University of Alberta

Library Release Form

Name of Author: Ryan R. Chladny

Title of Thesis: Modeling and Simulation of Automotive Gas Exchange Valve Solenoid Actuators

Degree: Master of Science

Year this Degree Granted: 2003

Ryan R. Chladny
#15 10731 85 Ave
Edmonton, Alberta,
Canada. T6E 2K9

"The highest plane of engineering science can only be achieved by the perfect blending of the utility of material things with the beauty of spiritual things"

–*Dr. J.J.C. Bradfield*

University of Alberta

Modeling and Simulation of Automotive Gas Exchange Valve Solenoid Actuators

by

Ryan R. Chladny

A thesis submitted to the Faculty of Graduate Studies and Research in partial fulfillment of the requirements for the degree of Master of Science.

Department of Mechanical Engineering

Edmonton, Alberta
Spring 2003

University of Alberta

Faculty of Graduate Studies and Research

The undersigned certify that they have read, and recommend to the Faculty of Graduate Studies and Research for acceptance, a thesis entitled Modeling and Simulation of Automotive Gas Exchange Valve Solenoid Actuators submitted by Ryan R. Chladny in partial fulfillment of the requirements for the degree of Master of Science .

Dr. C.R. (Bob) Koch

Dr. Alan Lynch

Dr. Roger Toogood

To my wife Melanie. Thank you for your love, understanding and the countless personal sacrifices that you have made in order for me to further my education.

ABSTRACT

A feasible method for significantly enhancing automotive engine efficiency is through direct actuation of intake and exhaust valves with electromechanical solenoids. Improvements of volumetric efficiency, fuel economy and emissions reduction while improving engine output have been demonstrated within laboratory settings, typically with electro-hydraulic or motor driven systems. Due to the highly non-linear physical relationships inherent to electromagnetic devices, design and control of such actuators has proven to be exceptionally challenging. To better predict actuator performance prior to prototype construction, a parametric Finite Element Analysis (FEA) model of a proposed actuator design was developed and validated with an existing physical prototype. The results from the FEA are incorporated within a lumped parameter model for control development and performance assessment. Consequently, a more accurate representation of alternate actuator designs can be investigated for control development, allowing for any subsequent design revisions to be made prior to costly prototype fabrication.

ACKNOWLEDGEMENTS

I would like to take this opportunity to acknowledge the following individuals / companies who helped me during the course of this work.

Dr. Koch for his selfless contribution of time, insight and invaluable wealth of knowledge.

Dr. Toogood for his encouragement and support during the unpredictable twists of my research.

Dr. Dale for his understanding, accommodation and genuine concern with regard to my funding.

DaimlerChrysler for the generous donation of solenoid actuators and test equipment.

No amount of thanks (or donuts) can repay technicians Ian Buttar, Bernie Faulkner and Andrew Coward or machinists Don Fuhr, Albert Yeun and Dave Pape for their expert skills, advice and the countless occasions where they sacrificed time from their projects for my own.

Thanks are also deserved to Terry Nord and Rasmus Torekov for their assistance with setting up and conducting the experimental tests and electrical schematic preparation.

Thanks to my colleagues of room 2-14 for their valued technical advice and laughs over lunch hours. Not to mention their continued daily efforts to promote safety awareness.

My parents for their continued love and encouragement throughout all of my challenges, academic or otherwise.

Table of Contents

LIST OF TABLES

List of Figures

Nomenclature

Note that bold typeface denotes a vector or matrix quantity.

i	Coil Current $[A]$
R	Coil Resistance $[\Omega]$
V	Coil Voltage $[V]$
σ	Conductivity $[S]$
$\boldsymbol{J}$	Current Density $[\frac{A}{m^2}]$
ρ	Electric Charge Density $[\frac{C}{m^3}]$
$\boldsymbol{E}$	Electric Field $[\frac{V}{m^2}]$
P	Electric Scalar Potential $[V]$
L	Inductance $[H]$
$\boldsymbol{B}$	Magnetic Field Flux Density $[T]$
$\boldsymbol{H}$	Magnetic Field Strength $[\frac{A}{m}]$
ϕ	Magnetic Flux $[Wb]$
λ	Magnetic Flux Linkage $[Wb$-turns$]$

MMF	Magnetomotive Force [A-turns]
$\boldsymbol{A}$	Magnetic Potential Vector $[\frac{Wb}{m^2}]$
μ_0	Permeability Constant $= 4\pi \times 10^{-7}\frac{H}{m}$
ϵ_0	Permittivity Constant $= 8.85\times10^{-12}\frac{F}{m}$
μ_r	Relative Permeability
$\Re$	Reluctance $[\frac{1}{H}]$
ν	Reluctivity $[\frac{m}{H}]$
τ	Time Constant

Chapter 1

Introduction

1.1 Introduction

A widely recognized method for significantly enhancing automotive spark ignition engine efficiency is through direct actuation of the intake and exhaust valves. Improvements of volumetric efficiency, fuel economy and emissions reduction while improving engine output have already been demonstrated within laboratory settings, usually with electro-hydraulic or motor driven systems. Independent control of the gas exchange valves also offers the possibility of facilitating promising fuel and combustion optimization strategies such as homogeneous charge compression ignition (HCCI), cylinder cut-out ability and flexible exhaust gas recirculation (EGR) schemes.

One promising means of actuation is through computer controlled electromechanical solenoids. Solenoids are ideal linear actuators for such applications as they are compact in size, relatively easy and cost effective to manufacture, simple to maintain and generally have fast response times.

However, implementing such actuators in an engine requires the satisfaction of a myriad of constraints which are often complex and conflicting in nature. In particular, the highly nonlinear physical relationships inherent with electromagnetic devices has made the design and control of such actuators exceptionally challenging. Traditional graphical and analytical techniques alone often prohibit accurate performance predictions due to nonlinear material properties, eddy currents, complex geometries and flux leakage. Commercially available Finite Element Analysis (FEA) software has recently aided with modeling, usually to calculate the nonlinear magnetic, mechanical and thermal properties of the actuator system. However, FEA use for the purpose of control design is less commonplace for automotive variable valve actuators. As a result, a costly design process of iteratively building a series of prototypes typically ensues.

It is the goal of this work to reduce the dependency of the iterative prototype design methodology typically found in practice today. Rather, a means of incorporating multidisciplinary analytical techniques with modern numerical simulation software is presented. Due to the inherently high speed and precision required of the actuator, attention must be given to the control design process. If control design is to be accomplished prior to prototype construction, accurately simulating and predicting actuator performance will be of significant concern. This work attempts to do so by utilizing ANSYS and Simulink together as a means of modeling the entire physical system of the actuator. This simulation process streamlines the design process by investigating key design parameters with ANSYS and then using the performance results in a Simulink simulation model. The result is a robust and realistic model of the actuator for performance prediction and control system development. Upon obtaining a satisfactory design, experimental controller programming can be reduced by using Simulink to generate controller code directly, minimizing programming time in the earlier design stages. In this way, the amount of empirical design and testing can be reduced, subsequently reducing the total design time and related expenses.

CHAPTER 2

A REVIEW OF CURRENT VARIABLE VALVE ACTUATOR TECHNOLOGY AND MODELING

2.1 Introduction

Currently, a myriad of variable valve timing (VVT) actuators have been implemented on laboratory engines. Electric motor, pneumatic, hydraulic and electromagnetic actuators have all been implemented and documented. Although such actuators have demonstrated the benefits of VVT on engine performance, their designs often neglect many of the issues which must be addressed prior to being implemented in a production vehicle. Means of preventing excessive valve seating velocity and the resulting wear and acoustic emissions are of particular concern. This chapter highlights some of the current efforts to implement VVT technology and actuator design strategies.

2.2 Benefits of a Flexible Valve-Train

An ever increasing demand for fuel efficiency and emission reductions, has motivated automotive manufacturers to find means of improving ICE performance. Without a feasible alternative to the internal combustion engine (ICE) foreseeable within the next ten to fifteen years [Atkins and Koch, 2003], methods of improving existing ICEs has become increasingly important. It was known as early as 1899 that having independent control over the timing of the gas exchange valves of an ICE could improve efficiency and performance [Allen and Law, 2002]. Standard ICEs with fixed camshaft timing usually must compromise low speed and high speed efficiency as the two modes of operation are conflicting [Schechter and Levin, 1996]. At high engine speeds, a delayed closing of the intake valve is desired to take advantage of air-fuel momentum, otherwise known as the ram effect. Conversely, at low engine speeds, ram-charging is negligible and intake valve closing should occur early to maximize the effective compression ratio and to avoid exhaust gas recirculation (EGR).

Until recently however, the computational and speed requirements for such actuation prohibited viable production VVT development. Investigating the effects of valve timing often required precision grinding of various camshafts to predetermined profiles [Theobald et al., 1994], making it extremely time consuming and expensive to obtain VVT data. With the advent of sophisticated hardware and software control electronics, engine valve timing ability is becoming ever more flexible. Instead of using a standard camshaft with one profile, it is not uncommon to implement mechanical devices capable of altering the valve phase [Pierik and Burkhard, 2000], duration [Hara et al., 2000] and lift [Nakamura et al., 2001], although usually within a limited crank angle range. BMW's Valvetronic, Porsche's Vario-Cam and Honda's VTEC are just a few examples of mechanical variable valve systems which are currently in production and offer some flexibility in valve actuation. However, such configurations do not offer the ability to change each individual valve event. In each of the aforementioned production systems, all intake valves will be changed to a new lift profile rather than just altering an individual valve. Such a requirement may occur when performing a cylinder deactivation procedure or for a staggered intake valve opening operation [Wilson et al., 1993]. As a result, the design and implementation of individual valve actuators which allow the ability to independently influence each valve irrespective of the crank angle or other valves in production vehicles is being actively pursued. Considerable work has already been done to demonstrate that the ability to independently alter valve timing to suit any given speed and load condition significantly improves engine performance. An extensive host of engine operation modes also becomes available with independent valve control, ranging from misfire emission control to regenerative engine braking [Schechter and Levin, 1996]. Laboratory engines have been fitted with hydraulic [Allen and Law, 2002, Barros da Cunha et al., 2000], pneumatic [Richeson and Erickson, 1989], motor [Henry, 2001] and electromagnetic actuators [Pischinger et al., 2000, Lequesne, 1990] to demonstrate the various benefits of VVT on engine performance. Torque output has been increased by 10%, fuel economy has been improved by 15% and NO_x emission output has been reduced by 20% [Moro et al., 2001, Pischinger et al., 2000, Lancefield et al., 1993].

2.3 Various Actuator Technologies

Presently, pneumatic and electro-hydraulic valve actuators for spark ignition engines are not expected to be mass produced in a production vehicle due to the relatively high unrecoverable energy input required to operate them [Henry, 2001]. In addition, these actuators tend to require considerable maintenance and their performance and accuracy are temperature sensitive. Pneumatic or hydraulic pumps, with coolers, filters and all the related accessories required to deliver the air or fluid are necessary to allow these actuators to operate in an on-board vehicle environment. Some hydraulic actuators rely on a traditional camshaft that provides pressure to small cylinders located above the valve body. Timing and lift may be then varied with a valve that controls the amount of fluid in the cylinder [Gecim, 1993, Kim et al., 1997, Barros da Cunha et al., 2000]. Aside from the increased parasitic load on the engine, such systems will increase associated engine manufacturing costs. Further costs may be associated with the safety equipment required to protect personnel from any system failures due to the presence of fluid pressures in excess of 34MPa (5000psi). As well, advanced control systems and electronics are required to coordinate appropriate valve motion. Pneumatic and hydraulic actuators are also susceptive to the same constraints as electromagnetic actuators such as cost, seating noise and speed requirements. It is suspected that it is for these reasons that successful use of such actuators has been primarily limited to either laboratory or to high output race engines.

Electric rotary motors which use permanent magnets have also been proposed for valve actuators. They typically employ mechanical devices which transform rotary motion into reciprocating linear motion. These systems appear relatively easy to control since valve position can be considered fixed with respect to the motor displacement. However, they are far less developed than pneumatic and hydraulic devices [Giglio et al., 2002], perhaps due to the relatively large physical volumes required to achieve the necessary response and valve speeds. Linear motors have also been implemented, but are better suited to valve strokes in excess of 20mm when compared with similar electromagnetic actuators. Although linear motors are faster for a single valve event, the high frequencies required and the resulting duty cycle demands make them unsuitable for ICE valve actuation applications [Lequesne, 1996]. Typically, electrically driven devices are easier to implement and require less energy input than that of an equivalent pneumatic or hydraulic device. Of course they still require a control system and a relatively large alternator to provide the additional electrical energy needed to drive them.

Another promising actuator configuration for independent valve control is the electromagnetic solenoid. Electromagnetic actuators for valve control were patented at least as early as the 1970s [Longstaff and Holmes, 1975, Pischinger and Kreuter, 1984]. Unlike the aforementioned hydraulic and pneumatic actuators, electromagnetic actuators are often designed with two springs which provide most of the necessary energy for a given valve cycle. After the armature is released it accelerates to the middle position, then the valve is decelerated with an opposing spring which stores the kinetic energy for the the next valve event. In the non-powered rest position, the two springs force the armature to the mid stroke position. In this way, electromagnetic energy is only required to influence the valve behavior at either end of the valve trajectory and to overcome any losses due to friction or gas forces. They are compact in size, relatively inexpensive to mass produce and are not as temperature dependant as their hydraulic counterparts. Like the motor based actuators, they require sophisticated electronic hardware and control software. A relatively large alternator / permanent magnet induction motor must also be employed to supply approximately 70W of peak electrical power per actuator at maximum engine speed and load. However, the extra electrical power requirement (3% of total engine output) is expected to be offset by the friction energy saved through the absence of camshafts (2% of total engine output for a roller-bearing valve-train) [Flierl and Klüting, 2000]. Successful implementation of electromagnetic actuators has also been generally limited to the laboratory, although several prototype vehicles have been built with an electromagnetic valve-train [Pischinger et al., 2000]. Control with combustion pressure disturbances has been particularly challenging. Feed-forward control has been implemented within laboratory settings, however such systems are unable to account for the significant combustion pressure fluctuations [Tai and Tsao, 2001]. In order to implement a reliable control system it must be robust to variations of the valve / actuator system. These variations include abrupt disturbances from combustion pressure variations as well as the relatively gradual parameter changes caused by fatigue, friction and temperature variations. In addition to these variations, the relatively high speed of the actuators, the non-linear magnetics and the short distance over which control is required has motivated many to develop closed loop control systems [Wang et al., 2002, Koch et al., 2002, Tai and Tsao, 2001, Hoffmann and Stefanopoulou, 2001]. Due to the design goals and the necessity for closed loop control, it has been determined that sophisticated armature position sensor resolution and frequency response are required. Such sensors are often expensive and difficult to calibrate in a mass production environment. However, efforts are being made to develop alternative cost effective sensors or sensing methods with sufficient response and resolution [Lynch et al., 2003, Rossi and Alberto, 2001, Takashi and Iwao, 1995, Roschke and Bielau, 1995].

2.4 Design Scopes

Due to the nonlinear and multidisciplinary nature of such electromagnetic devices, the design and control of these devices has been exceptionally challenging, particularly in maintaining acceptable valve seating and armature impact velocities.
There are at least three major areas in the design process of developing these actuators. They are as follows:

1. The actuator itself, which includes the geometric, electric, magnetic and mechanical aspects of the device.
2. The actuator system, which includes the actuator, valve, electronics and other associated dynamic effects such as friction and gas forces.
3. The control system, which includes algorithms for the various modes of operation and hardware specifications, such as sensor and controller requirements.

Each of these aspects require a significant level of expertise and resources. Therefore, it is common for published work to focus on only one aspect of the individual actuator design. Unfortunately, the wealth of published material is not uniformly distributed among the three areas. Most research discusses actuator control with little to no regard for the consequences of the actuator design on control performance. This is perhaps due to industry's desire to rapidly develop such devices. Thus, it is commonplace for designers to apply a top-down design approach of development, relying on an iterative process of constructing and testing prototypes without great certainty of controllability. Such a process is expensive and perhaps more time consuming than a bottom-up design approach. The focus of this thesis is on the modeling of the actuator and the actuator system in an effort to better predict actuator performance, and ultimately controllability, prior to prototype construction.

2.5 Actuator Design and Modeling

With many electromagnetic devices, simplified geometry and linear approximations are often satisfactory in estimating device performance. In the context of variable valve timing actuation design, control is to be applied in an operating region in which the air gap is small and at excitation levels sufficiently large that material saturation is significant, making linear theory unsatisfactory for accurately predicting actuator performance. The following highlights some of the work that has contributed to the advancement of actuator modeling. [Tai and Tsao, 2001] develop an LPM model which attempts to account for mechanical valve lash dynamics. The authors have approximated the force-position relation with the following function:

$$F_{Lin}(x,i) = \frac{\beta i^2}{(\kappa - x)^2} \tag{2.1}$$

Where coefficients β and κ are determined by performing a linear regression on experimentally obtained data. The function can then be used in a state space control model. This relation is quite common among literature as it works well in the unsaturated, or magnetically linear regions of the actuator where the permeability of the material can be assumed constant. Note that even with linear permeability, the force-position relationship is still inversely squared for constant excitations. For our actuator, it has been found that this relationship is generally a good approximation for lower excitation levels and air gaps in excess of one millimeter. Unfortunately, the actuator only develops significant force in air gaps of less than one millimeter, where model accuracy is most desirable. Common control performance indices of overshoot and trajectory tracking error are insufficient indicators of the quiet seating criterion. Engine speed and valve flight are also relevant parameters when quantifying "quiet seating". For this reason, Tai proposes an additional parameter, "seating tail-length", or seating settling time, which allows a method of comparing control strategies. Seating tail-length is defined by the additional time required to seat the valve when compared to the time required to achieve the minimum position achieved in a free oscillation. In this way, how quickly the valve can be seated can be expressed irrespective of the natural period of the armature, as determined by the actuator natural frequency. It is Tai's assertion that both the valve seating velocity together with the seating settling time should define the "quiet seating" ability of an actuator and control system. This can perhaps be more explicitly stated as how soft the valve lands and how quickly it can be seated.

The process of building a prototype first, then designing a control system, is perhaps best exemplified by the work of [Wang et al., 2002]. Wang et al. highlights some basic requirements for the actuator and claims that in order to develop a robust control strategy, a physical prototype must first be constructed. Upon prototype construction, force and flux data are collected experimentally. However, unlike Tai et al, this data is segmented into a linear and saturated region. A function is fitted to the respective regions using a linear regression approximation taking advantage of the same approximation Tai uses for the linear portion of data. The saturated expression takes the exponential form:

$$F_{Sat}(x,i) = [F_{Lin}(x,i_x) - F_{Max}(x)]e^{-k_i(x)(i-i_x)} + F_{Max}(x) \tag{2.2}$$

Where i_x is considered to be the saturation current, approximated by a linear function of position, $i_x = c_1 + c_2 i(x)$. The transition point between linear and saturated regions is determined by inspection of the experimental results as shown in [Wang et al., 2000]. $F_{Max}(x)$ is the maximum force developed at excitation levels above the saturation point, i_x, and $k_i(x)$ is a smoothing function that is solved for from the following stipulation:

$$\frac{\partial F_{Sat}(x,i)}{\partial i}|_{(x,i_x)} = \frac{\partial F_{Lin}(x,i)}{\partial i}|_{(x,i_x)} \tag{2.3}$$

This ensures a continuous force curve between the two regions. The final result is a series of linear state space equations which are represented in a mathematical (MATLAB-Simulink) model. A comparison of the model and experimental results is presented, generally showing good agreement. Although the segmentation of the linear and saturated regions likely enhances the force prediction for any given position and excitation, these approximations are of little use without the collection of data from an existing prototype. Their work also includes the results of dynamic test-bench studies. These experiments were performed to obtain values for dynamic parameters such as friction. Feedforward and feedback control strategies and results are discussed. A dSpace control card and pulse width modulated (PWM) current control is used but with 180 V for their experiments rather than a more practically attainable 42V (for in-vehicle applications).

Another proposed means of designing electromagnetic actuators is through the use of reluctance networks [Chillet and Voyant, 2001, Piron et al., 1999]. This analytic approach parallels an electric circuit approach to predicting actuator static and transient performance. By discretizing portions of the magnetic circuit into elements, each with their own permeability and geometric identity the same methods of solving electric circuits may be used to solve the reluctance network. The analytic approach to modeling can be quite cumbersome to use for complex geometries due to the need to predict the eddy current paths for model accuracy. This modeling technique also has difficulty in accounting for flux leakage as the extended flux air path may be ambiguous. It is acknowledged by [Piron et al., 1999] that a preliminary FEA analysis may need to be performed to predict flux and eddy current paths accurately. Both authors validate their approach by contrasting the results of their methods with those of equivalent FEA models. Chillet recognizes that such methods are not as accurate as FEA studies but are better suited to optimization studies due to the large number of iterations typically required in such studies. Indeed, this may be of particular use in the initial proof of concept and refinement stages of design. A FEA however should still be used as a means to generate any data intended for a control system dynamic model.

2.6 Use of FEA and LPM

In an attempt to better model actuator behaviour, more complex numerical methods have been employed such as reluctance networks and finite element analysis (FEA). These methods in themselves are satisfactory for optimizing steady state force and thermal output within specified material and geometric constraints. Unfortunately, most FEA software does not offer the ability to simultaneously predict electric, magnetic and mechanical responses for various initial conditions and constraints. Even using software where this is possible [ANS, 2002], the computational time required when using state of the art desktop computers is untenable. For these reasons, alternate methods of predicting transient system behaviour have been sought and developed.

The results from a steady state FEA will be incorporated into a lumped parameter model (LPM). This LPM is developed in the Matlab-Simulink environment and numerically integrates the differential equations describing armature and valve motion as well as coil dynamics. The LPM used at this time does not account for eddy currents. However, the parasitic effects of eddy currents for most modern actuators can often be considered negligible. This is due to the techniques available in mitigating the effects of eddy currents. These include the use of a laminar construction (larger surface areas yield longer eddy paths which in turn yield a higher net path resistance); powder metallurgy components (considered to again offer large surface areas due to the fine grain structure of the material); and the use of silicon steel (highly permeable yet resistive). Silicon steel offers substantially higher resistivity (1000 times greater) when compared with typical iron or steel, making it an ideal material in fast-acting electromagnetic devices.

The resulting LPM can then be used to develop a control system. Unlike the aforementioned work, the LPM can use data generated by the steady state results of the FEA model, without any dependance upon an existing prototype. Parameters such as spring stiffness and moving mass may be estimated based upon desired valve flight times and material properties.

The FEA model developed is also capable of predicting the actuator transient response for fixed armature positions. Such situations may be most useful for predicting the ability of an actuator to release the armature, the timing of which is critical in a real engine. Unlike the LPM model, the transient model is capable of predicting eddy current effects, although only at fixed positions. Consideration has been made to expedite the FEA computational time and minimize the model complexity while maintaining sufficiently accurate results to make experimental prototype fabrication unnecessary prior to control system development. The results have been verified by comparing the model predictions with the experimental results produced by an existing prototype. At the very least, this method can be used to predict which design candidate will offer the best overall performance. Although this method of actuator development is relatively uncommon, others have discussed or alluded to similar strategies.

[Giglio et al., 2002] have developed a method of modeling the actuator performance prior to prototype construction. The use of FEA software and a block diagram lookup table are claimed to have been developed. Unfortunately, little detail was provided regarding the model setup and structure. Nor is a comparison of simulated and actual results provided. They also propose a correction function, α, which is to be applied to the resulting expression for force. This function is derived by numerical experiments, and although not entirely clear, is presumably to account for deviations in their simulated force predictions and actual results. The relation appears as shown below.

$$F = \frac{B^2}{2\mu_o} S\alpha \tag{2.4}$$

and

$$B = \frac{\phi}{NS} \tag{2.5}$$

Where B is the magnetic flux density, ϕ is the flux linkage (presumably determined through FEA simulation), S is the armature area and μ_o is the free space permeability constant. If such a correction function is in fact used, then a prototype must have been tested and used to correct the FEA predictions. Few model details or results are discussed or quantified beyond what has been stated. The authors identify the need to minimize valve flight (usually achieved by high spring stiffness) while still maintaining reasonable holding currents and armature ‘first lift’ ability.

[Lequesne, 1999, Lequesne, 1990] discusses possible methods of improving solenoid performance by shaping the air gap to minimize reluctance and increase initial flux density on the armature. He promotes the use of a permanent magnet at either pole face to latch the armature at either extreme of the valve profile. This configuration is claimed to minimize energy consumption as no holding current is required at either extreme. Coils are then used to provide the coercive force necessary to temporarily counter the flux generated by the permanent magnet and subsequently release the armature. Although permanent magnets at each pole face will certainly decrease energy consumption, it will complicate landing speed control (if the design offers any control at all). In addition, most realistic (inexpensive) permanent magnet Curie Temperatures are within that of typical under-hood temperatures. Temperatures near the Curie Temperature are followed by a rapid demagnetization of permanent magnet materials, consequently rendering them useless in providing an armature holding force. In addition, these materials are often brittle, making them prone to premature wear and chipping over a device lifetime. His work does not offer any further regard to this matter other than a description of how the springs act as a brake. No specific landing speeds at corresponding engine operating speeds are offered. Lequesne acknowledges that there is a failure mode when the armature comes to rest in the middle of the two poles or spring mass equilibrium. However, his suggestion to overcome this situation by using permanent magnets sufficiently stronger than the spring force is perhaps incomplete for all modes of failure. Lequesne posits that lacking from existing literature is a systematic means to design electromagnetic gas exchange valve actuators. In his work he commonly uses FEA to validate any analytical models used. In [Lequesne, 1999] he mentions the use of integrating the static FEA results for instantaneous calculation of force and flux linkage.

[Melgoza and Rodger, 2002] investigate four methods of establishing LPMs to describe linear and rotary electromagnetic systems. The methods are evaluated for computational time and accuracy. It is acknowledged that it is not practical to fully simulate the overall performance of the actuator through a discretization processes. Rather, a more practical approach is the use of a simplified model that combines off-line results from an accurate field analysis with the speed of a LPM.

2.7 Summary

A brief overview of the progress towards designing and implementation of variable valve actuators is given with the goal of presenting the context of this work. Replacing the camshafts of traditional ICEs is a nontrivial task, and as such, design considerations and constraints are numerous. This thesis describes one method of predicting the actuator performance and provides a basis on which to develop a control system. This method is intended to expedite the design process by using FEA to generate data for use in a LPM. The LPM offers modeling flexibility and rapid solution time and thus minimizes the number of actuator prototypes that need to be manufactured.

CHAPTER 3

THEORY

3.1 Introduction

Due to the multidisciplinary nature of electromechanical actuators, a relatively large scope of physical phenomena must be examined when modeling such devices. The following presents a brief overview of the analytic and numeric tools and software applied during the course of actuator model development and analysis.

3.2 Vector Differential Calculus Operations & Notation

The following briefly summarizes the notation used to denote mathematical operations commonly used in the electromagnetic discipline, especially with Maxwell's equations.

3.2.1 Gradient of a Scalar Function

The gradient allows the derivation of vector fields from scalar functions, the latter of which are computationally easier to handle. For example, the gradient of a scalar function $s(x, y, z)$, results in

$$\nabla s = \frac{\partial s}{\partial x}\mathbf{i} + \frac{\partial s}{\partial y}\mathbf{j} + \frac{\partial s}{\partial z}\mathbf{k} \tag{3.1}$$

where x, y and z are Cartesian coordinates. The geometric interpretation of the gradient is such that ∇s points in the direction of maximum increase of s and the magnitude $\|\nabla s\|$ gives the slope or rate of increase along the maximum direction.

3.2.2 Divergence of a Vector Field and the Laplacian Operator

A useful operation in defining field quantities is the divergence operator, $\nabla\cdot$. Consider a differentiable vector function $\mathbf{v}(x, y, z)$, where x, y and z are Cartesian coordinates and the components of $\mathbf{v}$ are given by v_1, v_2 and v_3 as:

$$\mathbf{v}(x, y, z) = v_1\mathbf{i} + v_2\mathbf{j} + v_3\mathbf{k} \tag{3.2}$$

Then the divergence of $\mathbf{v}$ may be expressed as:

$$\nabla \cdot \mathbf{v} = \left(\frac{\partial}{\partial x}\mathbf{i} + \frac{\partial}{\partial y}\mathbf{j} + \frac{\partial}{\partial z}\mathbf{k}\right) \cdot (v_1\mathbf{i} + v_2\mathbf{j} + v_3\mathbf{k}) = \frac{\partial v_1}{\partial x} + \frac{\partial v_2}{\partial y} + \frac{\partial v_3}{\partial z} \tag{3.3}$$

Note that $\nabla \cdot \mathbf{v}$ depends only on $\mathbf{v}$ and the points in space, not on the choice of coordinate system.

If a scalar function $s(x, y, z)$ is able to be differentiated twice, the divergence of a gradient may be expressed as:

$$\nabla \cdot \nabla s = \frac{\partial^2 s}{\partial x^2} + \frac{\partial^2 s}{\partial y^2} + \frac{\partial^2 s}{\partial z^2} \tag{3.4}$$

This operation is also known as the Laplacian of $s(x, y, z)$ where the Laplacian operator is denoted by ∇^2 and may be written as:

$$\nabla^2 = \Delta = \nabla \cdot \nabla = \frac{\partial^2}{\partial x^2} + \frac{\partial^2}{\partial y^2} + \frac{\partial^2}{\partial z^2} \tag{3.5}$$

The geometric interpretation of divergence is the measure of how much a vector spreads or diverges from a given point. A point of positive divergence can be thought of as a 'source'. Similarly, a negative point of divergence can be considered a 'sink'.

3.2.3 Curl of a Vector Field

Again consider a differentiable vector function $\mathbf{v}(x, y, z)$ as before. The curl of $\mathbf{v}$ in a right handed Cartesian coordinate system is then defined as:

$$\nabla \times \mathbf{v} = \left(\frac{\partial v_3}{\partial y} - \frac{\partial v_2}{\partial z} \right) \mathbf{i} + \left(\frac{\partial v_1}{\partial z} - \frac{\partial v_3}{\partial x} \right) \mathbf{j} + \left(\frac{\partial v_2}{\partial x} - \frac{\partial v_1}{\partial y} \right) \mathbf{k} \tag{3.6}$$

Although curl is defined in terms of coordinates, it is not dependant on the coordinate system. The result of the curl operation can be considered a measure of how much the vector $\mathbf{v}$ rotates about a specified point. The curl of a gradient is always zero. For any scalar function $s(x, y, z)$ that is twice differentiable

$$\nabla \times (\nabla s) = 0 \tag{3.7}$$

Thus it may be observed that gradient fields are irrotational. Similarly, the divergence of a curl is also always zero, $\nabla \cdot (\nabla \times \mathbf{v}) = 0$.

3.3 Maxwell's Equations

James Clerk Maxwell recognized four general unifying relations which now make up the foundation of all classical electromagnetic field theory. These equations provide a means of coupling time varying electric and magnetic fields [Griffiths, 1999]. They are briefly derived in Appendix A and summarized below.

$$\nabla \cdot \boldsymbol{E}(\mathbf{r}, t) = \frac{\rho}{\epsilon_0}, \tag{3.8}$$

$$\nabla \times \boldsymbol{B}(\mathbf{r}, t) = \mu_0 \boldsymbol{J}(\mathbf{r}, t) + \mu\epsilon_0 \frac{\partial \boldsymbol{E}(\mathbf{r}, t)}{\partial t}, \tag{3.9}$$

$$\nabla \times \boldsymbol{E}(\mathbf{r}, t) = -\frac{\partial \boldsymbol{B}(\mathbf{r}, t)}{\partial t}, \tag{3.10}$$

$$\nabla \cdot \boldsymbol{B}(\mathbf{r}, t) = 0 \tag{3.11}$$

Where $\mathbf{r}$ is a position vector and t represents a time scalar.

Generally speaking, a vector field may be defined by specifying both the curl and the divergence of the field. In Equation 3.9, Maxwell extended the original expression by adding the far right hand side term, known as displacement current, to account for influence of time varying electric fields displacing electrons and thus generating current. Equation 3.10 is a derivation of Faraday's law (with Stokes theorem) which states that a time-varying magnetic field produces a corresponding electric field. The relationship is such that the electric field lines produced tend to encircle the magnetic field lines. Equation 3.11 indicates that no net flux may emanate from any given region of space and is perhaps most commonly visualized by considering a closed surface enclosing one end of a permanent bar magnet. In such an instance, there is an inward (negative) flux flowing through the interior of the magnet itself and there is an outward flow out the end of the magnet, through space and finally returning to the opposite pole. Thus, the net magnetic flux, ϕ_B, through an arbitrary closed surface is always zero.

3.3.1 Simplifying Assumptions

These relations are general enough to account for electromagnetic waves ranging from radio to gamma radiation. However, in the study of electromechanical devices, wave phenomenon are often disregarded as the electrical excitation frequencies are usually low enough that the system may be regarded as quasi-static, or slowly varying with time. This means that although the time dependency of the magnetic induction term $-\frac{\partial \boldsymbol{B}}{\partial t}$ of Equation 3.10 is of interest during transient analyses, the magnetic field may be approximated by ignoring the displacement current term in Equation 3.9, as nearly all the energy will be stored in the magnetic field rather than an electric field. For example, electromagnetic devices are often not limited by the propagation speed of electromagnetic fields traveling at the speed of light because their dimensions are relatively small. As such, the general solution of a given problem without the quasi-static assumption will likely have some portion depending on a ratio between the system geometry and the speed of light, and may be approximated as zero. The result is an approximation that a slowly varying electric excitation produces only a slowly varying magnetic field. Generally speaking, either the electric or magnetic field will dominate over the other, depending on the problem configuration. This fact is used to simplify the above complex relations to more practical expressions. For example, when a short circuit exists as in the case of a coil of wire, a large current typically exists and a large static magnetic field results. Accordingly, the displacement current is of negligible importance. In contrast, two isolated plates when excited with a constant electric potential result in an electric field but not a magnetic one, as the magnetic induction term is negligible. The quasi-static approximation allows the assumption that only one field is dominant and thus it is possible to de-couple the electric and magnetic relations and only consider the dominant field.

The revised Maxwell's equations with the quasi-static limit imposed for the case of a dominant magnetic field are shown below.

$$\nabla \cdot \boldsymbol{E}(\mathbf{r}, t) = \frac{\rho}{\epsilon_0}, \tag{3.12}$$

$$\nabla \times \boldsymbol{B} = \mu_0 \boldsymbol{J} \tag{3.13}$$

$$\nabla \times \boldsymbol{E} = -\frac{\partial \boldsymbol{B}}{\partial t} \tag{3.14}$$

$$\nabla \cdot \boldsymbol{B} = 0 \tag{3.15}$$

Note that the displacement current in Equation 3.9 is no longer present in Equation 3.13, yet the magnetic field still has a time dependency through Equation 3.14.

3.4 ANSYS and Magnetic Vector Potential

For the magnetic field solution of the actuator, 2D models are constructed with the commercially available FEA software, ANSYS, by ANSYS Inc. ANSYS utilizes the vector potential method for both static and transient cases with a quasi-static limit which dismisses any displacement currents, thereby using the above subset of Maxwell's equations. Equations 3.16 and 3.17 are also used to describe material behavior for the cases of: temperature independence, no permanent magnets and zero relative motion (although ANSYS is capable of including those cases).

$$\boldsymbol{H} = \boldsymbol{\nu} \boldsymbol{B} \tag{3.16}$$

where $\boldsymbol{\nu}$ is generally a reluctivity matrix, $[\nu] = [\mu]^{-1}$, however for the case of temperature independence and orthotropic material permeability, $\boldsymbol{\nu} = \nu = \frac{1}{\mu}$. μ is the relative permeability defined by a table of field, H and flux density, B values. The electric field is related to applied current density through

$$\boldsymbol{J} = \sigma \boldsymbol{E} \tag{3.17}$$

Generally ANSYS uses a matrix to represent material conductivity as σ. Again, material conductivity is assumed to be orthotropic, therefore σ may be assumed a scalar quantity. Note that precautions may need to be taken when modeling laminated devices as this assumption may no longer be valid.

With the modified Maxwell's and constitutive equations established, a solution is then sought to satisfy equations 3.13 through 3.15 over the entire model domain. For the actuator models analyzed, ANSYS introduces potentials to represent the magnetic and electric fields. The electric field $\boldsymbol{E}$ is a vector field which is always irrotational or has a zero curl component (proved with Coulomb's Law). This property may be used to transform the problem of solving for the vector $\boldsymbol{E}$ into a problem of solving for a scalar quantity known as the electric scalar potential, P. Recall from Section 3.2.3 that an irrotational vector may be represented as the gradient of a scalar function. Thus the electric field may be expressed as:

$$\boldsymbol{E} = -\nabla P \tag{3.18}$$

Substituting this expression into Equation 3.10 results in:

$$\nabla \cdot \boldsymbol{E} = \nabla \cdot (-\nabla P) = -\nabla^2 P = \frac{\rho}{\epsilon_0} \tag{3.19}$$

Which is known as Poisson's equation, or in non-conducting regions ($\rho = 0$), Laplace's equation. Thus the electric potential can be solved for with one differential equation and then related to $\boldsymbol{E}$ rather than solving for both the divergence and curl of $\boldsymbol{E}$.

In a similar fashion, the magnetic field $\boldsymbol{B}$ may be expressed as a magnetic vector potential $\boldsymbol{A}$ by proving that a magnetic field is divergence free as shown in Equation 3.15 (may be proven with the Biot-Savart law). For a field that has no divergence then it may be stated that

$$\boldsymbol{B} = \nabla \times \boldsymbol{A} \iff \nabla \cdot \boldsymbol{B} = 0 \tag{3.20}$$

However, the vector potential does not offer uniqueness. Any function with zero curl, or a gradient of a scalar function may be added to the potential $\boldsymbol{A}$ since the curl of a gradient is always zero. Thus, the divergence of $\boldsymbol{A}$, may be chosen to be zero as

$$\nabla \cdot \boldsymbol{A} = 0 \tag{3.21}$$

This stipulation is known as the Coulomb gauge condition. Substituting equation 3.20 into Faraday's law, equation 3.14, yields:

$$\nabla \times \boldsymbol{E} = -\frac{\partial}{\partial t}(\nabla \times \boldsymbol{A}) \tag{3.22}$$

or rearranging,

$$\nabla \times \left(\boldsymbol{E} + \frac{\partial \boldsymbol{A}}{\partial t}\right) = 0 \tag{3.23}$$

When written as the gradient of a scalar potential,P

$$\boldsymbol{E} = -\nabla P - \frac{\partial \boldsymbol{A}}{\partial t} \tag{3.24}$$

Equations 3.20 and 3.24 satisfy Maxwell's equations 3.14 and 3.15. Again, Substituting equations 3.20 into Ampére's equation, 3.13, results in:

$$\nabla \times (\nabla \times \boldsymbol{A}) = \mu_0 \boldsymbol{J} \tag{3.25}$$

Making use of the identity

$$\nabla \times (\nabla \times \boldsymbol{A}) = \nabla(\nabla \cdot \boldsymbol{A}) - \nabla^2 \boldsymbol{A} \tag{3.26}$$

and the Coulomb Gauge condition, $\nabla \cdot \boldsymbol{A} = 0$, results in:

$$\boxed{-\nabla^2 \boldsymbol{A} = \mu_0 \boldsymbol{J}} \tag{3.27}$$

This equation makes up one of three that ANSYS solves. The other two equations are derived from the divergence free property of current density $\nabla \cdot \boldsymbol{J} = 0$, and the constitutive relation, Equation 3.16. Substituting Equation 3.17 into the expression for divergence free current density results in:

$$\sigma \nabla \cdot \boldsymbol{E} = 0 \tag{3.28}$$

Substituting in Equation 3.24,the electric scalar potential yields:

$$\boxed{\nabla \cdot \left(-\nabla P - \frac{\partial \boldsymbol{A}}{\partial t} \right) = 0} \tag{3.29}$$

Which is another equation that ANSYS solves. Finally, the relations $\nabla \times \boldsymbol{H} = \boldsymbol{J}$ and Equations 3.16 and 3.17 are combined to yield:

$$\nu \nabla \times \boldsymbol{B} = \sigma \boldsymbol{E} \tag{3.30}$$

Substituting in the magnetic and electric potentials results in:

$$\nu \nabla \times (\nabla \times \boldsymbol{A}) = \sigma \left(-\nabla P - \frac{\partial \boldsymbol{A}}{\partial t} \right) \tag{3.31}$$

This may be simplified using the identity in Equation 3.26 and the Coulomb gauge condition to

$$\boxed{-\nu \nabla^2 \boldsymbol{A} + \sigma \frac{\partial \boldsymbol{A}}{\partial t} + \sigma \nabla P = 0} \tag{3.32}$$

It should be noted that the three derived equations will vary slightly in different material regions. For conducting (steel and copper coil) regions, this results in the following equations:

$$-\nu(\boldsymbol{H}) \nabla^2 \boldsymbol{A} = \boldsymbol{J} \tag{3.33}$$

$$\nabla \cdot \left(\frac{\partial \boldsymbol{A}}{\partial t} - \nabla P \right) = 0 \tag{3.34}$$

$$\sigma \frac{\partial \boldsymbol{A}}{\partial t} - \frac{1}{\mu(\boldsymbol{H})} \nabla^2 \boldsymbol{A} + \sigma \nabla P = 0 \tag{3.35}$$

For nonconducting, or air regions, the following equations apply:

$$-\nu_0 \nabla^2 \boldsymbol{A} = \boldsymbol{J} \tag{3.36}$$

$$\nabla \cdot \left(\frac{\partial \boldsymbol{A}}{\partial t} - \nabla P \right) = 0 \tag{3.37}$$

$$\nabla^2 \boldsymbol{A} = 0 \tag{3.38}$$

These differential equations are assembled into respective matrices and numerically solved as shown in the following sections.

3.4.1 Static Elements

For the static models, two element types were used. The two dimensional element type PLANE13 is used throughout the iron and air regions. Although this element may be used in non-magnetic studies, the nodal degree of freedom (DOF) that is solved for in the static analyses is the magnetic vector potential in the z or normal direction. The quadrilateral element is defined by four nodes at each corner of the element. Nonlinear magnetic materials are permitted by associating an appropriate property table with the element type. The axis-symmetric option was specified which requires all loads to be specified to accommodate the full actuator rather than per unit length or thickness. Similarly, all output results are representative of a 360^o model when the axis-symmetric option is specified. Magnetic forces are determined using both a Maxwell stress tensor calculation and Virtual Work calculation on surfaces in contact with air regions by using a macro that recognizes surfaces that have been identified or 'flagged' for such force calculations. The elements making up the armature region of the model are identified for such a force calculation. A steady-state current density body load is applied to the elements which make up the coil region. Note that this element does not possess voltage forced capability. Flux density is output with respect to the two dimensions of the element co-ordinate system. Flux is calculated by first defining a two point path. A macro then defines a pre-specified number of points along the path which flux density is integrated over. For all elements used, a default coordinate system orientation was used. These default systems are right-handed, orthogonal and parallel to the global Cartesian coordinate system.

To model far-field decay without solving for a large amount of additional elements, a single layer of INFI110 infinite boundary elements were used to surround the air region of the actuator model. These elements use four nodes and shape functions which force the magnetic potential to zero at infinity. These elements have both four node and eight node capability, but only offer the magnetic potential DOF. When used with PLANE13 elements, ANSYS documentation recommends using the four node option.

3.4.2 Transient Elements

The transient model elements used are similar to those of the static analyses with a few minor exceptions. In order to more closely represent the way in which the actuator is excited, a model with a circuit coupled voltage source was used. As such, PLANE53 elements were used throughout the air, iron and coil regions instead of PLANE13. This element is defined by eight nodes, each possessing up to four possible DOFs. These include the magnetic vector potential, a time-integrated electric scalar potential, electric current, and electromotive force (EMF). It is these additional degrees of freedom that make PLANE53 applicable to low frequency transient electromagnetic-circuit coupled analyses. However, only the magnetic potential degree of freedom was considered through the air and iron regions. In the coil region, the electric current and EMF degrees of freedom were also activated to allow for nodal coupling to the circuit domain. The circuit consists of three CIRCU124 elements, each of a different configuration. CIRCU124 elements are based on Kirchhoff's Current Law with stiffness matrices based on a lumped circuit model. An independent voltage source, stranded coil and resistor elements were meshed in series to represent the actuator circuit. The resistor was typically set to a value close to zero as it was only added to enhance model flexibility. The resistor only possesses a voltage degree of freedom. An independent voltage source was used to represent the actuator power source. The voltage source element has voltage and current degrees of freedom. The voltage degrees of freedom are specified by terminating one node as a ground, or 0V, and another node as a piecewise linear voltage function of time. This allows for the ability to 'switch' the supply on or off in a similar fashion to the real experimental power electronics. Finally, the stranded coil element has voltage, current and EMF degrees of freedom. The voltage degrees of freedom are coupled to the resistor and ground nodes. The EMF and current DOFs are coupled to a node in the coil region in the FEA domain. Similarly, all nodes in the coil region have the current and EMF DOFs coupled to one another. Physical coil properties are implied by the elements from the coil region FEA domain and specified material constants. Again, INFIN110 elements were used to surround the air region, however, with the 8 node option activated, as recommended by ANSYS documentation for use with PLANE53 elements.

3.4.3 Element Shape Functions

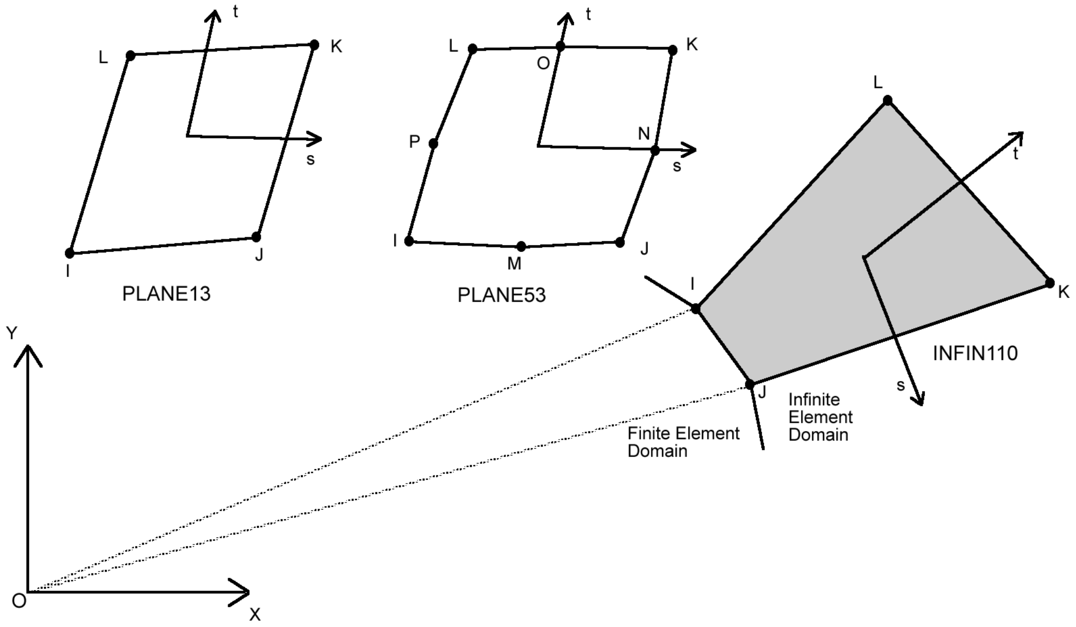

Figure 3.1: Element Configurations

Figure 3.1 illustrates the PLANE13, PLANE53 and INFIN110 elements. Coordinates s and t represent the local element nodal coordinate system. When the coordinates are used with the shape functions, they are normalized, going from -1.0 on one side of the element to +1.0 on the other. It should also be noted that s and t are not necessarily orthogonal to one another. The shape functions for the 2D magnetic vector potential (z component only) for each of the elements are as follows for PLANE13, PLANE53 and INFIN110 respectively:

$$\begin{aligned}\boldsymbol{A}_{\boldsymbol{z}PLANE13} &= \tfrac{1}{4}(\boldsymbol{A}_{\boldsymbol{z}I}(1-s)(1-t)+\boldsymbol{A}_{\boldsymbol{z}J}(1+s)(1-t)\\ &\quad +\boldsymbol{A}_{\boldsymbol{z}K}(1+s)(1+t)+\boldsymbol{A}_{\boldsymbol{z}L}(1-s)(1+t))\end{aligned} \tag{3.39}$$

$$\begin{aligned}\boldsymbol{A}_{\boldsymbol{z}PLANE53} &= \tfrac{1}{4}(\boldsymbol{A}_{\boldsymbol{z}I}(1-s)(1-t)+\boldsymbol{A}_{\boldsymbol{z}J}(1+s)(1-t)\\ &\quad +\boldsymbol{A}_{\boldsymbol{z}K}(1+s)(1+t)+\boldsymbol{A}_{\boldsymbol{z}L}(1-s)(1+t))\\ &\quad +\tfrac{1}{2}(\boldsymbol{A}_{\boldsymbol{z}M}(1-s^2)(1-t)+\boldsymbol{A}_{\boldsymbol{z}N}(1+s)(1-t^2)\\ &\quad +\boldsymbol{A}_{\boldsymbol{z}O}(1-s^2)(1+t)+\boldsymbol{A}_{\boldsymbol{z}P}(1-s)(1-t^2))\end{aligned} \tag{3.40}$$

$$\begin{aligned}\boldsymbol{A}_{\boldsymbol{z}INFIN110} &= \tfrac{1}{4}(\boldsymbol{A}_{\boldsymbol{z}I}(1-s)(t^2-t)+\boldsymbol{A}_{\boldsymbol{z}J}(1+s)(t^2-t))\\ &\quad +\tfrac{1}{2}(\boldsymbol{A}_{\boldsymbol{z}K}(1+s)(1-t^2)+\boldsymbol{A}_{\boldsymbol{z}L}(1-s)(1-t^2))\end{aligned} \tag{3.41}$$

The shape functions for voltage are analogous, and can be formed by substituting the scalar voltage with the magnetic vector potential terms. ANSYS assembles these functions for each element in shape function matrices. Hence the magnetic potential $\boldsymbol{A}$ and the scalar electric potential P may be represented by matrices $\boldsymbol{N}_{\boldsymbol{A}}$ and $\boldsymbol{N}_P$ respectively:

$$\boldsymbol{A} = \boldsymbol{N_A}^T\boldsymbol{A_e} = \boldsymbol{N_A}^T\begin{bmatrix}0\\0\\\boldsymbol{A_{ze}}\end{bmatrix} \tag{3.42}$$

and

$$\boldsymbol{P} = \boldsymbol{N}_P^T\boldsymbol{P_e} \tag{3.43}$$

ANSYS then uses $\boldsymbol{N_A}$ to calculate the flux density as follows:

$$\boldsymbol{B} = \nabla \times \boldsymbol{N_A A_e} \tag{3.44}$$

Where $\boldsymbol{A_e}$ and $\boldsymbol{P_e}$ are the nodal magnetic and electric potentials which are solved as described in the following sections.

3.4.4 Matrix Assembly

After the 2D model is meshed and appropriate boundary conditions and loads are applied, ANSYS solves equations of the following form:

$$[C]\dot{\boldsymbol{d}} + [K]\boldsymbol{d} = \boldsymbol{J} \tag{3.45}$$

Where the degree of freedom vector is represented by

$$\boldsymbol{d} = \begin{bmatrix} \boldsymbol{A_z} \\ \boldsymbol{P} \end{bmatrix} \tag{3.46}$$

$\boldsymbol{A_z}$ represents the magnetic vector potential in the Z direction (into the model/page) as this is the only relevant potential direction for the 2D axis-symmetric case. Note that this is a relatively large vector as it represents all elements. $\boldsymbol{P}$ is the time integrated electric scalar potential, $\boldsymbol{P} = \int P dt$ which is input as a voltage excitation (if one exists).

Matrices $[C]$ and $[K]$ are the coefficient matrices defined as:

$$[K] = \begin{bmatrix} [K^L] + [K^N] + [K^G] & 0 \\ 0 & 0 \end{bmatrix} \tag{3.47}$$

and,

$$\begin{aligned}
\left[K^L\right] = &\ \int_{Vol}(\nabla \times \boldsymbol{N_A}^T)^T \nu (\nabla \times \boldsymbol{N_A}^T) dV, \\
\left[K^N\right] = &\ \int_{Vol}(\nabla \times \boldsymbol{N_A}^T)^T \nu (\nabla \cdot \boldsymbol{N_A}^T) dV, \\
\left[K^G\right] = &\ 2\int_{Vol} \frac{d\nu}{d|B|^2} (\boldsymbol{B}^T(\nabla \times \boldsymbol{N_A}^T))^T (\boldsymbol{B}^T(\nabla \times \boldsymbol{N_A}^T)) dV
\end{aligned}$$

Where the element shape function matrices are integrated over their respected volumes. In the axis-symmetric case, the element positions are mapped to the global coordinate system so that the appropriate volume can be derived for the entire actuator. As before, ν represents the reluctivity matrix, $[\mu]^{-1}$, but for the case of orthotropism, is considered a magnetic field intensity dependant scalar. The nonlinear input B-H cure is converted to a spline fit function of ν vs $|\boldsymbol{B}|^2$ from which the derivative $\frac{d\nu}{d|B|^2}$ may be taken. The transient coefficient matrices are as follows:

$$[C] = \begin{bmatrix} \left[C^{AA}\right] & \left[C^{Av}\right] \\ \left[C^{Av}\right] & \left[C^{vv}\right] \end{bmatrix} \tag{3.48}$$

where,

$$\begin{aligned}
\left[C^{AA}\right] = &\ \int_{Vol} \boldsymbol{N_A} \sigma \boldsymbol{N_A}^T dV, \\
\left[C^{Av}\right] = &\ \int_{Vol} \boldsymbol{N_A} \sigma \nabla \cdot \boldsymbol{N}_P^T dV, \\
\left[C^{vv}\right] = &\ \int_{Vol} (\nabla \cdot \boldsymbol{N}_P^T)^T \sigma \nabla \cdot \boldsymbol{N}_P^T dV
\end{aligned}$$

For static analyses (no time dependant potentials or fields), only the K matrices and magnetic vector potential DOFs are required as Equations 3.33 through 3.38 will be further simplified when $\boldsymbol{B}$ is time invariant.

The load vector is defined as:

$$\boldsymbol{J} = \begin{bmatrix} \int_{Vol} \boldsymbol{J_s} \boldsymbol{N_A}^T dV \\ \int_{Vol} \boldsymbol{J_t} \boldsymbol{N_A}^T dV \end{bmatrix} \tag{3.49}$$

Where $\boldsymbol{J_s}$ is the source current density vector (also referred to as current segments) and $\boldsymbol{J_t}$ is the total current density vector. The total current density vector is equal to the summation of the source currents, eddy currents and induced velocity currents (not present as armature is fixed in all simulations).

3.4.5 Static Model Solution

As shown in the previous section, the FEA discretization process results in a series of simultaneous nonlinear equations as represented by Equation 3.45. For static models, the time dependant magnetic potential vector and coefficient matrices can be disregarded and an incremental Newton-Raphson method is used to solve nonlinear systems by:

$$[K^T_{n,i}]\Delta\boldsymbol{A_{z,i}} = \boldsymbol{J_n} - \boldsymbol{J^{nr}_{n,i}} \tag{3.50}$$

Where $[K^T_{n,i}]$ is the Dirichlet matrix for sub-step n, and iteration i. $\boldsymbol{A_{z,i}}$ is the magnetic potential vector at iteration i and $\Delta\boldsymbol{A_{z,i}} = \boldsymbol{A_{z,i+1}} - \boldsymbol{A_{z,i}}$. $\boldsymbol{J_n}$ is the applied current density vector for a given sub-step n, and $\boldsymbol{J^{nr}_{n,i}}$ is referred to as the resisting load vector which is calculated from element magnetic fluxes. The right-hand side of Equation 3.50 is referred to as the residual or out-of-balance load vector and represents the amount the system is out of equilibrium. A predetermined number of sub-steps are required for solution convergence when the system is highly nonlinear or path-dependent. These intermediate steps are performed so that the final current density vector $\boldsymbol{J}$ is achieved by applying it in increments. At each sub-step the Newton-Raphson procedure is performed by assuming a potential vector $\boldsymbol{A_{z,o}}$, which is usually obtained from the last converged iteration, $\boldsymbol{A_{z,i}}$. An updated coefficient matrix, $[K^T_{n,i}]$ and load vector, $\boldsymbol{J^{nr}_{n,i}}$ are determined from the magnetic potential vector, $\boldsymbol{A_{z,i}}$. Next $\Delta\boldsymbol{A_{z,i}}$ is solved for from Equation 3.50. Then $\boldsymbol{A_{z,i+1}}$ is computed by adding $\Delta\boldsymbol{A_{z,i}}$ to $\boldsymbol{A_{z,i}}$ or $\boldsymbol{A_{z,o}}$ if it is the first iteration. These equilibrium iterations are repeated until convergence is achieved for each sub-step and the current density vector is fully applied. Convergence checking can be based on either magnetic potentials, current segments, or both. However, for 2D axis-symmetric models, ANSYS recommends convergence to be determined by current segments as:

$$\sqrt{\sum(\boldsymbol{J}-\boldsymbol{J}_{\boldsymbol{i}}^{\boldsymbol{nr}})^2} < \zeta_J J_{Ref} \tag{3.51}$$

Where ζ_J is a specified tolerance of a typical current segment value, J_{Ref}, which is taken as $\|\boldsymbol{J}\|$. For magnetic potential convergence, ANSYS compares the change in nodal potential values between successive equilibrium iterations to a similar criterion as above.

3.4.6 Transient Model Solution

For the transient models, a generalized trapezoidal rule

$$\boldsymbol{A_{z,n+1}} = \boldsymbol{A_{z,n}} + \Delta t \dot{\boldsymbol{A}}_{\boldsymbol{z,n+1}} \tag{3.52}$$

is used to numerically integrate Equation 3.45 over a series of time steps, $\Delta t = t_{n+1} - t_n$ prior to the application of the incremental Newton-Raphson method as discussed in the static analyses. The magnetic potentials at time t_n are represented by $\boldsymbol{A_{z,n}}$ and the respective time derivative $\dot{\boldsymbol{A}}_{\boldsymbol{z,n}}$ is calculated at the previous time step. Substituting the trapezoidal approximation at time t_{n+1} into Equation 3.45 results in:

$$\left(\frac{1}{\Delta t}[C] + [K]\right)\boldsymbol{A_{z,n+1}} = \boldsymbol{J} + \frac{1}{\Delta t}[C]\boldsymbol{A_{z,n}} \tag{3.53}$$

This equation set is then solved in a similar fashion to the static models. However, sub-steps are now replaced with a time step, (ie. the load is no longer ramped). Therefore, to ensure convergence, a sufficiently small time step size must be used.

Upon calculation of $\boldsymbol{A_{z,n+1}}$, equation 3.52 is used to update $\dot{\boldsymbol{A}}_{\boldsymbol{z,n+1}}$.

3.5 Linear Theory & System Energy

Complex nonlinear systems can often be approximated as linear systems by making simplifying assumptions. This often allows for a starting point or perhaps an ability to observe general trends in particular regions of interest where the nonlinear effects do not dominate. Such is often the case in basic electromagnetic circuit analysis. For example, in many instances it may be assumed that the permeability of any particular material is linear (saturation does not occur). With this assumption, magnetic calculations can be expedited, and at low field intensities, good accuracy may be achieved, particularly at larger air gaps. In this way, one may be able to glean insights between one core geometry type from another, for example. Afterward, perhaps a rigorous investigation of the most promising design with a Finite Element simulation could be performed. Consider Figure 3.2 which illustrates the actuator schematically. When the armature of the actuator moves, energy is exchanged among three forms. Namely, the mechanical system, the electrical system and the magnetic field. It is possible to consider an energy balance of the entire system when observing the nature of the force development so that a complex field analysis may be avoided [Schmitz and Novotny, 1965].

The general energy balance equation for the three disciplines may be expressed as:

$$\Delta W_e = \Delta W_f + \Delta W_m \tag{3.54}$$

where ΔW_e, ΔW_f, ΔW_m represent changes in electrical, magnetic and mechanical energies respectively.

Since mechanical force may be expressed as a change of energy over a distance, the

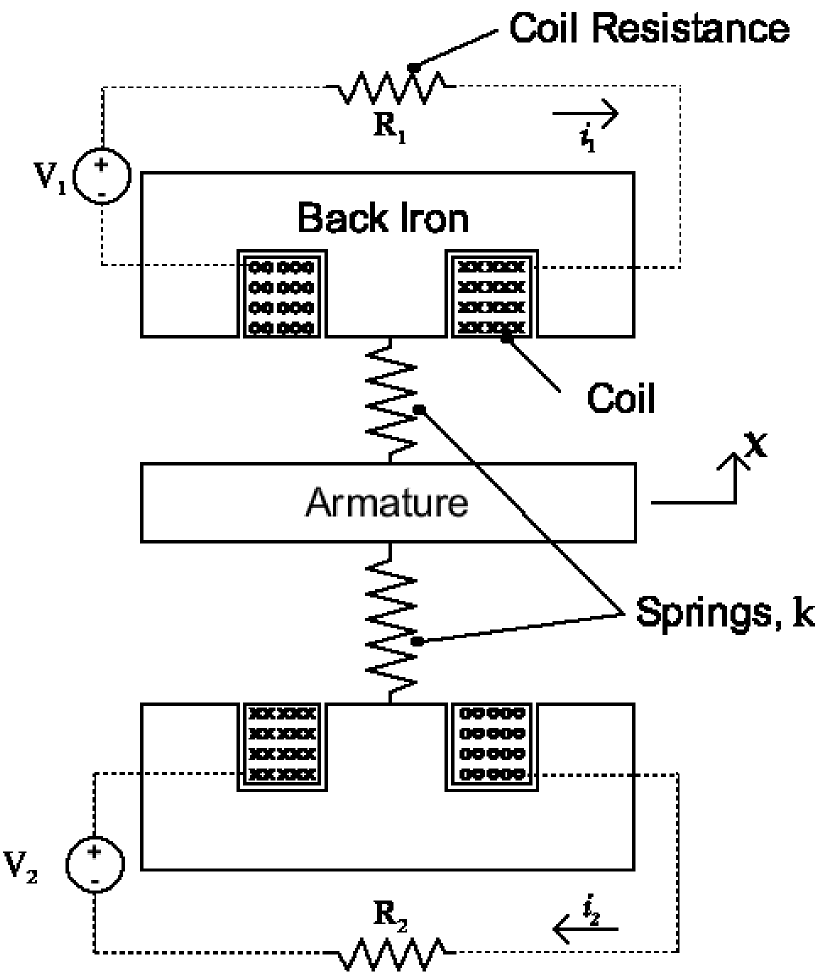

Figure 3.2: Actuator Schematic

average force on the armature may be stated as:

$$F_{avg}\Delta x = \Delta W_m \tag{3.55}$$

Implicitly, it may be observed from Equation 3.54 that for any given position, the mechanical energy may be determined from either magnetic flux linkage, λ, or electrical current, i. Thus, the average force may be expressed as:

$$F_{avg} = \frac{\Delta W_e(i,x)}{\Delta x} - \frac{\Delta W_f(i,x)}{\Delta x} \tag{3.56}$$

or

$$F_{avg} = \frac{\Delta W_e(\lambda, x)}{\Delta x} - \frac{\Delta W_f(\lambda, x)}{\Delta x} \tag{3.57}$$

For a simple air-coil-resistor circuit, W_f can be expressed as the stored energy in the coil over a change in time, $\Delta t = t_2 - t_1$, as:

$$W_c = \int_{t_1}^{t_2} i V_{Coil} dt \tag{3.58}$$

Using Faraday's law of induction, $V_{Coil} = \frac{d\lambda}{dt}$, yields:

$$W_c = \int_{t_1}^{t_2} \frac{d\lambda}{dt} i dt = \int_{\lambda_1}^{\lambda_2} i d\lambda \tag{3.59}$$

For such linear systems, the relationship between flux, λ, and current, i is often expressed as the coil self-inductance, L as:

$$L = \frac{\lambda}{i} \tag{3.60}$$

Inductance is analogous to mechanical inertia or mass as it resists any change in current due to an applied voltage, just as a mass resists a change in acceleration due to an applied force. If the system is excited from $\lambda_1 = 0$ and experiences no losses other than those from resistive heating, the stored field energy may be expressed as:

$$W_c = \int_0^{\lambda} i d\lambda = \frac{1}{2} L i^2 \tag{3.61}$$

The magnetic flux through a multi-turn system can also be approximated as:

$$\phi = \int_A \boldsymbol{B} \cdot dA = B A_{path} \tag{3.62}$$

where A_{path} is the normal cross-sectional area of the flux path, assuming the flux density is uniformly distributed along the flux path. Uniform distribution is likely to occur in devices with a ferromagnetic cores with linear relative permeability, μ_r, that tend to constrain the field to within the material. By taking advantage of the linear permeability relationship, $B = \mu_r H$, flux can be related to the material properties and field intensity, H as:

$$\phi = \mu_r H A_{path} \tag{3.63}$$

Note that for nonlinear or saturable materials $\mu_r = \mu_r(H)$. H can be related to the number of turns of the coil, N, the current, i and the length of the flux path, l by:

$$H = \frac{Ni}{l} = \frac{M}{l} \tag{3.64}$$

where M is known as magnetomotive force, or MMF. Equation 3.63 can now be rearranged as:

$$\phi = \frac{\mu_r A_{path} N i}{l} \tag{3.65}$$

This expression can be used to discretize the geometry and material of a linear magnetic device which results in a network of regions that can be solved in a similar fashion to a classical circuit analysis. Thus, flux for a device consisting of several different linear materials in series can be expressed as:

$$\phi = \sum_{i=1}^{n} \frac{\mu_i A_i N I_i}{l_i} \tag{3.66}$$

In these cases, each of the elements are analogous to resistors in an electric circuit. In magnetic terms, they are cumulatively known as the system reluctance, $\Re$, where

$$\Re = \frac{M}{\phi} = \frac{Hl}{\phi} = \frac{Bl}{\mu_r \phi} = \frac{l}{\mu A} \tag{3.67}$$

or by definition of inductance, $\Re = \frac{N^2}{L}$. Note that in devices with air gaps, it is often possible to neglect the reluctance of materials with high permeability much in the same way the resistance of wires in an electric circuit can often be neglected. Consequently, for devices such as solenoids, flux linkage, $\lambda = \lambda(x, i)$, is highly dependant on the air gap, or position of the armature, as well as current excitation or MMF. Flux can finally be stated as:

$$\phi(x, I) = M \sum_{i=1}^{n} \frac{1}{\Re_i} \tag{3.68}$$

Where the magnetic system is discretized into n regions of unique reluctance elements, $\Re_i$.

3.5.1 Magnetic Force Calculation

Consider a singularly excited magnetic system with an armature separated by an air gap, x. The steady state representation of this system may be expressed by Equation 3.54 with the electric circuit term omitted. If the armature is slowly displaced a small amount over a constant current, the energy exchange may be expressed as:

$$F_{avg} \Delta x = -\frac{1}{2} i^2 \Delta L \tag{3.69}$$

The change in inductance is dominated by a change in air gap, or position. Therefore, force may be expressed as:

$$F_{avg} = -\frac{1}{2} i^2 \frac{\partial L}{\partial x} \tag{3.70}$$

and may be used as an approximate expression for magnetic force at a given position.

3.5.1.1 Maxwell Stress Tensor

One method that ANSYS uses to calculate armature force is the Maxwell Stress method. The nodes surrounding the armature region are flagged for this calculation. Flux density values are numerically integrated over the element surfaces that are in contact with the air region. For the 2D case, the force for one element is calculated as follows:

$$\boldsymbol{F} = \frac{1}{\mu_0}\int_S \begin{bmatrix} B_x^2 - \frac{1}{2}|B|^2 & B_xB_y \\ B_xB_y & B_y^2 - \frac{1}{2}|B|^2 \end{bmatrix} \begin{bmatrix} n1 \\ n2 \end{bmatrix} dS \tag{3.71}$$

where B_x and B_y represent normal and tangential tensor components of $\boldsymbol{B}$ for an x-y cartesian coordinate system. The respective horizontal and vertical surface normals are represented by $n1$ and $n2$. Or perhaps more practically, the normal force component (of primary interest as the armature is constrained horizontally anyway) may be expressed as:

$$F = S\left(\frac{B_y^2}{2\mu_{Armature}} - \frac{B_y^2}{2\mu_0}\right) \tag{3.72}$$

Where S represents an armature-air surface area and $\mu_{Armature}$ is the armature steel permeability. The forces from exterior armature elements are then summed to obtain the net armature force.

3.5.2 Magnetic Response

Due to the relatively fast valve flight time (3-4ms), actuator response is of great concern to the design of an armature position control system. Electromagnetic response is strongly related to system inductance. The inductance may be calculated by forming a simple expression for a magnetic core of flux path length ℓ_{iron}, air gap of length ℓ_{air}, flux area A_{path}, magnetic iron permeability μ_{iron}, and free space permeability μ_0 as:

$$L = \frac{\mu_0\mu_{iron}A_{path}N^2}{\ell_{iron}\mu_{air} + \ell_{air}\mu_{iron}} \tag{3.73}$$

Equation 3.73 gives an indication of the importance of the various terms of the inductance magnitude. A higher inductance opposes current changes and thus increases the response time of the coil current and consequently the magnetic force. For this system, as the gap decreases the inductance increases (reluctance decreases). If a simple model of coil resistance and inductance is used and eddy currents are ignored, then Faraday's law and Kirchhoff's 2nd law may be used [Roters, 1941] to show:

$$V = iR_{coil} - L\frac{di}{dt} \tag{3.74}$$

Where V is the applied coil voltage, i is the coil current and R_{Coil} is the coil resistance. The solution of which with respect to current $i(t)$ is

$$i(t) = \frac{V}{R_{Coil}}(1 - e^{-\frac{t}{\tau}}) \tag{3.75}$$

In this way, current i may be expressed as a function of a time constant $\tau = L/R_{Coil}$. Additional effects that reduce the ability to change the magnetic force are eddy currents which, especially at small air gaps, inhibit response time. They may be accounted for through the use of FEA techniques, thereby increasing performance prediction accuracy, and their effects can be minimized practically through the use of laminated construction techniques and highly resistive yet permeable materials.

3.6 Simulink Implementation of a Lumped Parameter Model

Traditionally a lumped parameter model (LPM) consisting of multiple ordinary differential equations is used for electromechanical system performance prediction. LPMs often consider the individual systems as conservative and calculate only the terminal parameters such as voltage, current and force rather than field expressions [Woodson and Melcher, 1968]. As a result, they often neglect material saturation,

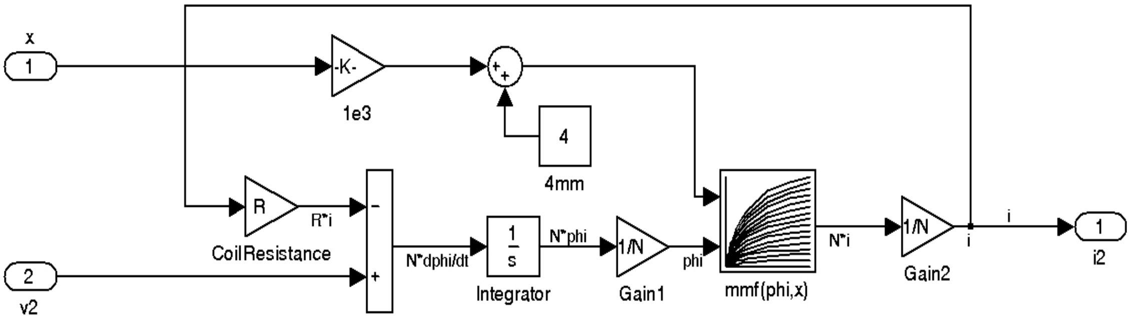

Figure 3.3: Simulink Coil Dynamics Model

nonlinear field effects and eddy current losses. However, the method offers a means of predicting the entire system response without the burden of a field analysis and can be easily incorporated into control design studies.

As a means of hybridizing the accuracy of a field solution with the expedient solution time and flexibility of a LPM, a MATLAB-Simulink model of the actuator circuit and mechanical dynamics was implemented. Figure 3.3 represents a block diagram where for a specified voltage, V, and initial armature position, x, Simulink numerically integrates Faraday's equation, specifically, the change in flux, $\frac{\partial\lambda(i,x)}{\partial t}$ to derive flux linkage, λ. Position and flux linkage are used in a lookup table (generated from FEA analysis) to predict a corresponding coil current. The current is then used in another lookup table for the same position to determine armature magnetic force. This force is used in a differential equation represented in Figure 3.4. Spring and inertial forces are subtracted and the resulting acceleration is subsequently integrated to solve for armature velocity and displacement. Simulink has a variety of solvers available to numerically integrate. For the LPM in this study, only the fourth order, adaptive step size Runge-Kutta solver ode45.m was used with a solution tolerance of 1×10^{-5}.

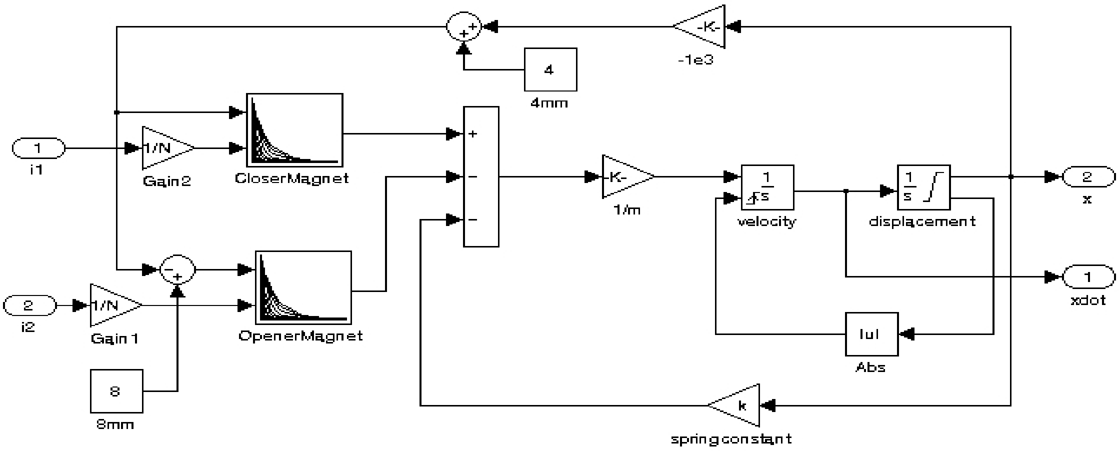

Figure 3.4: Simulink Mechanical Dynamics Model

3.7 Summary

The preceding sections briefly summarize the key analytic and numerical tools and assumptions used during the course of the actuator modeling and analysis. Specifically, Maxwell's general equations are subjected to the quasi-static limit and the magnetic vector and electric scalar potentials are used to provide differential equations which govern air and iron regions of a 2D system. ANSYS applies these equations over discretized regions and assembles them into a system of equations which are then solved using a Newton-Raphson procedure. The FEA results will later be contrasted with an equivalent model based on linear theory and assumptions. As well, a dynamic Simulink LPM was implemented using ANSYS generated results. The remaining chapters will discuss the details and contrast the results of these models as a means of validating the LPM used.

Chapter 4

Experimental Setup and Apparatus

4.1 Introduction

The following describes in detail the procedure and equipment used for the modeling and experimental testing of an existing electromagnetic prototype actuator.

4.2 Actuator & Valve

Five valve actuator prototypes were donated by DaimlerChrysler for experimental use. The prototypes are of the two-spring, flat-faced armature configuration commonly proposed by designers. Figure 4.1 illustrates a partial sectional view of a typical actuator and valve assembly. The opener is the coil and back iron portion of the actuator responsible for opening the valve. It should be noted that only the opener portion of the actuator was experimentally tested. This is due to the difficulty in fabricating a nondestructive load cell-to-actuator adaptor capable of measuring the high tension loads that will be experienced at low air gaps, while simultaneously accommodating the opposing return spring force. In addition, the experimental testing is only intended to validate the the FEA, not to evaluate the actuator performance in its entirety.

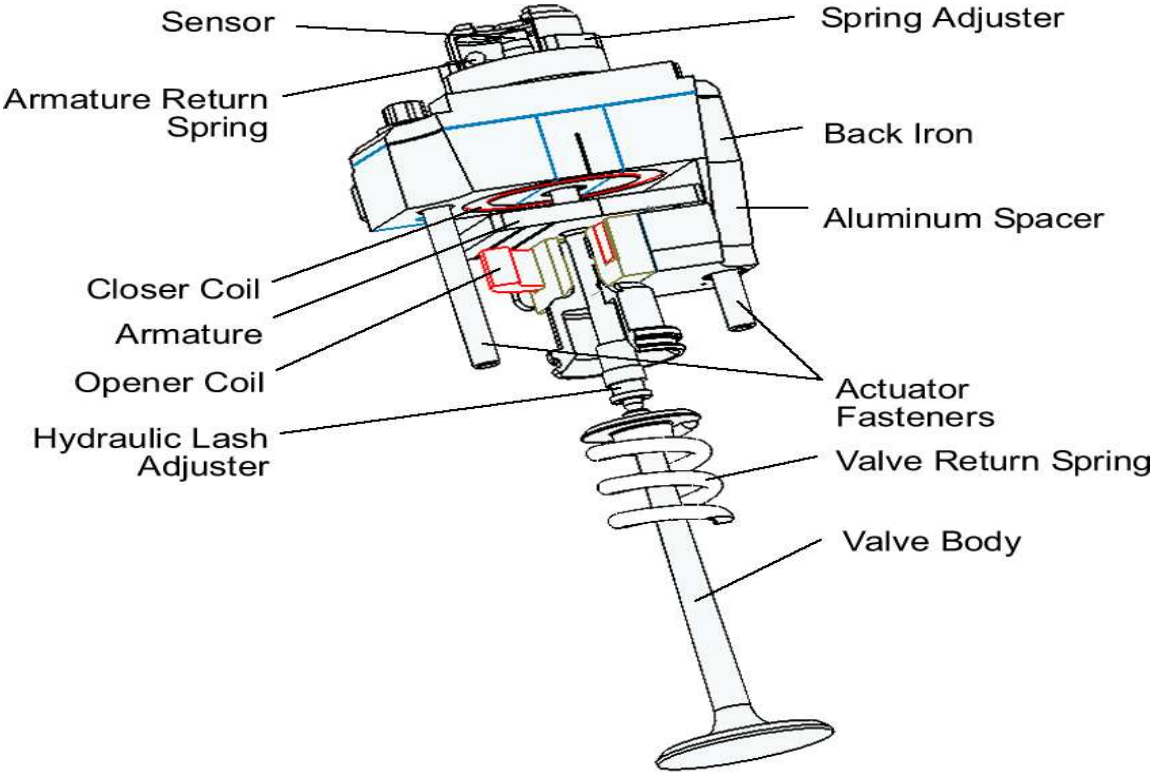

Figure 4.1: Actuator and Valve Partial Sectional View

4.3 Computer Software & Hardware

In order to predict actuator performance, a Finite Element model was implemented using the commercially available software, ANSYS (versions 5.7 and 6.1) by ANSYS Inc. The lumped parameter model was built in the MATLAB 6.0 - Simulink 4.0 environment. Both software suites were run on a 300W ATX desktop computer consisting of an AMD Athlon XP 1800 (1.53GHz) CPU, 1.0Gbyte of RAM using a Microsoft Windows 2000 operating system.

4.4 Equipment & Experimental Setup

In order to test the validity of the static and transient FEA, two experiments were designed to measure steady state force for a specified current excitation and a transient

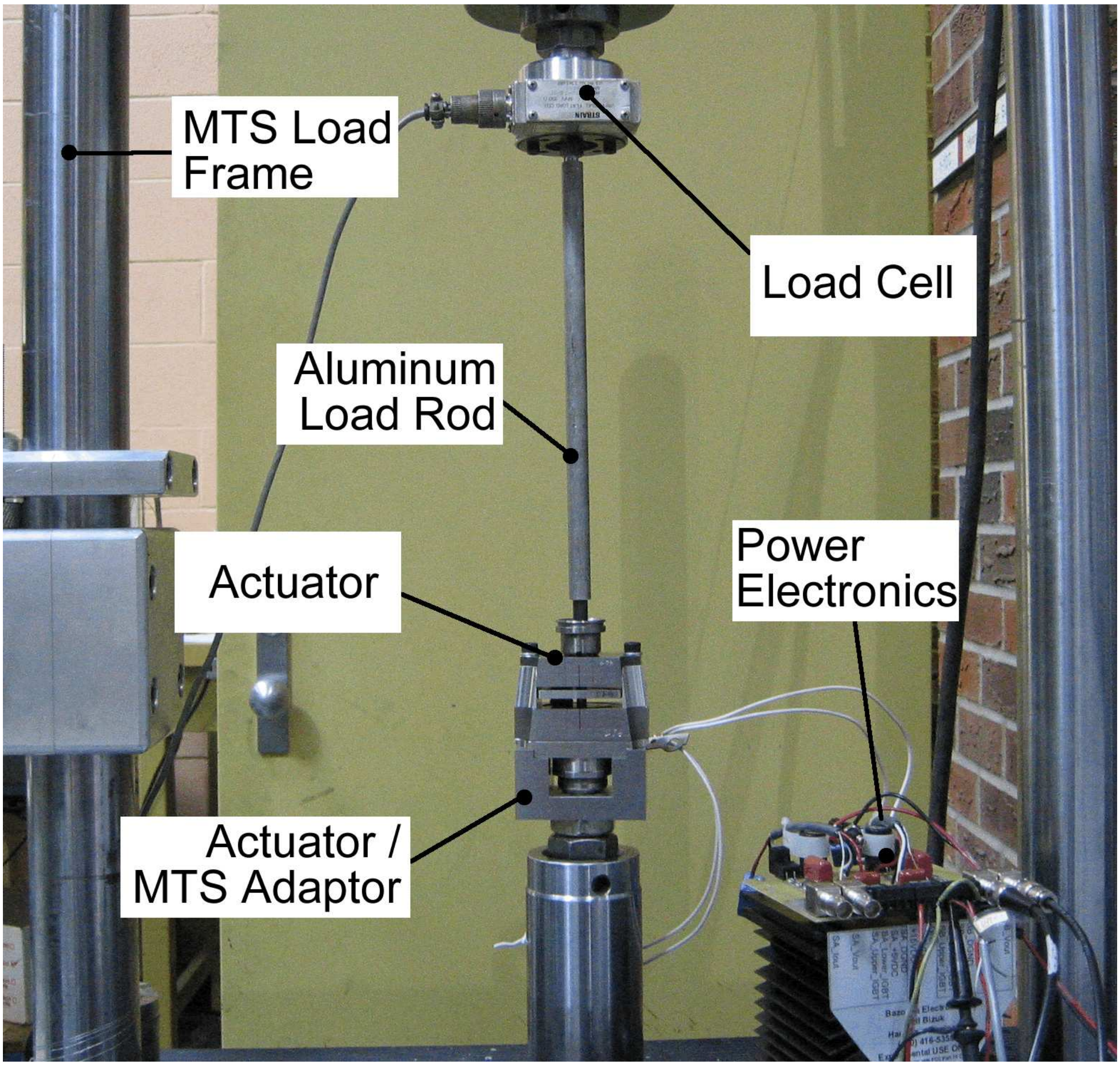

Figure 4.2: MTS Experimental Setup

force and current response to a step voltage input. Figures 4.2 and 4.3 illustrate the equipment setup and layout. Table 4.1 provides general specifications of the equipment used for both the static and transient cases.

4.4.1 MTS Axial Load Testing Machine

The MTS machine that was used for all experimental testing is located in the Mechanical Testing Laboratory on the main floor of the Mechanical Engineering Building

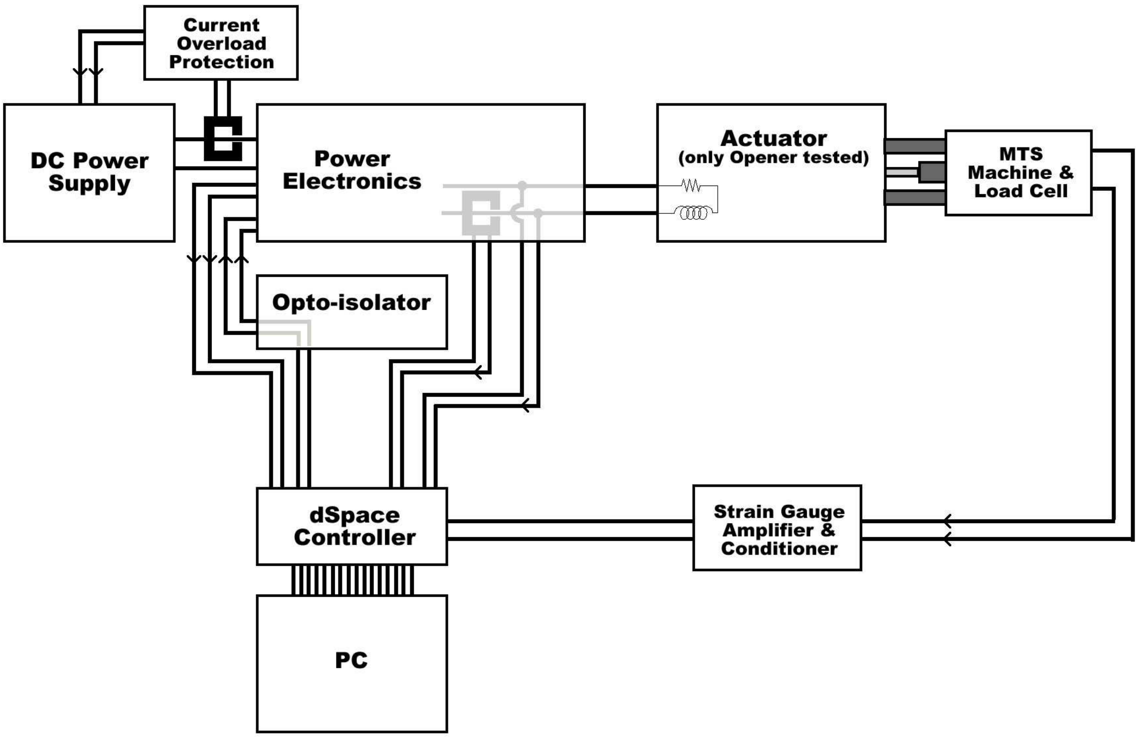

Figure 4.3: Schematic of the MTS Experimental Setup

at the University of Alberta. The axial displacement control capability of the MTS machine was used in all tests. The MTS load frame brace was adjusted to allow for ample clearance for the Actuator-MTS Load Rod, load cell and Load Cell-MTS Adaptor to be installed. After the rod, load cell and adaptors were installed into the MTS load frame, the armature position was set by the manual position control knob on the MTS Control Unit. Upon sufficient change in displacement, the actuator armature stem contacts the fixed load rod. Further change in the MTS crosshead position overcomes the return spring force and displaces the armature to a desired position. Great care should be taken to not exceed the actuator 8mm stroke limit to prevent the MTS setup from severely damaging the actuator. Specific positions are set by inserting feeler gauges between the armature and the opener pole face while manually adjusting the crosshead position until the gauges can be precisely inserted and removed from the resulting air gap. It should be noted that due to manufacturing tolerances of the actuator, a difference in air gap of $0.076mm$ could typically be measured from one side of the armature to the other.

4.4.2 Actuator Adapter

An adapter that attaches the actuator to the MTS crosshead was designed and fabricated from AISI 1024 steel. The actuator was attached to the Actuator-MTS Adaptor using two socket-head cap screws and secured to the MTS crosshead with steel ready-rod and a locknut.

4.4.3 Load Cell and Rod

In order to measure armature force, a Strainsert FL1U-2SGKT flat strain gauge load cell was installed on the MTS load frame. Due to the observed sensitivity of the load cell to magnetic fields, a rod that transfers force from the armature to the load cell was fabricated. The distance between the unloaded load cell and the operating actuator was increased until no detectable interference was observed in the load signal. This approximate distance was used for the length of the rod. As short of a length of rod as possible was desired to minimize the amount of deflection of the rod during loading. Aluminum was chosen over steel as the construction material to minimize a flux path to the load cell. The load cell strain gauge bridge was balanced and conditioned using a Vishay 2100 strain gauge conditioner and amplifier system. Gain was set to provide an output of 2.2mV/N (10mV/lbf). Calibration of the load cell was performed using another load cell which had previously been calibrated with a proving ring.

4.4.4 dSpace 1103 Controller

The dSpace control card provides the ability to coordinate sophisticated control systems and perform analog to digital measurements. The controller software provides a library which may be incorporated directly into the Matlab-Simulink environment. Such a capability is particularly useful as a developed LPM and control system can utilize the hardware library directly, minimizing the time spent translating the theoretical LPM into a low level hardware program. The dSpace card also makes use of a signal input/output break-out board. This device provides a efficient means of interfacing standard connectors with the controller. Aside from making instrumentation easier, this is also useful when debugging software and hardware. The controller card connects to a passive backplane ISA extension PC which is then connected to a host PC through two optical PCI communication cards. This backplane and additional PC was required as the dSpace 1103 is available only with ISA bus compatibility due to the higher current demands of the controller. Unfortunately, the ISA bus standard has become largely unavailable for modern desktop motherboards. Otherwise, the dSpace controller could be mounted directly in the host PC.

4.4.5 Sorensen Power Supply

Actuator power was provided with a Sorensen DCS60-18E 1kW programmable switching power supply. The supply converts a standard 120VAC 60Hz line source into a variable DC power source. The supply is remotely shutdown through a connection to an external overload circuit that monitors the supply current output. Although the supply output is rated to maximum 18A of continuous current, it was observed that the supply was capable of providing short term (5ms or less) currents in excess of 50A at 50V. This allowed the measurement of the actuator over an extensive operation range.

4.4.6 Circuit Protection

To prevent the significant levels of current to flow unchecked through the actuator, an overload circuit was constructed. The circuit measures and low-pass filters the coil

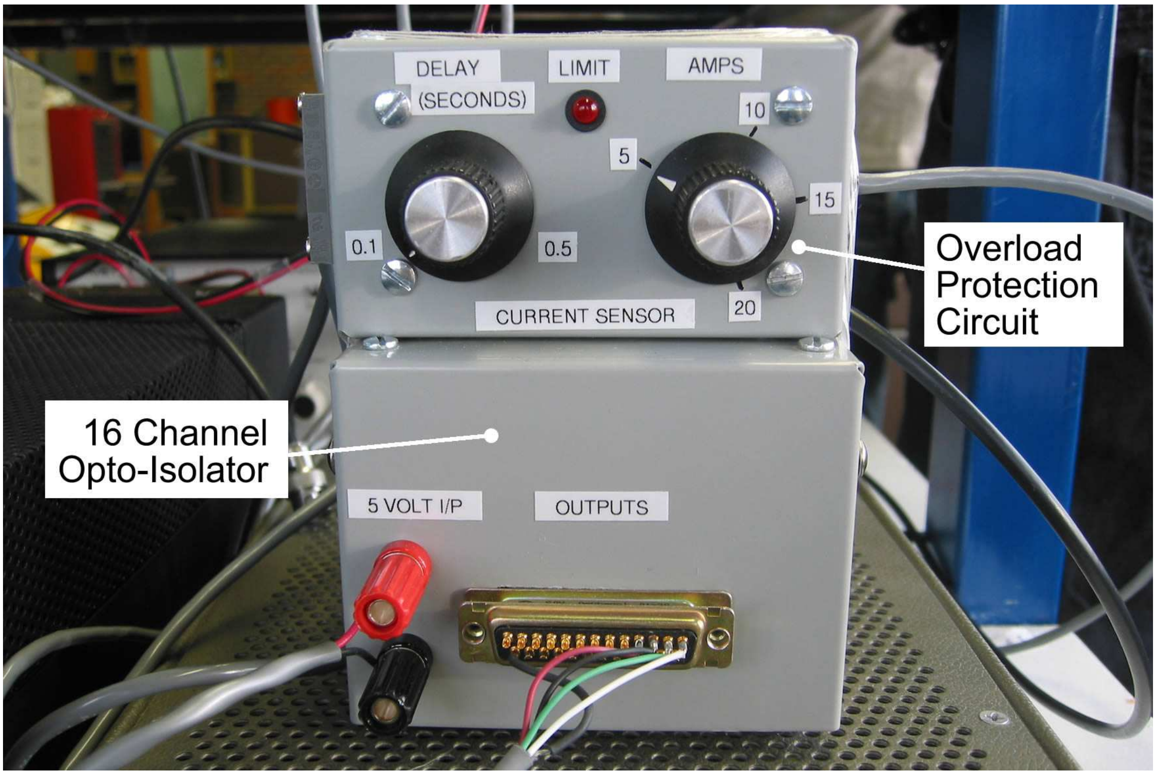

Figure 4.4: Opto-Isolator and Overload Protection Circuits

current and generates a signal to the power supply when the low frequency current exceeds a shutoff limit (in the event of a software or power electronics error). This avoids destroying the actuator coil in the case of a system failure. The output lead from the Sorensen power supply to the power electronics is measured using a Hall-effect current sensor. The shutoff threshold is manually adjusted to allow a suitable current limit. It was also deemed necessary to protect the dSpace control card and computer from potential electrical spikes or surges that may originate from an actuator or power electronics failure. Thus, all switch signals from the dSpace controller to the power electronics are optically isolated using an opto-isolator circuit. Both the overload circuit and opto-isolator require a DC power source which is provided by a HP 6236B triple output power supply. The analog force, current and measurement lines from the Vishay 2100 and power electronics were connected directly to the dSpace input/output board. Similarly, switch signals from the opto-isolator are measured directly due to the relatively low voltage and current inherent to TTL or PWM signals. Figure 4.4 illustrates both devices. Electrical schematics of both devices are provided in Appendix B.2.

4.4.7 Power Electronics

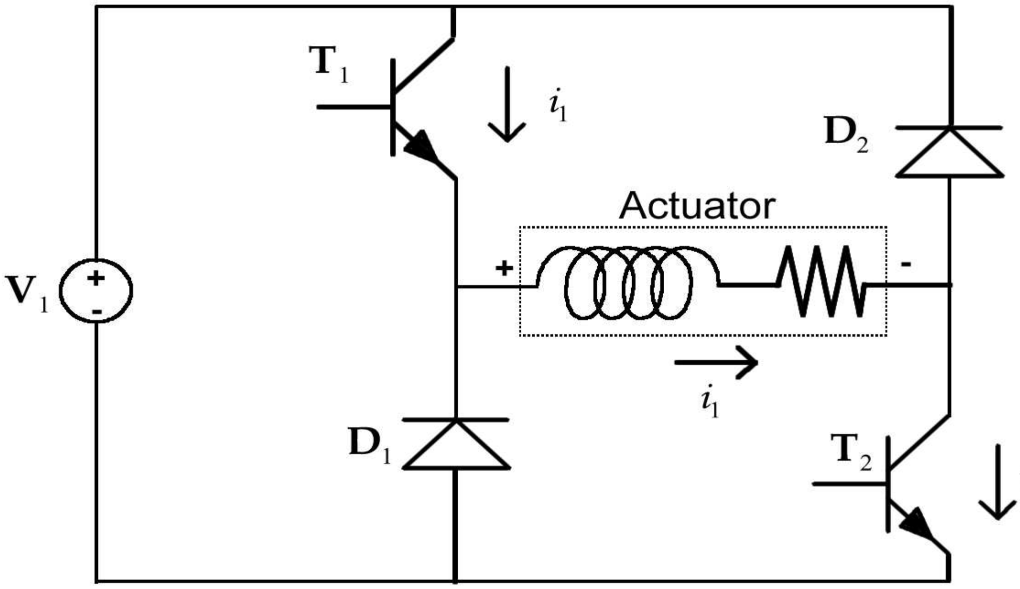

Figure 4.5: Power Electronics in +42V Mode

Custom H-bridge power electronics were designed and built by Bazooka Electronics Ltd. to supply the actuator with the necessary electrical power in a coordinated and repeatable fashion. The actuator opener coil, opto-isolator signal lines, voltage and current measurement lines as well as the Sorensen and HP power supplies were connected to the custom power electronics. The positive actuator coil lead is passed through the Hall-effect current sensor of the power electronics. These electronics will

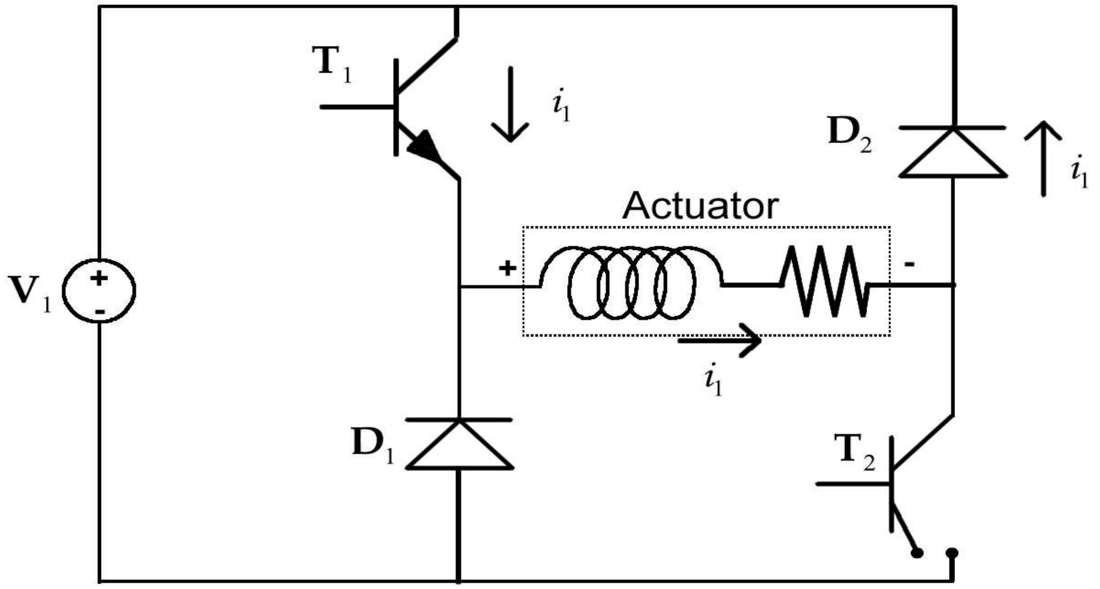

Figure 4.6: Power Electronics in 0V Mode

also be used in future test-bench and internal combustion engine experiments.

The electronics provide three basic output modes of +42VDC, 0VDC and −42VDC to the coil. These three modes are achieved by switching two transistors of an H-bridge power circuit. Figure 4.5 schematically illustrates the power electronic circuit in +42V mode. Transistors T1 and T2 are closed and current flows from the power supply, through the actuator and to ground. This mode is used to switch the actuator on.

Figure 4.6 schematically illustrates the power electronic circuit in 0V mode. After the coil is energized to a pre-specified level, transistor T1 is closed and T2 is opened. This results in a net potential difference across the actuator of 0VDC. Coil current rise stops and recirculates or ‘freewheels’ through the diode, D2, until it drops below a threshold level, at which time the coil is usually switched back on.

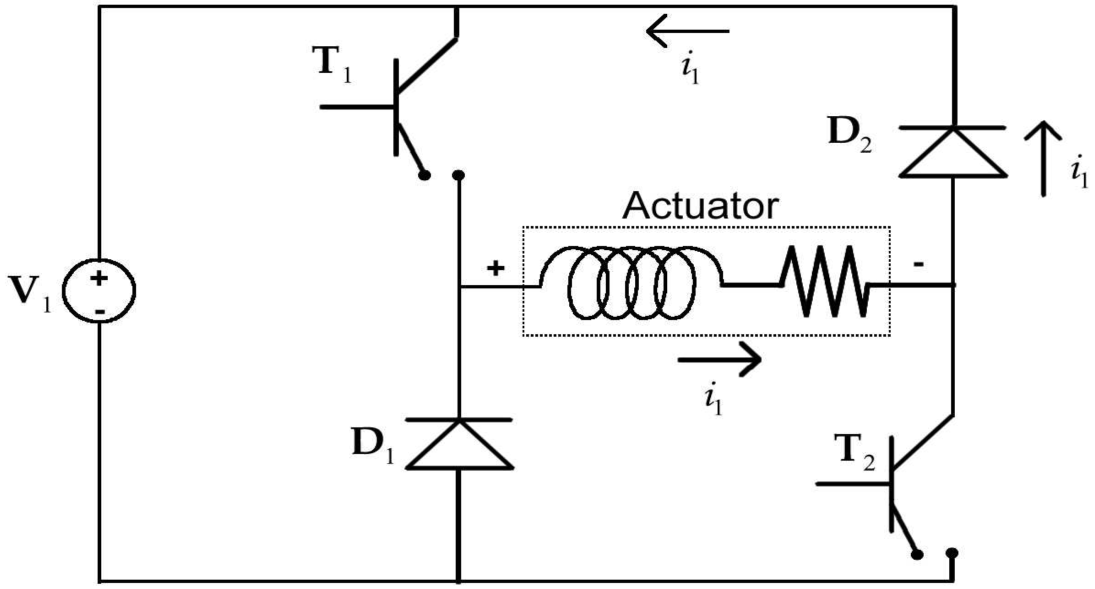

Figure 4.7: Power Electronics in −42V Mode

Figure 4.7 schematically illustrates the power electronic circuit in −42V mode. After the coil is energized the net potential difference across the actuator is now −42VDC. In this mode, transistor T1 is open and current is driven down (usually until zero) at a faster rate than the 0V mode due to the effective change in polarity. It should be noted that when T1 is open, the mode is the same regardless of the state of T2. This mode is used to switch the actuator off in a more expedient way than the 0V mode. This mode would be used when releasing the armature in order to reduce the magnetic force quickly and subsequently achieve faster valve travel time.

4.4.8 Current and Voltage Sensing

Both coil voltage and coil current signals are generated on-board the power electronics. Coil voltage is inferred by dividing the coil voltage with a differential operational

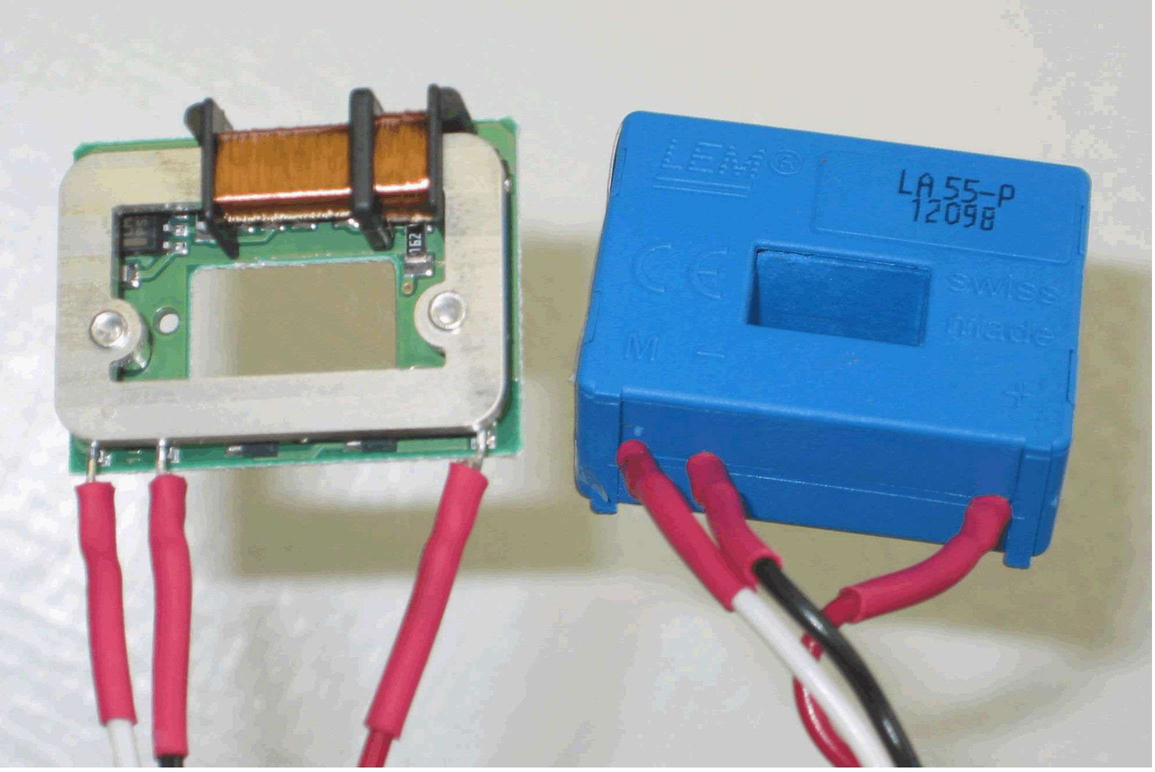

Figure 4.8: Current Sensor

amplifier circuit. The value of the gain and resistors are chosen such that the output voltage is a convenient fraction of the actual voltage across the coil.

For both the case in the overload protection circuit and the power electronics, current is measured with an off-the-shelf Hall-effect current sensor. The Hall-effect current sensor works by directing the magnetic field produced by a flowing current, given by $B = \frac{\mu_o I}{2\pi r}$, into a semiconducting material using a steel yoke. When a semiconducting material is exposed to a magnetic field, it produces a measurable current and voltage in proportion to the impinging field as predicted by the Hall-effect phenomenon. In order to avoid the nonlinear behavior of the yoke and the semiconducting material itself, an operation amp maintains a feedback loop by using a coil that generates an opposing magnetic flux in the yoke in proportion to the output of the semiconducting material. Thus, any flux produced by the current intended to be measured is equally

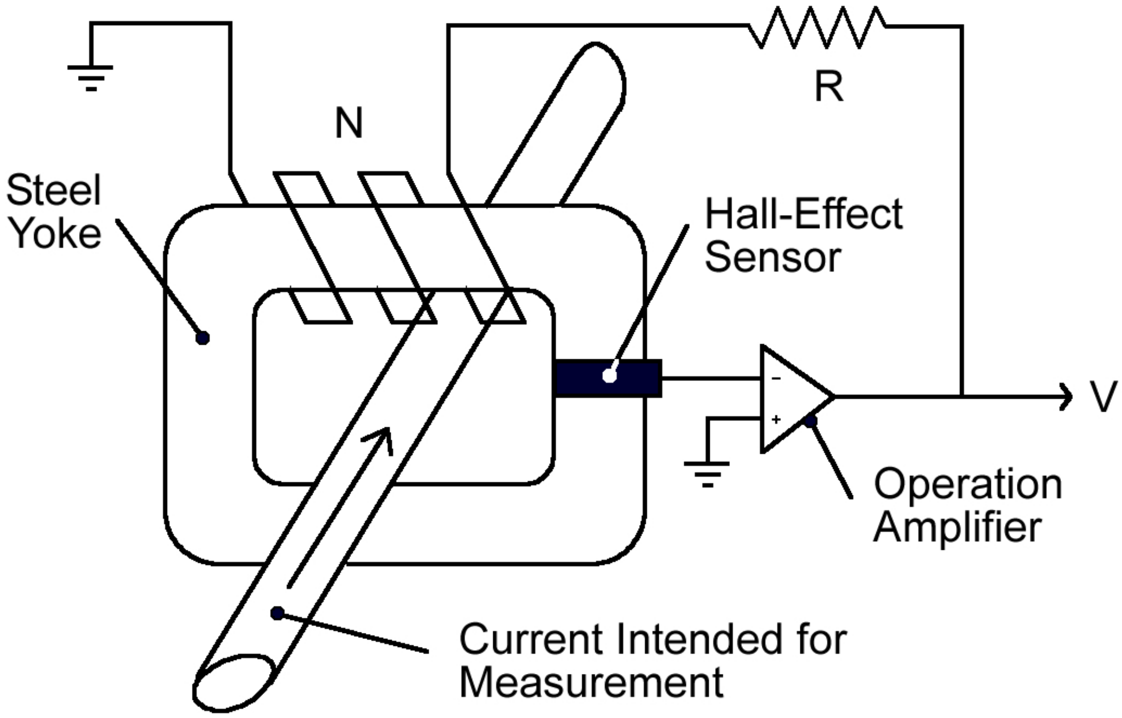

Figure 4.9: Current Sensor Schematic

countered by the flux produced by the op-amp driven coil. The counter flux is generated by passing the op-amp current through a resistor and, N, external loops around the yoke. The operation amplifier voltage is then measured since it is proportional to the current required to balance the magnetic flux produced by the line current. It is then possible to relate the op-amp voltage to the current flowing in the conductor by $V = \frac{I_{Measured}R}{N}$. Figure 4.8 shows the actual current sensor and Figure 4.9 illustrates the sensor schematically. Note that large currents can be measured because it is possible to cancel the generated flux with a small current by using a large number of turns about the steel yoke.

4.5 Static Experimental Setup

For the steady state force measurements it was necessary to actively control the actuator current input in a repeatable fashion. This was done through pulse width modulation (PWM) and the power electronic current sensor as feedback. By sending appropriate switching signals, the dSpace controller allows the measured coil current to rise to a specified level and then switches the power electronics to the 0V mode. The power is switched on again when the current drops below a threshold level. Controller switch signals, actuator coil voltage, coil current and load cell signals are all recorded with the dSpace controller at a sample rate of 50kHz. The power electronics, opto-isolator and the dSpace controller are all capable of producing a PWM carrier frequency of 50kHz. However once the actuator coil reaches steady state excitation and power is switched off, the current dissipates slowly enough that it is not required to switch on again during the 50ms measurement period. Data recording was triggered with the measured coil voltage signal. All measured signals were saved in comma separated format as well as Matlab binary files. Force and current data were scaled, analyzed and recorded for comparison to the steady state FEA opener model results. The naming convention of all data files are listed in Appendix D.

4.6 Transient Experimental Setup

In order to investigate the accuracy of an ANSYS transient model, several experiments were conducted that measure actuator force and current response to a stepped voltage input. The air gap is adjusted and the dSpace controller and power electronics switch on and off the power to the actuator coil. The process is repeated by adjusting the power supply voltage to 24V, 42V and 50V over several air gaps. As no current control is required, the input signal to the transient experiments is simpler than those of the steady state experiments using the H-bridge power electronics. Caution should be exercised when selecting the duration over which the actuator is switched on as current is now only limited by the power supply output and Ohm's law, thereby making it possible to melt the coil. The overload circuit and power supply should be conservatively limited prior to testing. Once the power supply current and overload protection are limited, pulse duration can gradually be increased to allow for a suitable force and current profile. Only then, should the power supply current limit and overload circuit protection be relaxed as necessary. Pulse duration was typically set to 1.5ms. Note that current will rise faster at larger air gaps due to the lower inductance of the magnetic circuit. It is therefore recommended that pulse duration be set at the largest air gap that is to be tested. Data recording was triggered with the measured coil voltage signal. Coil voltage, current and force data were scaled and recorded in comma separated format for comparison to the transient FEA opener model results. Again, the naming convention of all data files are listed in Appendix D.

4.7 Dynamic Experimental Setup

An experimental test platform was constructed to evaluate the LPM accuracy and physically test the actuator control system prior to implementation on a single cylinder research engine. The experimental test setup is shown in Figure 4.10 and illustrated schematically in Figure 4.11. The actuator is fastened horizontally into an aluminum mount which apposes the valve assembly. The valve assembly consists of the valve body, return spring pressure cavity and eddy current displacement sensor. A cavity can be pressurized with compressed air to simulate combustion pressures. The actuator mount and valve assembly are fastened to a steel stage which allows for relative horizontal displacement adjustment between the two assembles. The adjust-

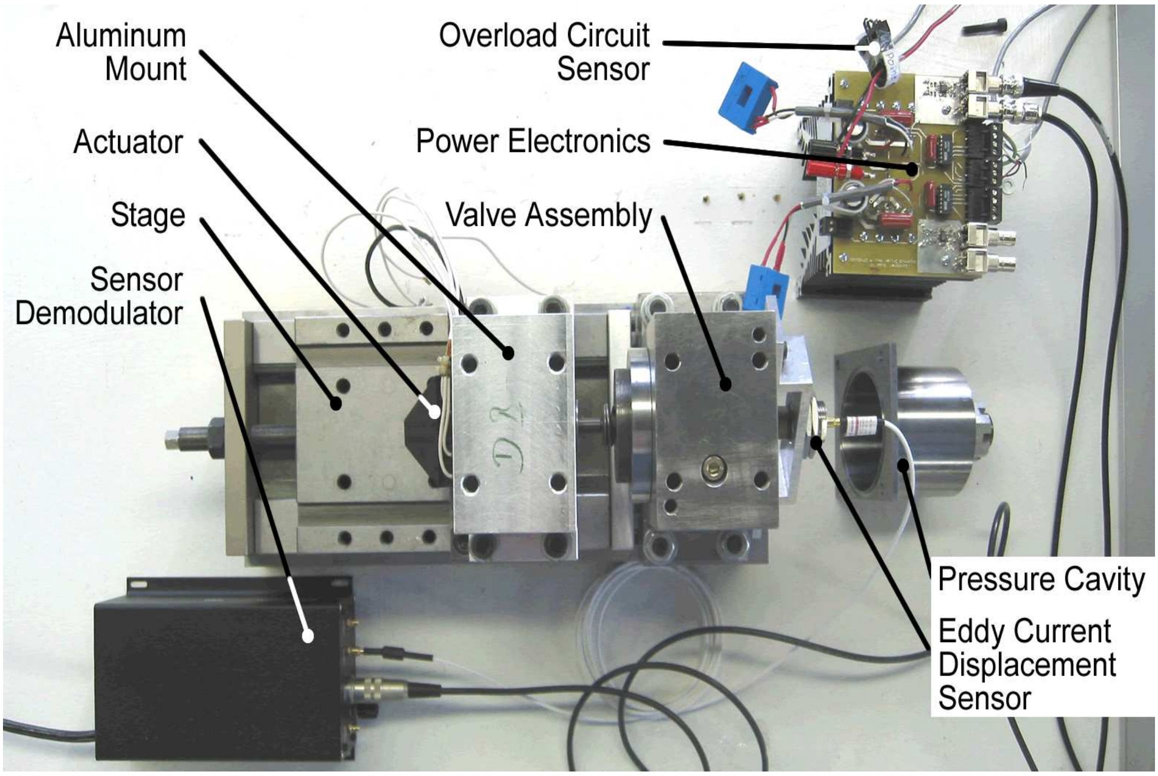

Figure 4.10: Experimental Test Bench Setup Schematic

ment is required to ensure proper valve to actuator contact as well as provide testing flexibility such as the possible incorporation of a hydraulic lash adjuster. Between the work table and the steel stage is a steel mounting slab and a layer of neoprene rubber to assist in damping vibrations from the actuator to the experiment surroundings. The steel mounting slab is bolted through the steel members of a custom work table. If necessary, spring isolated fasters may be employed to further isolate unwanted vibrations. Again, the actuator is to be controlled by the dSpace control card and power electronics. This experimental testing will not be undertaken until the continuing control system development is complete.

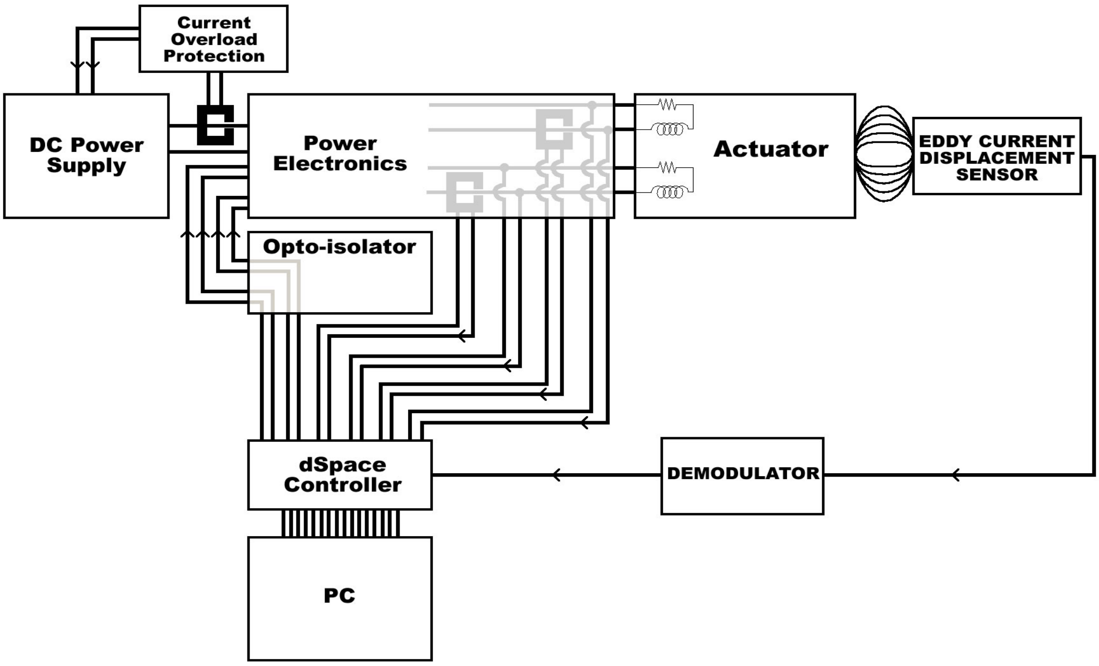

Figure 4.11: Test Bench Setup Schematic

4.8 Summary

The above sections provide a brief summary of the hardware and procedure used to conduct the experimental and numerical studies performed. An ordinary desktop computer was used for conducting the FEA and LPM studies. Custom H-bridge power electronics were interfaced with a switching power supply and high speed controller to supply the prototype actuator with an appropriate power. Actuator force was measured with a load cell and MTS load and controller apparatus. An actuator test-bench was also constructed as a means to simulate an engine environment for control development.

Table 4.1: Static and Transient Experimental Equipment

Item	Description	Relevant Specifications
Prototype Actuator	TEMIC Linear actuator 11997 provided by DaimlerChrysler	8mm (0.315") stroke
Actuator-MTS Adaptor	Connects the actuator to the MTS crosshead	AISI 1024 Steel
Actuator-Load Cell Rod	Transfers load from the armature to the load cell	13mm (1/2")ϕ x 300mm (12") 6061 T6 Aluminum bar
Load Cell-MTS Adaptor	Fixes the load cell to the MTS load frame	6061 T6 Aluminum
Actuator Power Supply	Sorensen DCS60-18E programmable switching power supply	0-60V, 0-18A Max output: 1kW
Accessory Power Supply	Hewlett Packard 6236B triple output linear supply for power and miscellaneous electronics	+6V, -20V and +20V output
Power Electronics	Custom H-Bridge driver for actuator current control with on board current hall-effect sensor	Switching to 50kHz Sensitivity: XV/A Cap.: 200V @ 70A
Load Cell	Strainsert FL1U-2SGKT flat load cell	Cap.: 4448N (1000lbf) Acc.: 1% FS
Load Frame	MTS 312.21 Axial Load Frame	Cap.: 100kN (22.5kip)
Load Controller	MTS 436 Control Unit position and load control	-
Strain Gauge Conditioner	Vishay 2100 provides load cell excitation and calibration	1-12V Excitation Gain: 100-2100
Feeler Gauges	Precision shims to measure air gaps	Res.: 0.001mm Acc.: ± 0.0005mm
Computer	Standard ATX computer for data collection and actuator control	1.53GHz CPU 500Mb RAM
Controller	dSpace 1103 I/O panel and Control Desk software	12Bit Sampling and switching to 50kHz
Misc. Electronics	Custom 16 channel Opto-isolator Variable overload protection	10Mbit/s $\leq$ 10ms response
Misc. Hardware	Various connectors, leads and fasteners to connect hardware	-

Chapter 5

Design Methodology and Modeling

5.1 Introduction

The following identifies electromagnetic gas exchange actuator constraints and proposes a development process intended to alleviate prototype construction for control system development. The design process indicates the need for an accurate and efficient method of predicting actuator performance. A method of incorporating the accuracy of a numerical field solution with the speed and flexibility of a lumped parameter model is demonstrated with an existing prototype and commercially available software.

5.2 Design Methodology

A proposed actuator development process is illustrated in Figure 5.1. Each block represents a distinct stage in the design and implementation processes as discussed below. Note that the focus of this thesis is on the derivation and use of FEA and lumped parameter models for control development, as indicated by the dashed outline in the same figure.

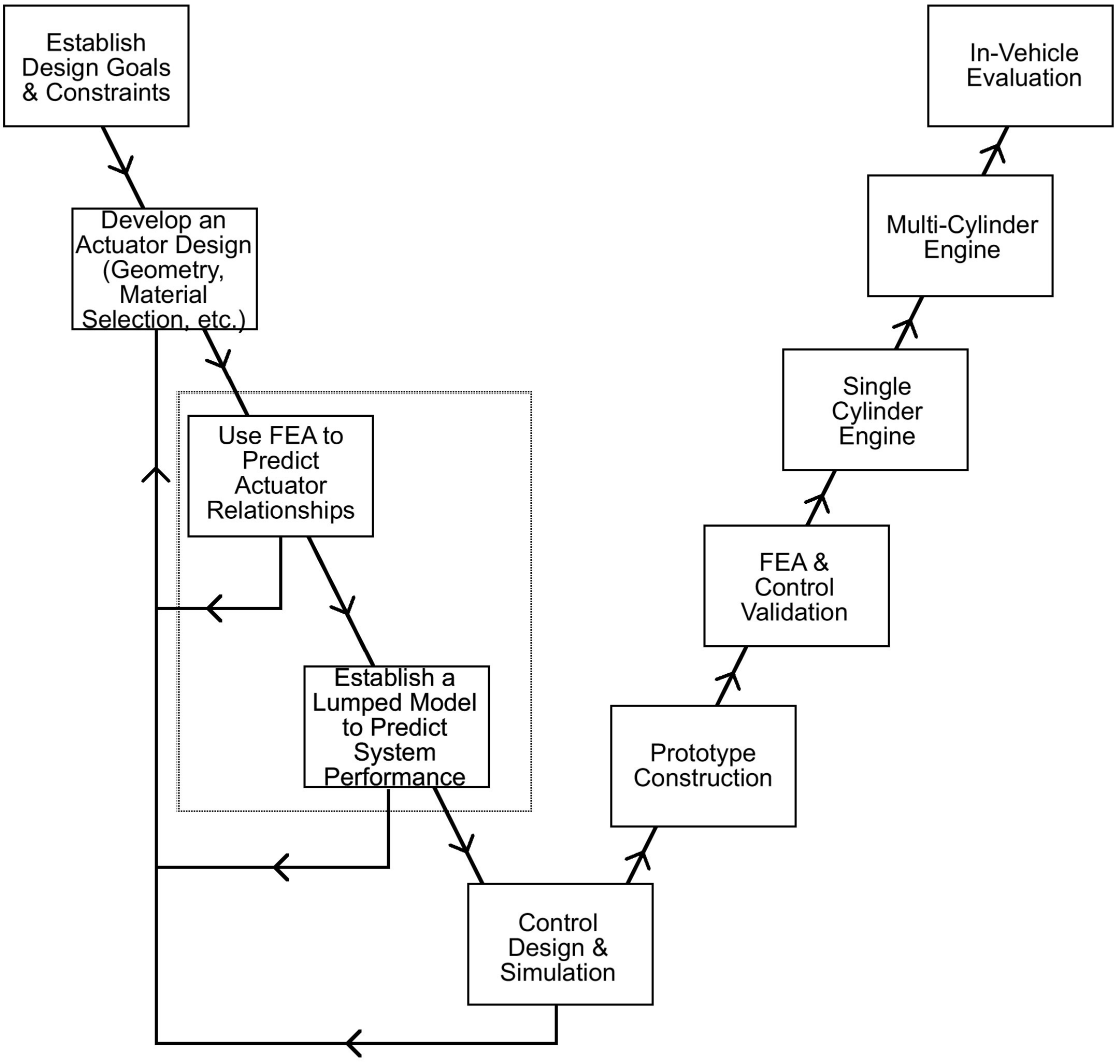

Figure 5.1: Overall Actuator Design and Implementation Process

5.2.1 Identifying Actuator Constraints and Requirements

Replacing the camshaft and associated components with electromagnetic actuators and electronics is a relatively large change from a conventional engine. Accordingly, the design of solenoid valves for intake and exhaust valves has many requirements which must be realized. For example, engine acoustic noise, maximum engine RPM, operational reliability and durability must all be comparable or improved with respect to the same parameters of a conventional combustion engine. The solenoid system must be implementable within existing engine blocks and under-hood environments. These conditions include mechanical fatigue and vibration, electric and magnetic noise in an environment with a temperature range of -40^{o}C to 160^{o}C. As well, selected material availability and design tolerance expectations must be consistent with realistic manufacturing practices. Engine emission standards and feasible implementation costs are also relevant design constraints.

These implementation constraints have been highlighted to illustrate the breadth of scope and complexity of the ensuing design challenges. How these challenges are translated into specific actuator performance requirements will ultimately determine effective design strategies. These requirements include valve travel times of 3-4ms over a minimum valve stroke of 8mm, corresponding to engine speeds of 5500RPM, while maintaining seating velocities of 0.1m/s or less at idle speeds. Vehicle packaging and cylinder spacing dictate a maximum allowable actuator volume. The actuator must also be compatible with on board 42 Volt DC power supplies, the emerging automotive standard. Cumulative actuator electric energy consumption must be minimized to maximize engine brake power and efficiency. Accordingly, the magnetic circuit configuration itself will ideally exhibit high electrical to mechanical energy conversion efficiency. Similarly, trajectory design and control of valve motion must be developed to minimize energy consumption. The system must be capable of functioning with rapid parameter fluctuations such as those experienced during a combustion ignition failure or misfire event. As well, the system must account for the relatively long term variations of friction and electromagnetic and mechanical material properties caused by temperature variations, spring stiffness and valve seat wear caused by 300,000km of vehicle operation. Additionally, the associated position sensor, power and control electronics ideally exhibit simplicity and robustness. Of course after addressing the above constraints, the initial motivation of improving fuel economy and decreasing emissions must be realizable to justify the design implementation.

5.2.2 Design Concept Development

As many of the critical design constraints have been identified, it is possible to develop an initial actuator concept. Using traditional analytic tools with idealized approximations, it is possible to derive a concept capable of qualifying the elementary requirements of volume, force, approximate valve travel time and cost constraints. A host of available materials may be identified for possible use. A computer 3D CAD model of the device will be created to ensure packaging and manufacturing constraints are satisfied. This CAD model may later be directly incorporated into a FEA study which optimizes mass, temperature rise or fatigue.

5.2.3 Design with FEA

There are several ways to predict magnetic actuator performance, namely, analytic, empirical and numerical. Analytical methods typically attempt to describe the magnetic system by taking advantage of highly ideal circumstances such as linear material behavior and simple geometry. Other phenomenon such as eddy currents or flux leakage must typically be neglected. In certain instances, a unique analytic solution is possible and, despite idealized assumptions, valid for general performance predictions. However, often the highly idealized assumptions prohibit accurate closed form solutions over an entire operating range for a detailed design to continue. For example, the determination of permeance of air gaps through the calculation of flux paths is limited to a few special geometric cases, as flux lines typically are not confined by a path that is easily expressed mathematically. As a result, the designer is typically restricted to a one or two dimensional analysis and must employ simplifying assumptions or use graphical techniques. However, these techniques are often inadequate when considering time dependant systems or complex 2D or 3D pole geometries. Further, in using such methods, the ultimate analysis will require a validation through comparison with an actual device or experiment. In other words, to perform a complete design, one may have to construct several prototypes resulting in an iterative empirical design process. The number of iterations will then be a function of the designer's aptitude at making assumptions and interpreting results. Such traits are underlying skills which often distinguishes an exemplary designer, at least in the initial stages of design. Even the best designer would agree that any reduction in the number of assumptions one must make will contribute to the reduction of the necessary design and prototype iterations. There are methods of analytically modeling some of the complex behaviors mentioned above, however they are often not comprehensive, overly complicated, time consuming, or not well suited to a semi-automated design procedure.

It is possible to reliably use data based on previously tested designs just as one might graphically interpolate / extrapolate a data set. Of course the closer the new design is to the models existing in the data base, the greater the probability in achieving accurate results. If a new or revolutionary design is to be implemented there is likely little data to compare it with and the results will have to be justified with prototype construction.

Although based upon analytic theory, a FEA field solution is achieved numerically, thus the solution is not exact. In addition, a level of expertise is required to conduct a FEA in the event of troubleshooting singularities and ensuring solution convergence, for example. The use of FEA may also require a significant amount of computing time and depending on the model complexity, may be prohibitive. The benefit of an FEA is that near exact solutions to problems with complex geometries, nonlinearities and time dependant boundary conditions are possible. For the magnetic valve actuator, a FEA model is capable of accounting for many of the nonlinearities of the magnetic system including transient coupled field problems. Although more computationally expensive, thermal, dynamic, magnetic and electric problems could be simultaneously modeled. Computational time is consistently being expedited with the advent of inexpensive yet powerful desktop computers. A field solution can provide qualitative results which may also be of use to the designer. Thus, for many circumstances a FEA permits an acceptable method of predicting actuator performance without prototype construction.

After a concept is obtained, preliminary FEA studies may be performed, such as structural, fatigue and thermal investigations to refine the design and perhaps indicate any significant deviations from the assumptions utilized in the initial design phase. Upon satisfactory performance, armature force and flux results can be generated over a grid of armature position and coil excitation values as a means of later predicting dynamic performance in a LPM. In this study, a prototype of typical configuration was obtained in order to validate an equivalent FEA and LPM. After the FEA and LPM techniques have been validated, they may be applied to a variety of actuator configurations with confidence. The details of this process will be discussed following this section.

5.2.4 Lumped Parameter Modeling

The nonlinear relations of force and flux as a function of position and current from the FEA are used in a lumped parameter model as a means of coupling the electrical and mechanical domain. This allows for simulation of the entire actuator valve system response to a voltage input. If it may already be ascertained that actuator performance is unsatisfactory, another opportunity is in place to modify the design and again generate new FEA data before prototype construction. The model is modular in nature to facilitate association with further studies.

5.2.5 Control Design

Next, a control scheme is incorporated and analyzed in conjunction with the lumped model. This stage of the actuator implementation process poses a host of challenging design considerations. These considerations include actuator frequency response, trajectory planning, actuator startup algorithms and identifying sensor requirements. The following highlights two other areas pertaining to control development.

5.2.5.1 Parameter Variations

For robust valve control, a learning feedforward and feedback control strategy will need to be imposed to restrict valve and armature impact velocities. In particular, a feedforward scheme will be required to adapt to different or changing system parameters. For example, during the manufacture of the devices there will be manufacturing tolerances of armature mass, spring stiffness, etc. How sensitive the control system is to these tolerances and how well it can adapt to variations is certainly of concern. Similarly, the damping coefficient can also be expected to change with oil temperature and the spring stiffness will change over the device useful lifetime due to fatigue. In contrast to the rapid disturbances due to combustion variations or failures being accounted for in the closed feedback loop, all of these changes occur relatively slowly with respect to the valve cycle, making it possible to adjust the overall system model recursively, provided the initial estimate of the parameters are within reason. One way of gaining insights of such parameter dependencies is to estimate the parameters from the measured input and outputs of the state variables force, displacement and velocity.

5.2.5.2 Mechanical Stability

The spring valve system is approximated by a mass spring damper system. The force exerted by the electromagnet may be expressed as a nonlinear function of the air gap, with a differential equation for the effective mass-spring system represented as

$$F_m(x, i) = m\ddot{x} + c\dot{x} + kx \tag{5.1}$$

where m is the moving mass, c is the damping coefficient and k is the effective spring stiffness. To analyze this system, Equation 5.1 is linearized about a particular air gap, x_0. The landing velocity and damping effects are assumed to be zero. Zero velocity may be justified as the real system requires control towards the end of the valve stroke at a very low impact velocity (0.1m/s). Damping in the analyzed system is low when the temperature is above 20^oC ($< 3\%$ per cycle). The system is linearized about the point $x = x_0 + \delta x$ by calculating the current required, i_0, for the magnetic force, $F_m = F_0$, to just balance the spring force. Thus, the magnetic force can be approximated as

$$F_m(x, i) \cong F_0 + \left.\frac{\partial F_m}{\partial x}\right|_{i_0} \delta x + \left.\frac{\partial F_m}{\partial I}\right|_{x_0} \delta I \tag{5.2}$$

For example, at a 1mm gap, a magnetic force of $F_0 = 537$N at $i_0 = 27$A is required for armature equilibrium. Now define $k_x = \left.\frac{\partial F}{\partial x}\right|_{i_0}$ and consider the current i_0 to be constant. By substituting the approximate force (Equation 5.2) into Equation 5.1 and letting $x = x_0 + \delta x$ and solving for δx yields:

$$0 = m\delta\ddot{x} + k\delta x - k_x \delta x \tag{5.3}$$

This is an equation of the perturbations of the solenoid system about a stationary point x_0, where the coil current i_0 and magnetic force are in static equilibrium with the spring force. Equation 5.3 resembles an unforced mass spring oscillator with mass, m, and spring force, $k - k_x$. The value of k_x is the slope of the magnetic force curve at a constant current and position, which, for this system is $k_x = -560$N/mm at $x_0 = 1$mm and $i_0 = 27$A. When $k_x > k$ the poles of this system are on the real axis with one pole p_u being unstable.

At an air gap of $x_{gap} < 2.3$mm, $k_x > k$ the system is unstable and the magnitude of the unstable pole increases with decreasing air gap. The physical interpretation of the open loop system poles are when the slope of the magnetic force exceeds the spring constant then the system is not stable to small displacement perturbations about an equilibrium. This has important implications on the control system. The physical constraints of a limited power supply and actuator volume constraints will also have important implications on the control system.

The LPM allows the opportunity to predict how the actuator and control system may respond to a variety of operating conditions and make necessary design changes. Note that after prototype construction, it becomes extremely difficult to make design changes without building a new prototype. It is for this reason that the design and simulation process is as rigorous as possible to discriminate potential design flaws prior to construction rather than after.

5.2.6 Prototype Construction

If successful control simulations are achieved, the selected actuator design is fabricated and assembled. Off the shelf accessories such as sensors and other application specific electronic hardware are acquired. Depending on design complexity, tolerances and selected materials, this process may be costly, especially when the actuator is produced in low quantities.

5.2.7 Prototype Implementation

After a prototype is constructed, it is tested in increasingly more realistic operating environments. Initially the prototype is mounted to a test bench that idealizes typical engine response. This allows the opportunity to refine any control parameters and hardware before operating in an engine where a failure could result in extensive damage to the actuator and engine alike. Upon successful test bench performance, prototypes are graduated through a laboratory single cylinder, multi-cylinder and finally onboard vehicle engines. During the course of these stages, engine performance may be monitored and used to evaluate and improve actuator and control performance. Advanced engine control schemes such as multi-cylinder cutout and timing strategies may also be implemented and evaluated.

5.3 Prototype Actuator Specifications

To demonstrate FEA model validity, a prototype of a typical gas exchange actuator was donated by Daimler-Chrysler and tested to provide experimental results. A cutaway illustration of the actuator discussed in the proceeding work is shown in Figure 5.2. Both steady state and transient prototype response was simulated and experimentally measured. The prototype of the linear actuator discussed can be characterized as having a short stroke (small air gap) and flat pole and armature geometries. Such a configuration is typically, if not exclusively, cited among literature on automotive electromagnetic gas exchange valve actuators. These flat-face, short-stroke properties allow for a relatively fast response at larger air gaps in addition to strong holding force capability due to the high flux and hence force densities. Although a variety of pole and armature geometries and configurations are conceivable (such as conical, horseshoe, etc.), the flat-face offers large surface areas and minimal fringing for maximum force per actuator volume [Roters, 1941]. Unfortunately such a configuration has an inherently nonlinear force vs. position relationship which may compromise control performance. Other configurations such as a conical pole and armature interface produce a higher degree of fringing, resulting in a less dramatic change in air-gap over the entire stroke range and consequently providing a more linear force-position relationship at the sacrifice of volume or force density. Another key design characteristic of this actuator is the use of two preloaded linear compression springs. These springs offer an ideal way of achieving rapid flight times and minimizing electrical energy input. They do so by providing a high system energy

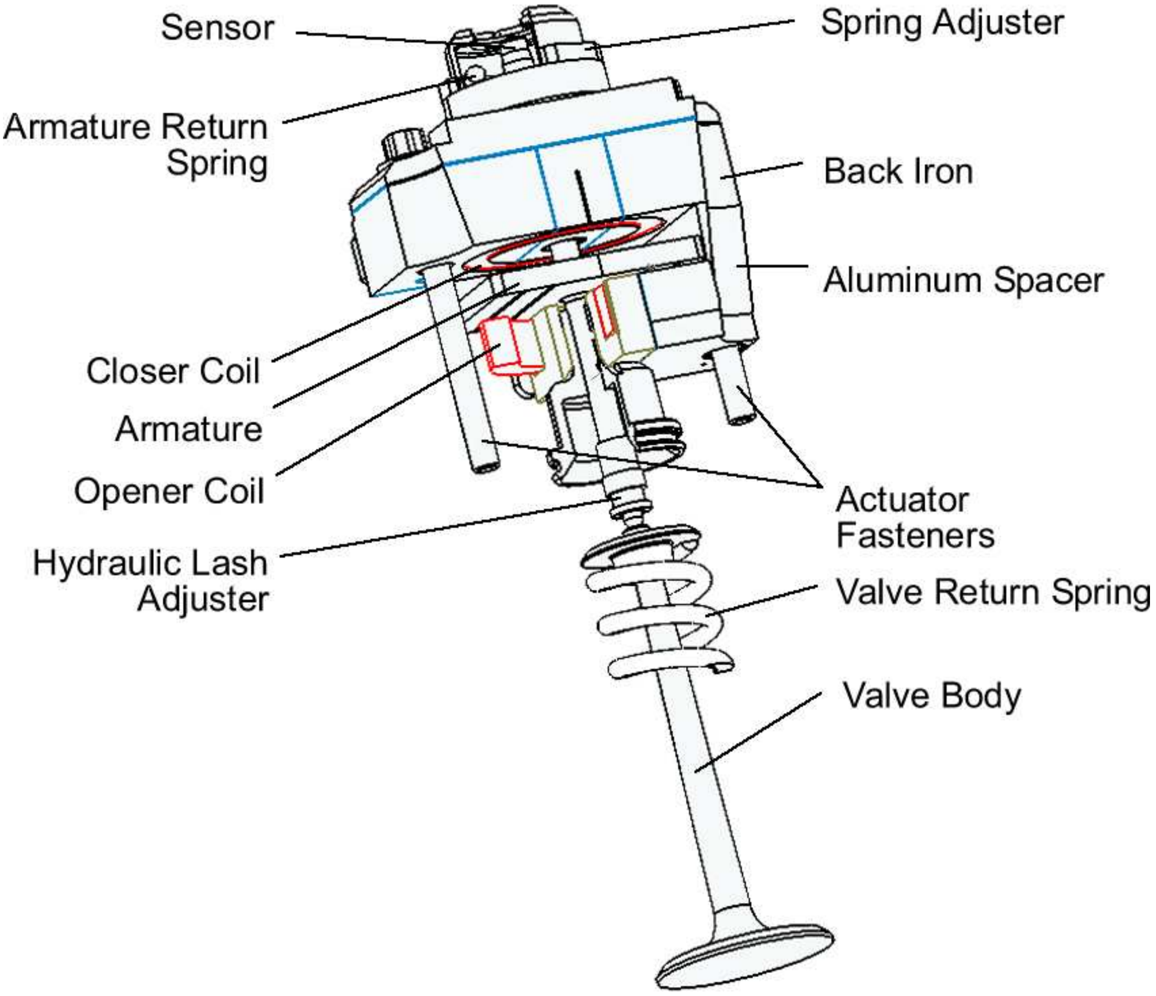

Figure 5.2: Cutaway View of the Actuator

density, which is required for overcoming significant combustion pressures, and by storing the kinetic energy during valve deceleration. Thus, the magnets are only required for 'catching' the armature at either stroke bound in addition to overcoming friction and pressure disturbances. However, the springs are also responsible for very rapid armature accelerations at the valve stroke bounds. These high acceleration rates impose significant sensor resolution demands in order to prevent excessive acoustic noise and premature wear caused by large armature and valve impacts. Spring stiffness is selected to be high enough to achieve the minimum valve flight time while overcoming valve gas forces. The moving mass and springs are also selected for a first mode system natural frequency of approximately 170Hz allowing engine speeds up to 5500RPM. The springs also introduce an additional parameter into the system which is subject to variations caused by thermal expansion and fatigue, potentially increasing control complexity. Opener and closer return spring force curves were measured and are plotted in Appendix Figure C.2. The actuator back iron material is made of QStE500 sintered powder steel and the armature is made from Vacoflux silicon steel, their respective properties are listed (where available) in Appendix C.2. Aluminium spacers are used to maintain a physically contiguous device while mitigating any tendency for flux to flow from one magnet to another without passing through the armature. For example, it is undesirable for flux generated from the opener magnet to pass through the opposing closer back iron, or vice versa. The closer coil has 79 turns and the opener coil has 72 turns. Due to peak current loads in excess of 40A, resistive and eddy current heating is expected. To assist in preventing thermal damage, the closer has cooling channels in the back-iron which allow for a coolant to circulate and transfer excess heat away from the actuator.

5.4 FEM of Actuator

The commercially available FEA software ANSYS 5.7 / 6.1 by ANSYS Inc. was used to simulate the performance of an electromagnetic actuator. ANSYS was used because it is widely available and commonly used among industrial and academic institutions alike. ANSYS also offers a batch operation mode, ideal for automating the solution of a large number of operating points. A two dimensional representation of half the opener and closer were separately modeled by assuming vertical symmetry as a means of minimizing model complexity and computational time. This assumption implies that the actuator has a cylindrical cross-section as opposed to an elliptical cross-section. Figure 5.3 illustrates the actual and modeled cross-sections (normal to the air gap flux path) that will most influence force estimates. Due to the minimal differences in area, and hence inductance / reluctance, only minor force discrepancies should be expected. The main weakness of the assumption between a 2D and 3D case will be the differences in fringing due to the neglected corners of the iron and armature as well as the more complex 3D eddy current paths available in the transient cases. However, the differences are minor in magnitude with respect to those effects captured by the 2D model and have not yet warranted the added complexity and computational load of a 3D model. It will be demonstrated in the following chapter that the validity of the 2D assumption is upheld by measured experimental results. As a means to conserve energy, both coils will never be simultaneously energized. This allows for the opener or closer to be modeled separately by assuming no interaction between the two iron paths. For example, all flux generated by the opener is assumed to only pass through the armature and return to the opener back-iron, not through the closer back-iron. Due to the relatively high permeability of the armature, it is assumed that any leakage flux will likely not interact in a significant way in an opposing back-iron. Due to the close similarity between the opener and closer, as well as practical measurement difficulties, only the opener was measured experimentally. Since the two magnets are quite similar in nature, it is presumed that a validation of one magnet will demonstrate the capability of accurately modeling the other.

5.4.1 Static Modeling and Simulation

In order to predict the actuator steady state performance static ANSYS models of the opener and closer were created using the proprietary ANSYS command language. The commands for each model are listed in two text files. One file, known as the master file, specifies the air gaps and excitations (in MMF) over which the force and flux are to be determined. The master file calls macros from a file containing scripts which automates the solution and data output of all the specified operating points.

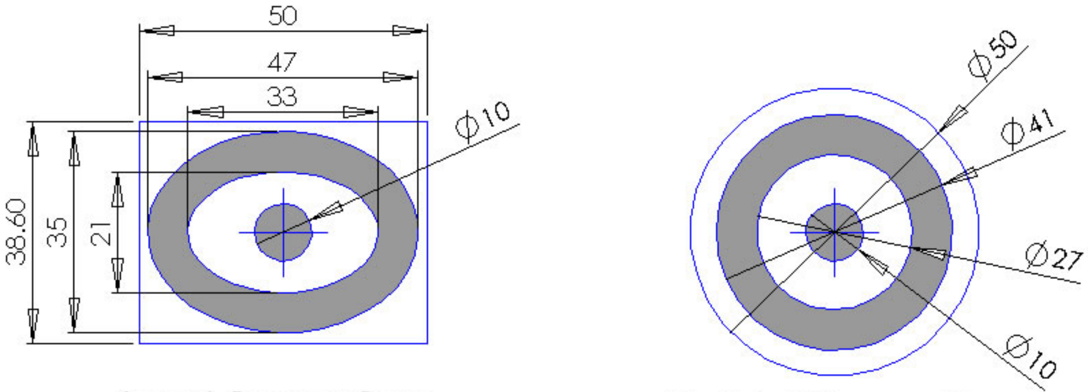

Actual Opener Core
Inner flux path area = 466mm^2
Outer flux path area = 638mm^2

Modeled Opener Core
Inner flux path area = 494mm^2
Outer flux path area = 643mm^2

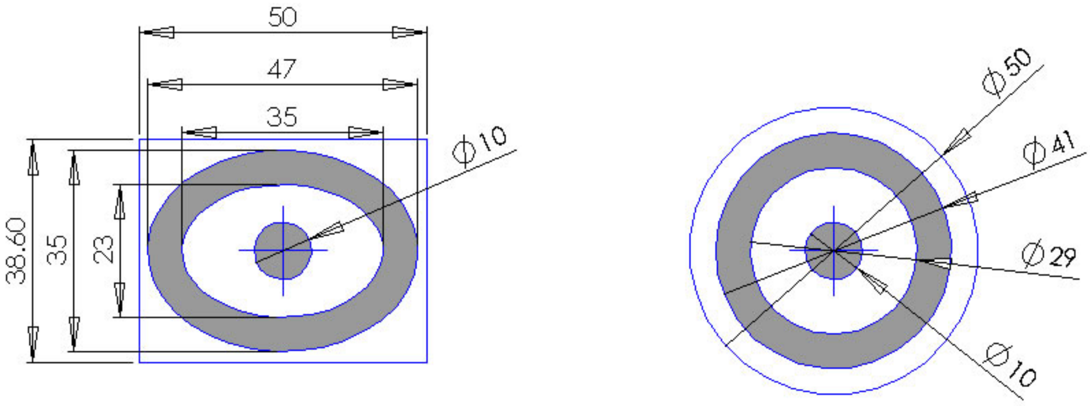

Actual Closer Core
Inner flux path area = 554mm^2
Outer flux path area = 638mm^2

Modeled Closer Core
Inner flux path area = 582mm^2
Outer flux path area = 643mm^2

Figure 5.3: Contrast of the actual actuator vs. modeled actuator flux path section areas

The macro file includes several functions which generate the appropriate geometry, mesh the model, specify material properties, apply boundary conditions and current excitation, clear old geometry and write force and flux data to the output file as specified by the master file. Flux and armature force values are calculated before a final macro is called which writes the flux and force data to a pre-specified text file. The resulting output data files are then processed and converted into appropriate MATLAB m-files for later use in a LPM. The master program continues to generate results for all excitation levels specified and then regenerates and meshes the geometry for the next specified position. The final result is a file containing force and flux values for each of the desired position and excitation levels. Results were determined for each of the operating points listed in Table 5.1 for a total of 336 static solutions.

Table 5.1: Air Gap and Excitation Operating Points

Air Gap [mm]							
0.03	0.08	0.15	0.20	0.30	0.40	0.50	0.60
0.80	1.00	1.50	2.00	3.00	4.00	6.00	8.00

Coil Excitations / MMF [Ampere-turns]						
50	100	150	200	250	300	400
500	600	800	1000	1500	2000	2500
3000	3500	4000	4500	5000	5500	6000

These operating points were selected through prediction and observation of the actuator response to provide a relatively smooth force and flux relation as a function of air gap and current. For example, it was known that a higher number of data points would be required for a smooth data set at low air gaps due to the dramatic change in force in such regions. Similarly, due to material saturation, a higher resolution of data was required at lower excitation levels rather than higher levels. The induction curves for both the back-iron and armature steel were provided with the prototype and input in the ANSYS model and plotted in Appendix C. Excitation levels were extended beyond normal or practically feasible levels to provide a means of investigating the possible benefits of using a unpractically large power source on control dynamics. Mesh refinement was determined by inspection as well as by ensuring force and flux convergence with respect to a decrease in element density. In order to prevent elements with poor aspect ratios, active mesh control was established in the back iron, armature and air gap regions in addition to the model boundaries. The default ANSYS auto-mesh generator was used to mesh the remaining regions

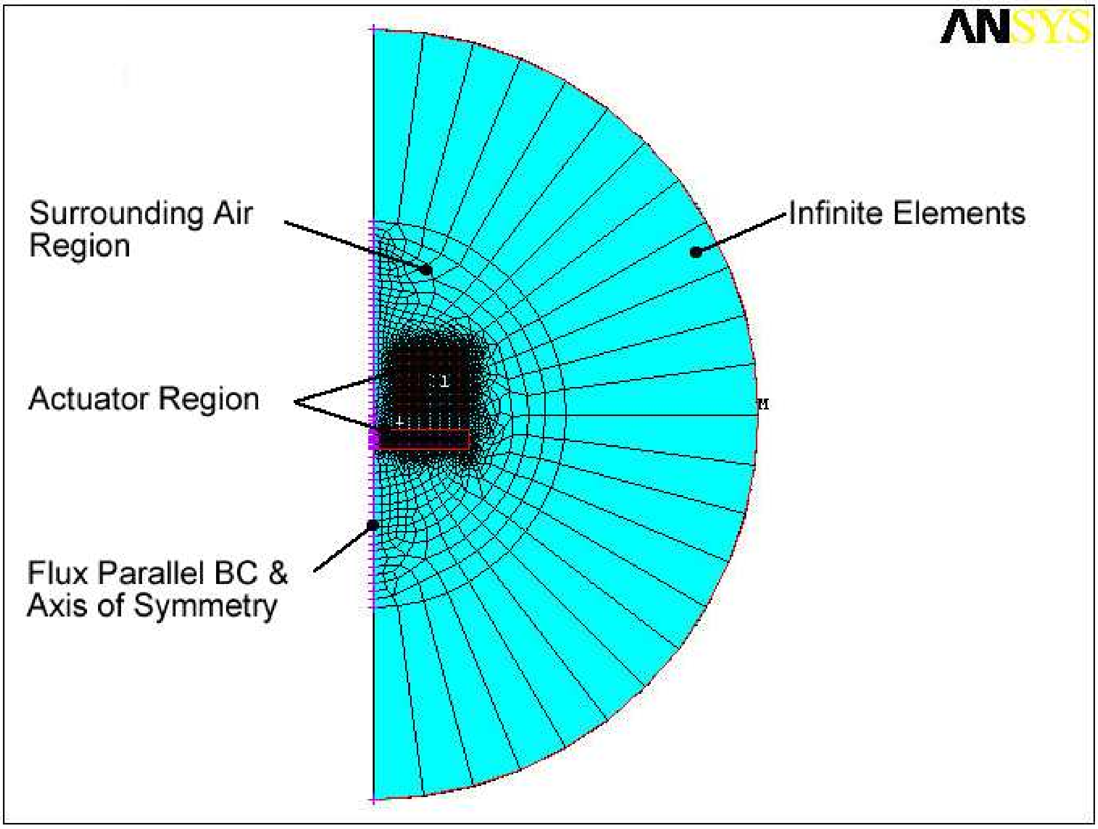

Figure 5.4: Static Model Elements and Mesh

with the smallest mesh refinement possible. In order to ensure appropriate element densities and shapes at extreme armature positions, a linear function was used to control the element mesh in the air gap region over the eight millimeter armature operating range. A single element of air is prescribed between the pole face and the armature at the smallest gap and sixteen elements for the largest gap. The model does not support a gap of exactly zero as a change in the number of areas will occur and the following material assignment and meshing routines will fail. However, this is not a model limitation, as even when the armature and back-iron are contacting, there is always a significant air-steel interface as no surfaces are perfectly smooth. Quadrilateral element type PLANE13 was used for the entire model domain (both iron and air regions) with the exception of a single layer of INFIN110 boundary ele-

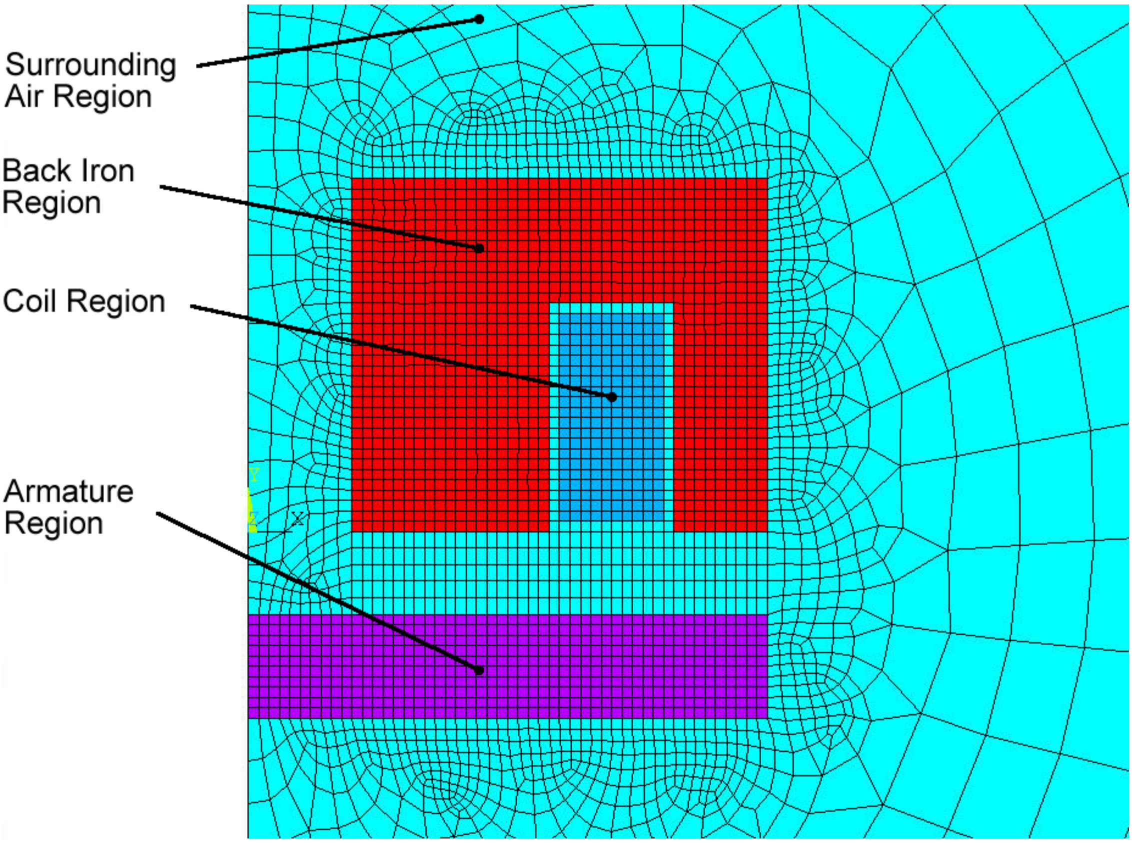

Figure 5.5: Close-up of Static & Transient Model Elements and Mesh

ments which are better suited to model far field decay. Figures 5.4 and 5.5 illustrate the PLANE13 element meshed over the armature, air and back iron portions of the model. INFIN110 elements surround the rest of the model in a semicircular fashion and were used to simulate far field decay. The infinite elements use shape functions to force the magnetic potential to zero at infinity. Coil excitation was applied directly to the coil elements in the form of current density, J $[A/m^2]$. Nodes located on the line of symmetry have a magnetic potential of zero imposed (also known as a flux parallel or Dirichlet boundary condition). A contrast between simulated and measured results is presented in Section 6.1.

5.4.2 Transient Modeling and Simulation

Although the focus of actuator modeling was to obtain static results for use in a LPM, some exploratory investigations were conducted to evaluate the ability of the ANSYS software to predict the results of equivalent transient experiments. Of particular interest was current and force response as a function of time and voltage for a constant air gap. To simulate coil and force dynamics, a quasi-static transient model was developed for fixed armature positions. Although the armature is fully constrained, the simulation should be more accurate than the LPM coil dynamic model as it accounts for eddy currents and the excitation history (low frequency only). A command file containing nearly identical macros as those used in the static cases were again used in the transient modeling. The transient model is not as automated as the static simulations since only nine operating points were investigated, thus a master file was not deemed necessary. Rather, macros that construct the geometry, mesh the model, apply boundary conditions and solve the resulting system for a pre-specified voltage input are manually called from the ANSYS graphical user interface (GUI) command line. The three positions evaluated are 0.30mm, 0.50mm and 2mm. At these positions, three voltage excitations, 24V, 42V and 50V were chosen to illustrate the effect of electric potential on actuator response time. A step voltage was applied for a specified time period to observe force and current rise and then switched off to observe the resulting force and current decay. Voltage excitation is specified by an array of times and corresponding step voltages. Due to complexities added by the power electronics and power supply, excitation was specified according to the observed voltage excitation. Results are determined at every time step which is implicitly defined by the number of steps taken from one solution time period to another. A higher number of steps are taken to ensure solution convergence and where a higher time resolution of results are required. Solution time varies with the number of time steps taken and the simulated duration. Typical transient solution time is approximately thirty minutes for a 0.020s simulation duration with approximately 125 time steps.

Quadrilateral element type PLANE53 are used for the entire model domain (both iron and air regions), again with the exception of a single layer of INFIN110 boundary elements. A voltage source, resistor and stranded coil are modeled using CIRC124 elements to excite the actuator FEA domain. The circuit elements are not part of the field solution. Rather, the stranded coil element current and EMF degrees of freedom (DOF) are coupled to the coil elements in the actuator domain. The resistor is only modeled in series with the stranded coil element for additional model flexibility and is usually set to zero as the coil resistance is accounted for through the geometry of the FEA modeled coil and the specified conductivity of copper.

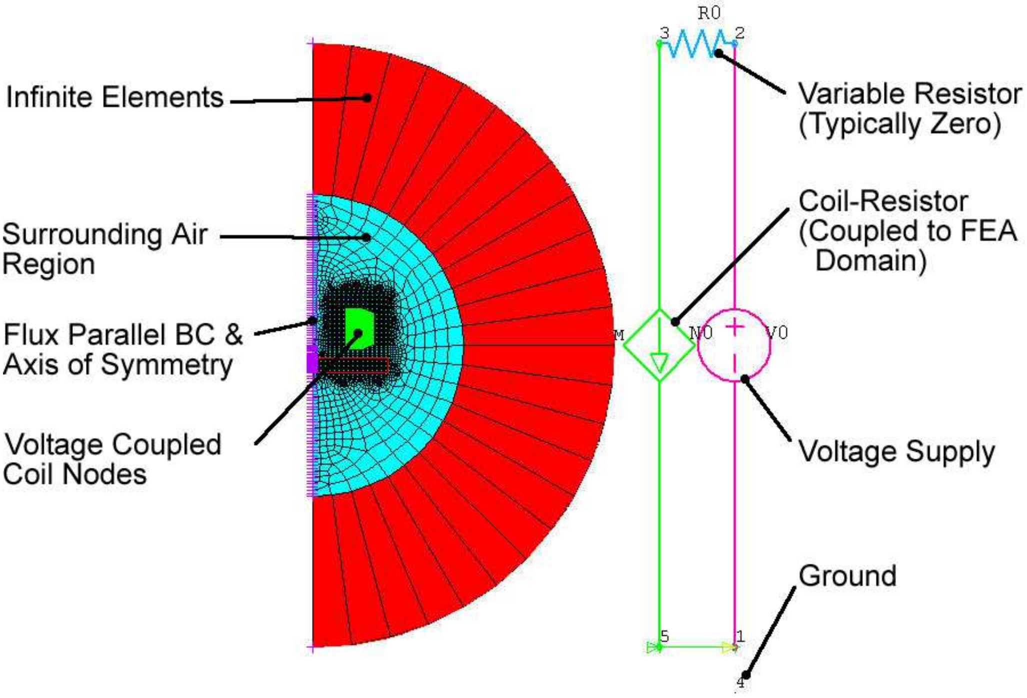

Figure 5.6: Transient Model Elements and Mesh

Figure 5.6 illustrates the transient model meshed with PLANE53, INFIN110 and CIRCU124 elements. Armature, back-iron and surrounding air regions are meshed identically to the static model as indicated in Figure 5.5.

Despite the FEA model not accounting for armature motion, the simulations may be useful for investigating armature release performance. For variable valve timing systems, armature release timing is critical for combustion and engine performance as well as low valve lift control development. During the release, the armature is at rest and the magnetic response may be investigated until the force is beyond that of the spring force, after which, armature motion is initiated. Similarly, the FEA transient studies may be used for developing the low valve lift operation mode where again, the armature is not fully released. This mode is characterized by rapidly varying the magnetic field on the closer side which in turn allows the valve to only open a short distance rather than the full eight millimeters. The operation may be ideal at low engine speed and load conditions such as idling, although may require high electrical energy. The results were compared with those observed in the experiment described in Section 4.6 and discussed in Section 6.2.2.3.

5.5 Linear Theory Actuator Model

A model utilizing linear theory was derived to contrast the static ANSYS and experimental results. For this system, force was calculated by first determining an expression for inductance as a function of air gap. Inductance relates the resulting change in a magnetic flux for a given change in current as discussed in Section 3.5. Figure 5.7 illustrates the mean flux path established through the back iron, armature and air gaps. Each region is represented by at least one length, material permeability and cross-sectional area. The actuator is discretized into four area sections, namely, the two air gaps, one section that vertically bisects the back iron above the coil region, A_2 and one that vertically bisects the armature below the coil, A_4. Just as in the FEA model, the linear model also assumes an axisymmetric actuator. Since the actuator is

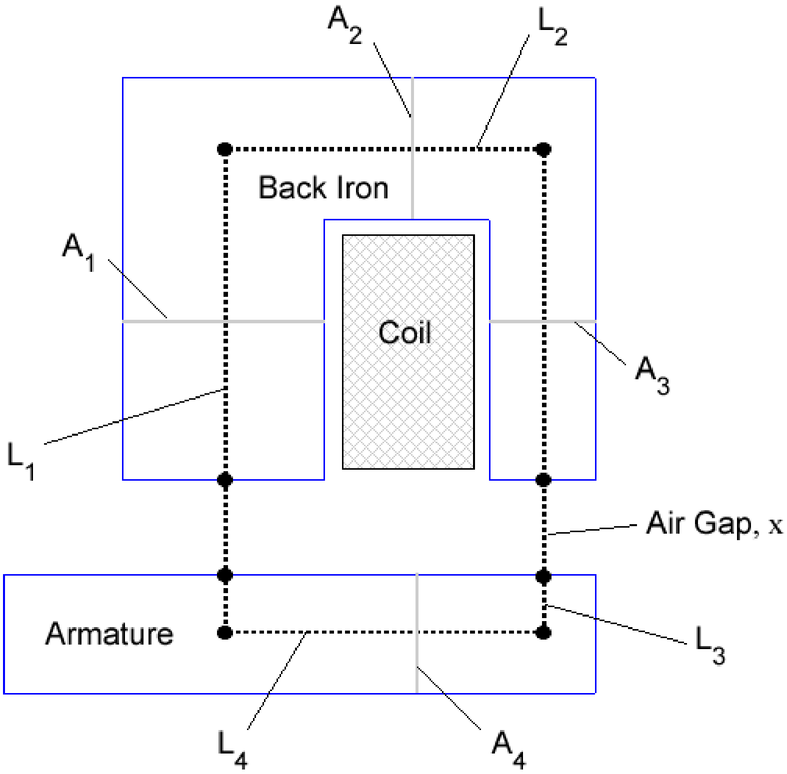

Figure 5.7: Lengths and Areas used for the Linear Inductance Calculation

assumed axisymmetric, the reluctance need only be calculated for one side, but using the areas for the entire device. For example, the two air gap areas, A_1 and A_2, are the same as those modeled in Figure 5.3. Using these parameters, the reluctance for the entire opener may be expressed as

$$\Re = \alpha + \beta + x\gamma \tag{5.4}$$

where,

$$\begin{aligned}
\alpha &= \frac{1}{\mu_{iron}}\left(\frac{L_1}{A_1} + \frac{L_2}{A_2} + \frac{L_1}{A_3}\right) \\
\beta &= \frac{1}{\mu_{arm}}\left(\frac{L_4}{A_4} + L_3(\frac{1}{A_1} + \frac{1}{A_3})\right) \\
\gamma &= \frac{1}{\mu_0}\left(\frac{1}{A_1} + \frac{1}{A_3}\right)
\end{aligned}$$

The linear permeabilities for the back iron, μ_{iron} and armature, μ_{arm}, are estimated from the induction curves for the respective materials as plotted in Figure C.1. Since the linear permeability of steel is approximately 1000x greater than air, it is not expected the steel material properties will become significant in the inductance calculation at large air gaps or prior to the onset of saturation. Upon material saturation, the steel permeability is the same as free space, μ_0 or air, and hence the reluctance of the steel flux path lengths, L_1 through L_4, are as significant as the air gaps. Saturation is expected to occur at relatively large excitation levels and small air gaps, as it is at those operating points where the magnetic field intensity will be greatest. The derived reluctance may be related to inductance by

$$L = \frac{N^2}{\Re} = \frac{N^2}{\alpha + \beta + x\gamma} \tag{5.5}$$

where N is the number of coil wraps. For steady currents, an expression for force may be derived by using the derivative of inductance with respect to airgap, x and Equation 3.70 as shown below.

$$F_{avg} = -\frac{1}{2} i^2 \frac{\partial L}{\partial x} = \frac{N^2 i^2 \gamma}{2\left[\alpha + \beta + x\gamma\right]^2} \tag{5.6}$$

Note that this expression only approximates the average force, and does not account for the field and hence force distribution across the armature. It should also be stated that a model using linear theory may also be developed by curve fitting an equation approximating a force-position relation with experimental prototype or FEA data. It was found that the use of FEA data look-up tables was more accurate than an expression fit to FEA results. Further, the use of prototype data to develop control models undermines the intent of alleviating the necessity of prototype construction. More detail on this method is provided in Section 2.5.

5.6 Lumped parameter model of actuator and valve system

A lumped parameter model was constructed in Simulink as a means of evaluating the overall actuator and valve performance. By determining only terminal parameters such as force, velocity, displacement and current with respect to time, a complex field analysis may be avoided. When compared to a full motion FEA, the lumped parameter model is substantially less computationally expensive and is easier to manipulate over a variety of initial and boundary conditions. By using the data from the static FEA analyses, the nonlinear effects due to magnetic saturation may be more accurately represented with simple linear lumped parameter models and lookup tables. Physical parameters such as valve mass and spring stiffness were measured for use in the LPM. Valve mass was measured with a digital scale and spring stiffness was measured using the the MTS load cell apparatus. The model does not presently account for gas forces or effects of friction and eddy current losses, although they may be incorporated. The model also neglects valve lash effects. Again, this may be accounted for by assuming the armature / valve system has two independent mechanical degrees of freedom and spring elements rather than one. Dynamic valve and armature impacts are also neglected. The model presently forces the velocity to zero at either pole face. Elastic impacts could conceivably be included with knowledge of the material coefficient of restitution for a perhaps more realistic prediction of armature and valve impact behavior. The main objective of the LPM used in this work is to demonstrate the extension of a typically linear modeling technique by incorporating nonlinear field solutions in lookup tables. The FEA data is expected to improve the LPM accuracy sufficiently enough to allow the development of realistic control designs. Although much of the experimental hardware necessary to conduct valve system testing has been acquired as described in Section 4.7, the model has yet to be combined with a control strategy or contrasted with equivalent test-bench results.

5.7 Experimental Validation

In order to validate the FEM simulations, experiments using a prototype actuator were devised. Only the opener portion was tested as there was no available means of securely and non-invasively measuring the tensile force generated by the closer. As the opener and closer only differ in the number of coil turns and slightly in geometry, it was deemed only necessary to validate the opener FEA simulations.

5.7.1 Static Experiments

For both the static and transient experiments, the actuator was fixed in the MTS apparatus using custom machined adaptors. Just as in the FEA simulations, a predetermined position was set with the MTS position controller and the opener coil was energized at a variety of current levels. To maintain a specific current excitation the dSpace controller uses a current control algorithm which rapidly switches the coil voltage with a PWM signal, holding the current within a specified tolerance. This procedure allowed for a repeatable method of applying relatively steady current excitation. If a constant coil voltage were applied, the coil current would continue to rise until either saturating the power supply or satisfying $V = IR_{Coil}$. In all likelihood, the power supply would saturate and the coil would overheat and be destroyed. For both static and transient experiments, the force and current response was measured with the load cell and power electronics Hall effect sensor respectively. All signals were recorded with the dSpace control card in both experiments.

5.7.2 Transient Experiments

The transient experiments were conducted to validate the transient FEA models. A step voltage pulse of predetermined duration was used to excite the actuator while measuring force and current response. Voltage steps of 24V, 42V and 50V were applied at three different air gaps. These experiments served little beyond lending insight of the ability of the FEA and LPM models to predict transient behavior.

5.7.3 Future Test Bench Experiments

For future control testing and refinement an experimental apparatus was constructed to simulate typical response within an engine as shown in Figure 4.10. The actuator horizontally apposes an exhaust valve and return spring. A sealed cylinder mounted over the valve seat allows the ability to simulate exhaust gas forces with pressurized air. Internal pressure and hence gas forces may be determined with a pressure transducer. A Micro-Epsilon eddy current sensor provides valve displacement. Otherwise, the power supply and electronics hardware setup is nearly identical to the MTS validation experiments. However, control software is required for full motion actuator experiments is beyond the scope of this study.

5.7.4 Displacement Sensor Requirements

Due to the low-impact speed requirement of the valve and significant combustion pressure fluctuations, a means of accurately sensing armature or valve position is required for feedback control. The feedback sensor imposes a requirement on the control system. Figure 5.8 illustrates a typical valve trajectory as it is released from one pole face and forced to the other by the actuator springs. It is desirable to correct for landing speed as close to the pole face as possible to minimize flight time and electric energy input. For an ideal mass spring system without disturbances or damping, this phase plane plot would be circular rather than elliptical. Assuming that the control system follows the steep deceleration of the spring mass system and that the valve impacts at V = V_{impact}, the effect of a displacement offset may be calculated with a first order approximation. For example, the linearized slope prior to impact may be, $\frac{\Delta V}{\Delta s} = \frac{0.5m/s}{0.1mm}$ corresponding to a deceleration of 0.5m/s over a

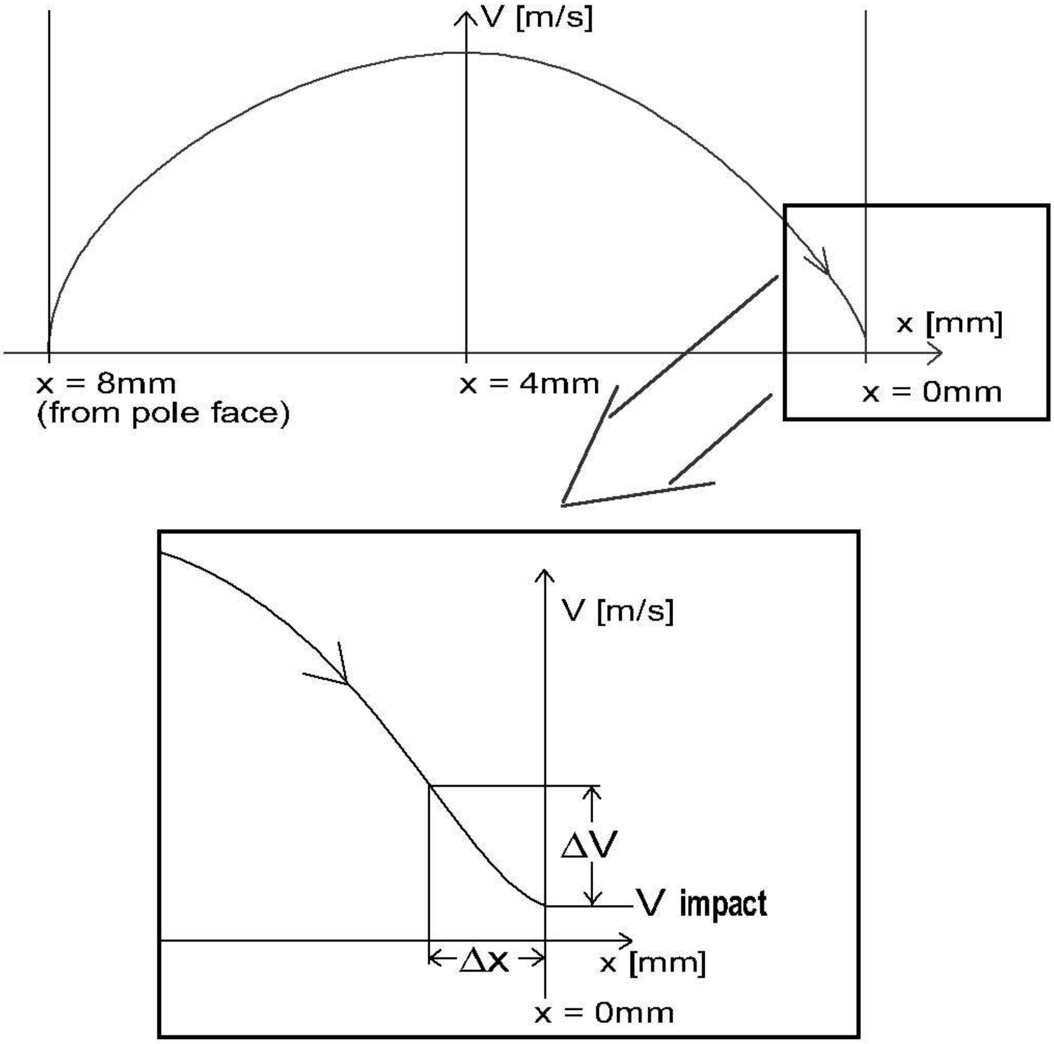

Figure 5.8: Position uncertainty with respect to air gap

0.1mm stroke. Since a typical impact velocity requirement is $0.1m/s \pm 0.05m/s$, the corresponding variation in position, Δx, is equal to at least $0.05m/s(\frac{0.1mm}{0.5m/s}) = 0.01mm$ or 10μm. Thus, a sensor accuracy of at least $10\mu m$ is required. A sensor with this accuracy over a 8mm stroke length is currently expensive and requires online end position calibration. In addition, the sensor response must not limit the control system and consequently system stability. Therefore, the sensor must have an equivalent response or bandwidth of the actuator system. This bandwidth can be met with LVDT, eddy current or laser sensors. However, these sensors tend to be expensive or inappropriate for operation in an engine environment. Other promising sensor concepts have been proposed such as self inductive [Takashi and Iwao, 1995] and coil type [Roschke and Bielau, 1995], [Rossi and Tonielli, 2001]. It is proposed that the driving coil itself be used to measure coil flux and current to relate the armature position. Such a sensor would obviously be cost effective, although it may be complicated by signal processing related challenges [Butzmann et al., 2000].

5.8 Alternate Actuator Configurations

Upon establishment of a design concept and a method for investigating the design accurately, it may be necessary to derive and simulate more stable designs. One example of a proposed alternate design concept is the hinged armature or 'clapper' style solenoid as illustrated in Figures 5.9 and 5.10. In this configuration, an armature rotates about one pinned end instead of translating axially. Rather than using two linear compression springs, the armature equilibrium is balanced between a torsion bar and one linear compression spring. Pole geometry is considered 'U' shaped and can be easily made of laminated steel for eddy current suppression. By taking advantage of a mechanical leverage ratio, a flatter force vs. position relationship may be developed as shown in Figure 5.11. Here a leverage ratio is defined as the distance from the hinge point to where the net magnetic force acts on the armature, divided by the horizontal distance from a hinge point to where the force is transmitted to the valve body. For example, a ratio of 1 can be considered as equivalent to a linear case and a ratio of 0.5 indicates a situation where the point of valve contact is twice as far from the hinge point as the net magnetic force on the armature. A flatter force displacement relationship is also expected due to the less dramatic change in air gap over a full valve stroke. A flatter force response enhances stability and consequently reduces system bandwidth and actuator tolerance requirements.

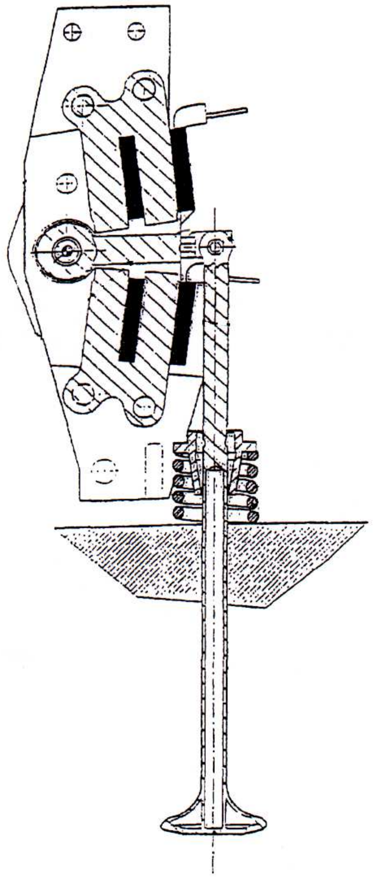

Figure 5.9: Hinged Actuator Concept from [Rossi and Tonielli, 2001]

5.9 Summary

A brief summary of electromagnetic VVT actuator constraints, design process and development challenges was given. A typical prototype is used to discuss fundamental design requirements and experimentally measured to validate a proposed modeling process. The process proposes an accurate FEA field analysis be coupled with a simplified LPM to provide a practical and sufficiently accurate model of the entire actuator system for control system development. Feedback sensor requirements and an alternate actuator concept were also presented to provide examples of other areas of actuator development.

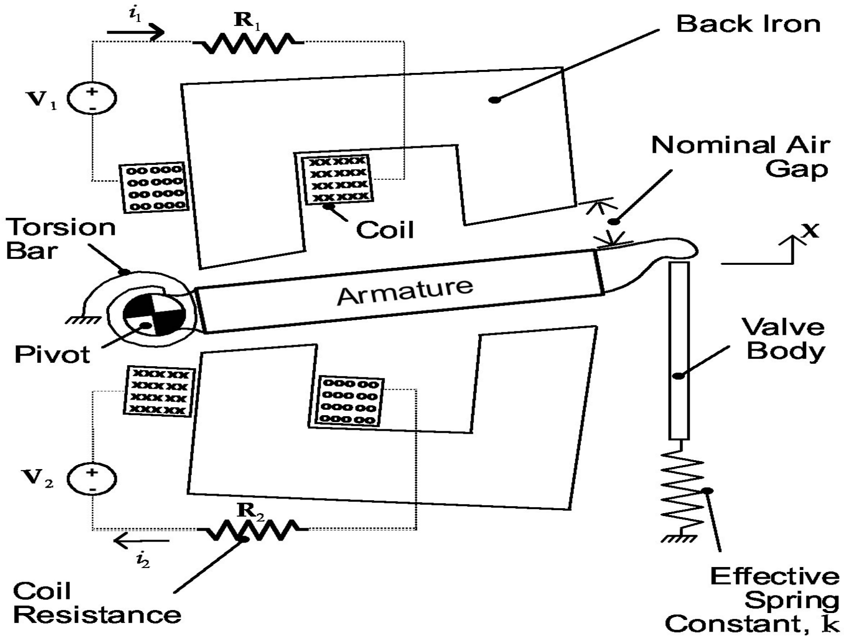

Figure 5.10: Hinged Actuator Schematic

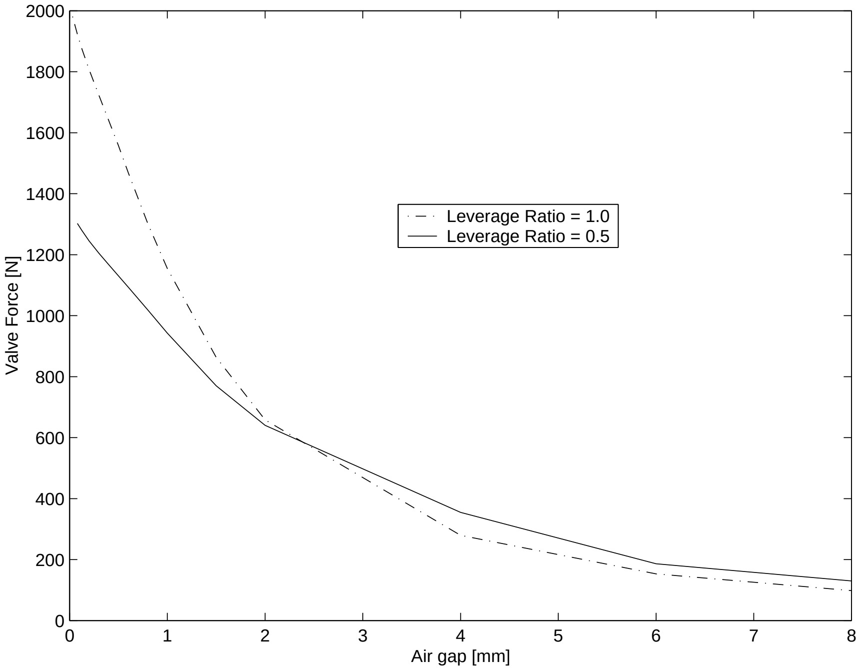

Figure 5.11: Effect of Leverage Ratio on Force-Position Relationship

Chapter 6

Discussion and Results

6.0.1 Introduction

The following summarizes and discusses the results obtained during the simulation and experimental investigation of an electromagnetic prototype actuator. Of primary interest are static predictions of armature force at specified air gaps and excitations as these results will be used in subsequent LPM simulations.

6.1 Static Results

The opener static force results for various excitations are plotted in Figures 6.1 and 6.2. The prototype actuator force was measured using the MTS and current control apparatus as described in Section 4.6. The measured results are contrasted with the ANSYS simulation results as well as those predicted by linear magnetic theory. ANSYS and linear model force predictions were simulated as discussed in the previous chapter. The nonlinear force response is indicative of the flat pole face / armature actuator type. Experimental results beyond 4mm are not included due to the relatively small change in force over the remaining stroke length. Due to power supply limitations in addition to minimizing the risk of excessively loading the opener coil, excitation levels were limited to 40A. Realistic coil currents at air gaps less than

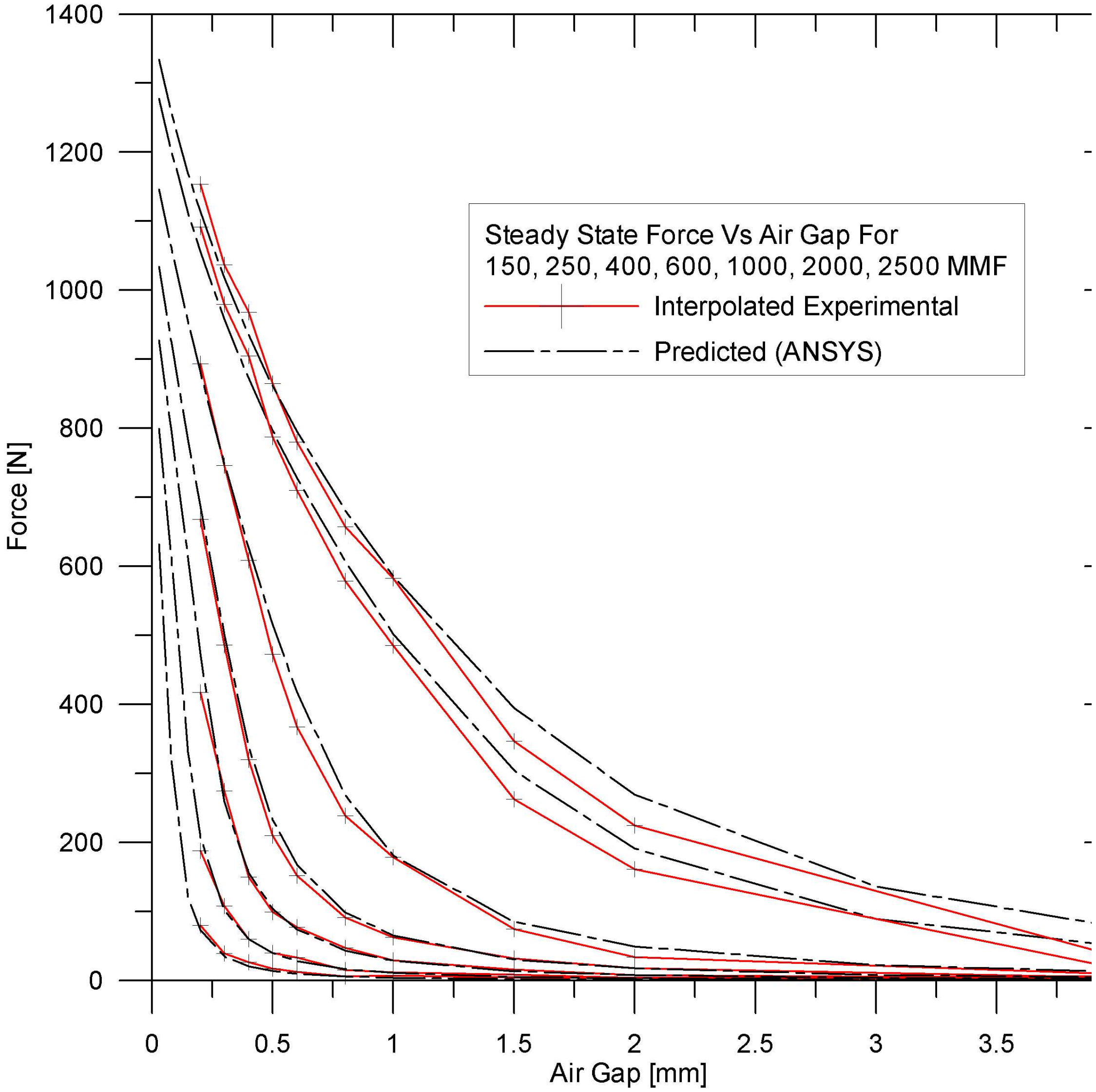

Figure 6.1: Experimental and ANSYS Force Vs. Air Gap for Various Excitations

0.20mm resulted in force loads capable of deflecting the armature sufficiently enough to partially contact the pole face, making any recorded force measurement erroneous. These measurements are not included.

ANSYS uses the Maxwell Stress Tensor force calculation method for force prediction. Generally, the ANSYS and experimental results have good agreement at all operating points. Although the specified experimental excitation levels were repeatable within 0.5A, they were often similar but not identical to those levels simulated. Rather than

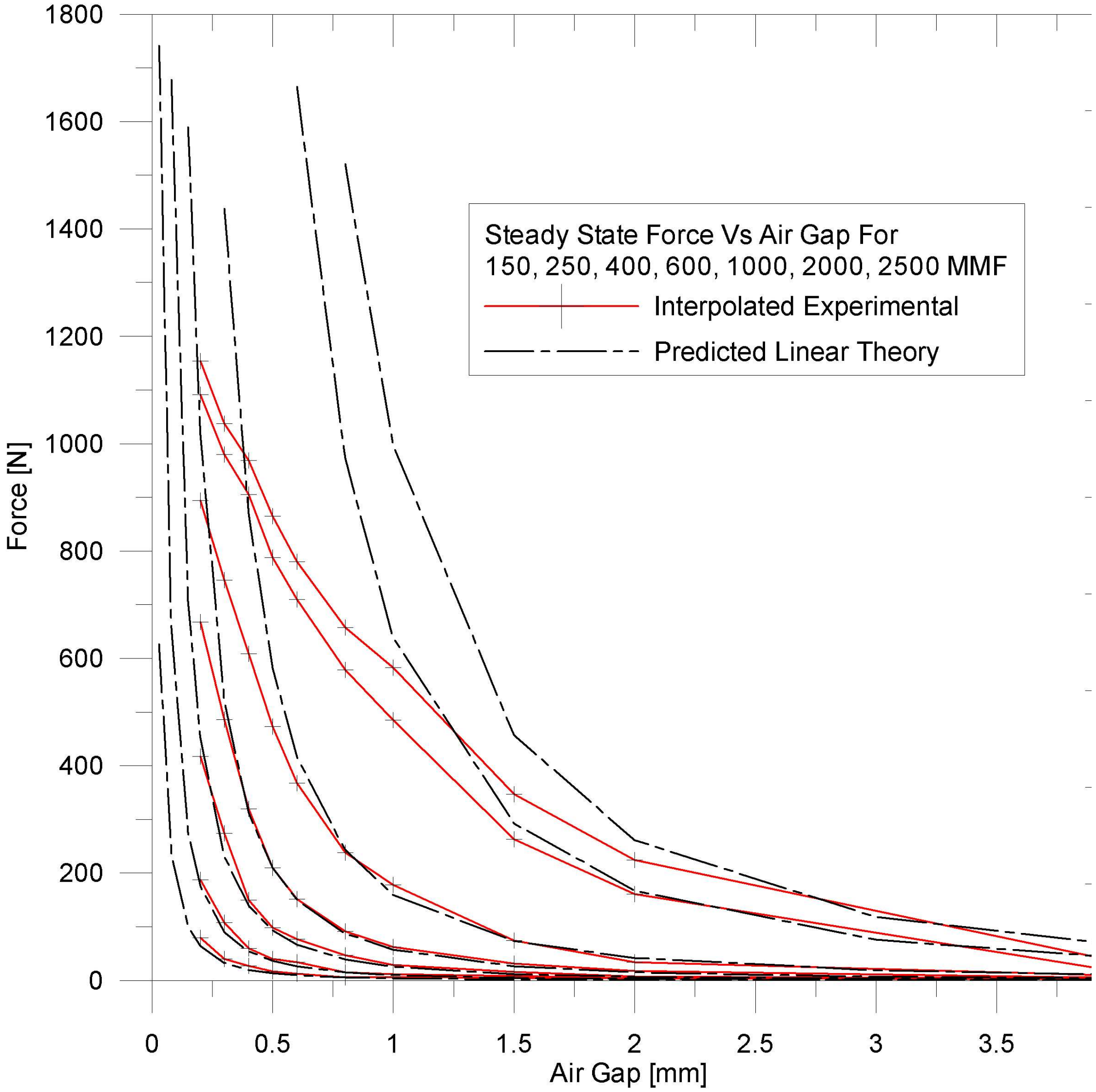

Figure 6.2: Experimental and Linear Model Force Vs. Air Gap for Various Excitations

re-simulate at the experimental operating points, the experimental results were linearly interpolated to the exact simulated operating points. The interpolation error is not expected to be significant with respect to experimental measurement error or actuator manufacturing tolerances. For example, it was observed that the air gap consistently varied by as much as 0.08mm from one armature edge to another. The air gap was measured at the smallest side resulting in a mean air gap that was actually larger than the one simulated. This may explain the general trend of the ANSYS

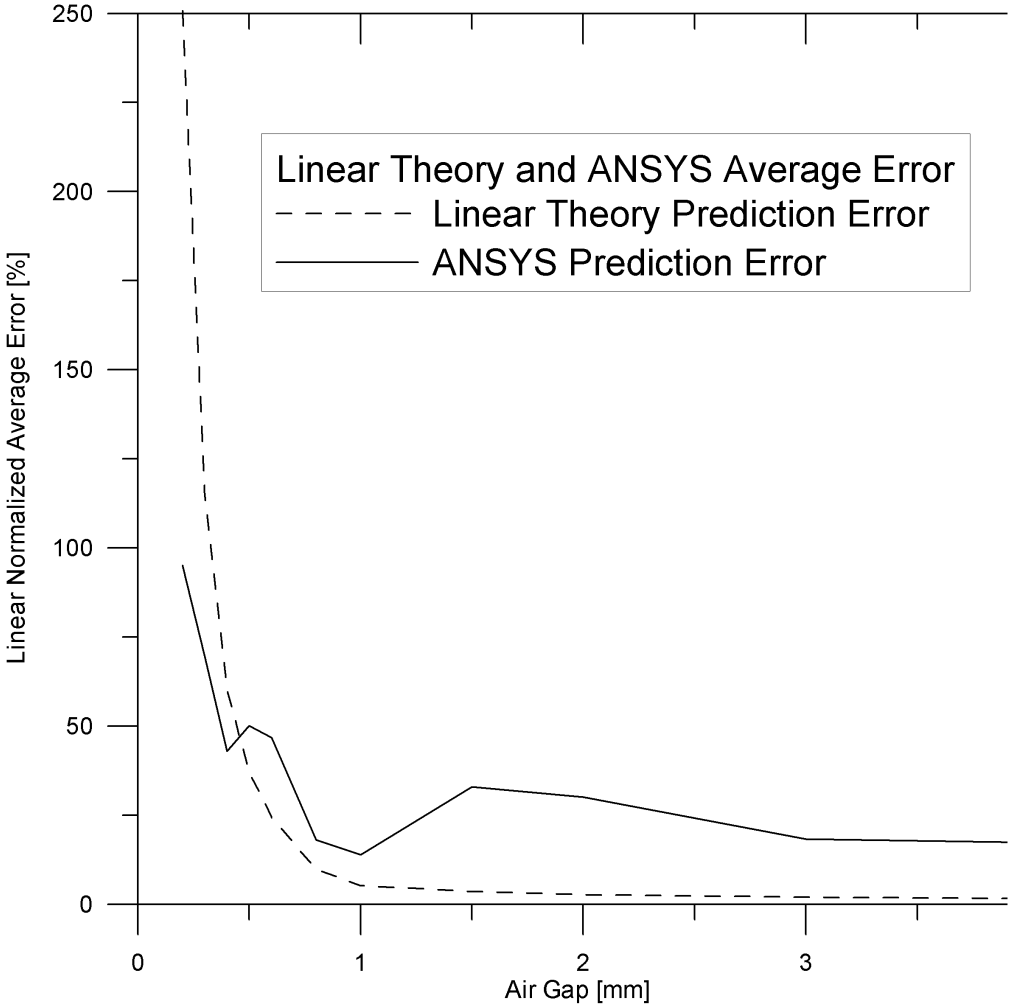

Figure 6.3: Normalized Average Linear and ANSYS Force Error

model to slightly over estimate the measured steady state force. The axisymmetric modeling assumption may also be responsible for some of the discrepancies. The normalized ANSYS and linear force error are plotted Figure 6.3. The ANSYS error is averaged over all excitation levels at constant air gaps and the error is normalized by the maximum force obtained for each excitation level. ANSYS force prediction error does not exceed 10% and is typically no more than 5%. This is an excellent result considering the complexity of the system. The magnitude of these errors are of the same order of the variations expected between actuators and thus must be accounted for in the controller design anyway. In contrast, Figures 6.2 and 6.3 indicate that the linear theory model exhibits very poor performance for air gaps less than 0.5mm with errors in excess of 200%. The average error in such regions is dominated by the higher excitation level operating points. For control of the armature landing speed, force errors in excess 200% will significantly affect controller design. Consequently, the use of this linear model is not recommended for control simulations. For an objective comparison, parameters of the linear model are determined using only geometric data and material permeability which may be obtained from a preliminary design study. Consequently, the ANSYS model and linear model used have similar information. Thus, a prototype does need not need to be constructed to establish either model. It is possible to improve the linear theory model by fitting a representative relationship to obtained experimental or ANSYS data. The modified linear model can then be used as an aid in designing some types of controllers [Koch et al., 2002].

The large observed linear model errors are due (at least in part) to the poor estimate of inductance, which is dependant on the material properties. The relationship for inductance as a function of air gap was determined as described in Section 5.5 and is used to estimate the average armature force as described in Section 3.5.1. The calculated linear model inductance and ANSYS predicted inductance (for various excitations) are plotted as a function of air gap in Figure 6.4. The ANSYS inductance is determined at a constant excitation level with the definition of inductance, $L = \frac{\lambda}{i}$. At the lower excitation level of 150MMF (equivalent to a coil current of approximately 2A for the opener) and air gaps less than 0.5mm, the linear inductance prediction is reasonably accurate. Note for this same excitation level that the linear model deviates from the ANSYS prediction with increasing air gap. This deviation may be explained by the linear model's inability to predict flux leakage. One of the the linear model assumptions is that all flux must be constrained strictly to the back iron, armature and air gap areas, irrespective of air gap. Practically, this should not be expected,

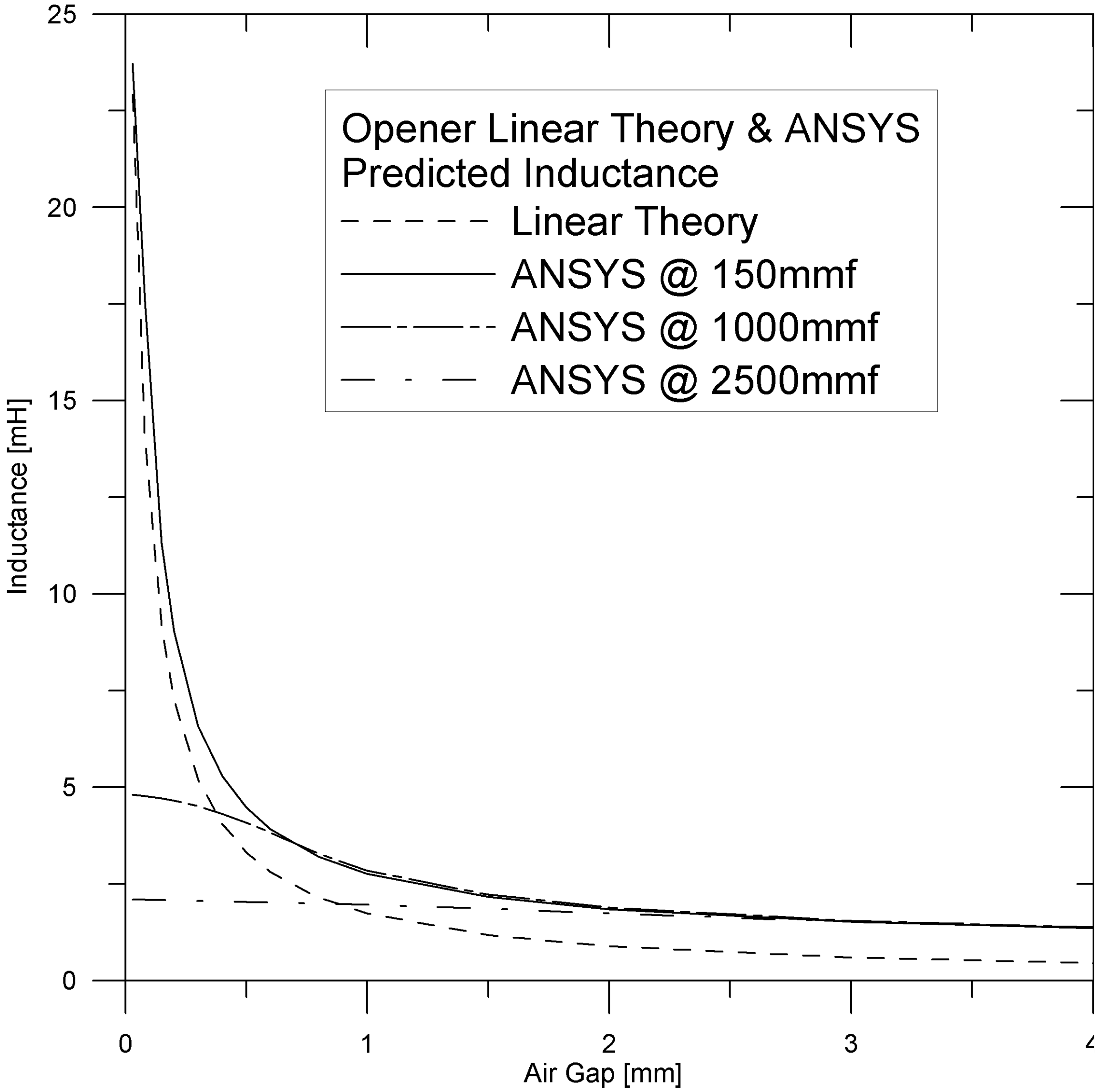

Figure 6.4: Predicted Linear and ANSYS Inductance at Several Excitations

as at large air gaps some flux will bypass the armature and instead pass from one portion of the back iron, through the air immediately surrounding the pole face and return to the back iron. This leakage effect may be observed in the static flux contour plot shown in Figure 6.7. Flux leakage results in a net decrease in reluctance (the air path is not as large) and hence a higher inductance should be expected.

At larger excitation levels and small air gaps, the linear material permeability assumption becomes invalid and the resulting inductance prediction becomes increasingly inaccurate. Note that for the excitation level of 2500MMF (∼35A), ANSYS predicts little change in inductance. This can be attributed to significant flux fringing and the early saturation of the back iron and armature. Consequently the change in armature position has a less dramatic affect on the system reluctance.

After an expression for inductance is obtained, the derivative is taken with respect to the change in air gap for a constant excitation level. The result is used in Equation 3.70, the linear magnetic force expression. Just as in the case of the linear model inductance prediction, the force relationship is generally good at predicting forces at relatively large air gaps and low excitation levels. The influence of material saturation on the linear model inductance and ultimately force prediction accuracy is apparent at higher excitation levels and air gaps less than 0.5mm.

6.1.1 ANSYS Static Results

After the ANSYS force and flux results are generated, they are processed in Matlab for further use in Simulink LPM lookup tables. The results are plotted for the opener in Figures 6.5 and 6.6. Similar results were obtained for the closer. The plots clearly demonstrate the influence of nonlinear permeability and the onset of saturation. Note the nearly linear force and flux response with respect to excitation at large air gaps. Also note that force magnitude is most significant for only a small portion of the total stroke length (where the air gap is smallest). This would suggest that simultaneously using both coils to influence the armature trajectory to reduce landing speeds would be ineffective and energy inefficient. In all of the static ANSYS simulations, flux was calculated at a vertical section bisecting the vertical portion of the back iron directly above the coil region. Simulated flux was calculated in the back iron rather than the armature because it is the most practical location to measure magnetic flux experimentally. It may be desired to measure flux for further model validation or

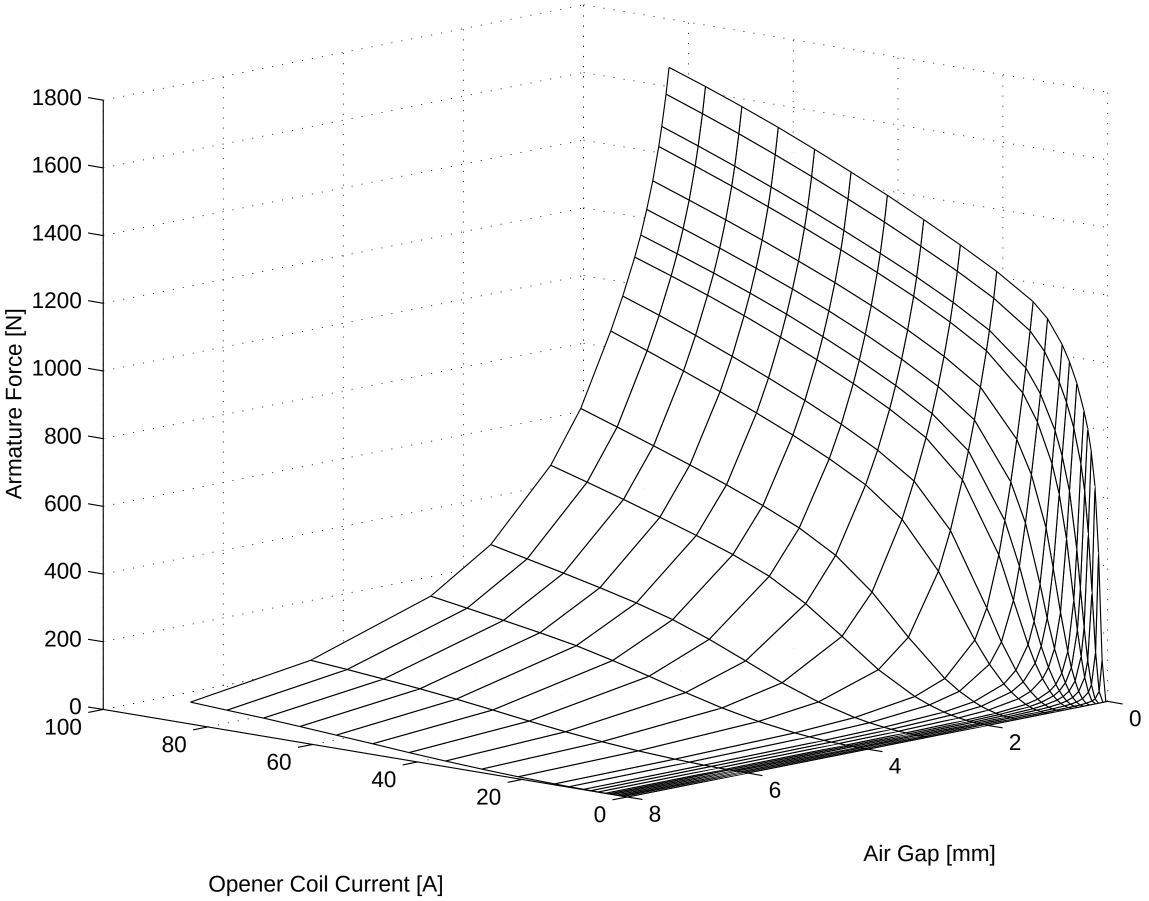

Figure 6.5: Opener Force Vs. Air Gap and Excitation

position sensor development. Flux was also calculated through the armature and exhibited a similar response shape as armature force.

6.1.1.1 ANSYS Static Flux Contour Plots

As a means of assessing flux leakage and fringing, ANSYS was used to produce flux contour line plots of the closer at extreme operating positions as shown in Figures 6.7 and 6.8.

The plots may also serve as a qualitative assessment of flux density distribution, as regions with a large number of flux lines indicate a higher flux density level. Each continuous line represents a constant level of magnetic flux, the value of which is

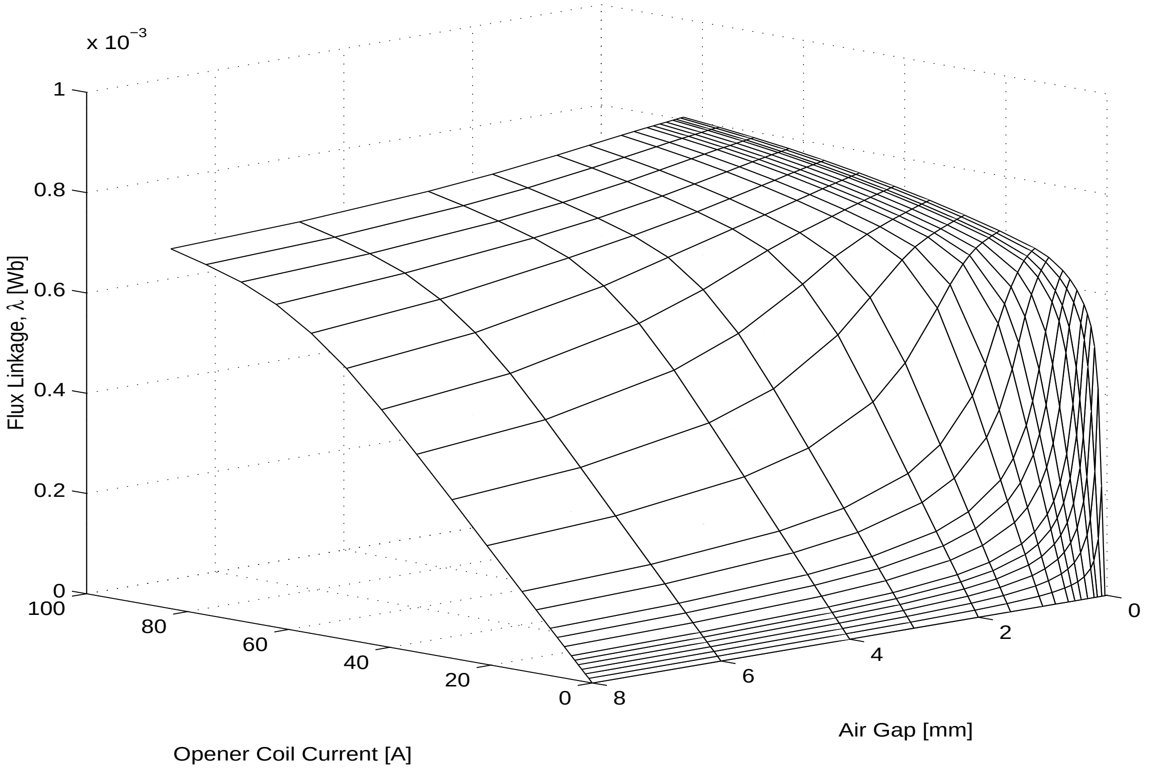

Figure 6.6: Flux Vs. Air Gap and Excitation

indicated in the legend on the right hand side of the figures in units of Webers. For the case of the opener and closer, the largest flux values refer to the innermost contour, and the lowest values to the outermost contour. At 8mm, significant fringing between the the back iron and armature is observed. As well, the majority of the flux does not pass through the armature at all. Rather, the flux flows through the air gap from one leg of the back iron to the other, consequently resulting in a relatively small armature force. Conversely, for the case of 0.03mm, there is little to no observed leakage or fringing as the armature is close enough to the pole face to constrain nearly all flux flow.

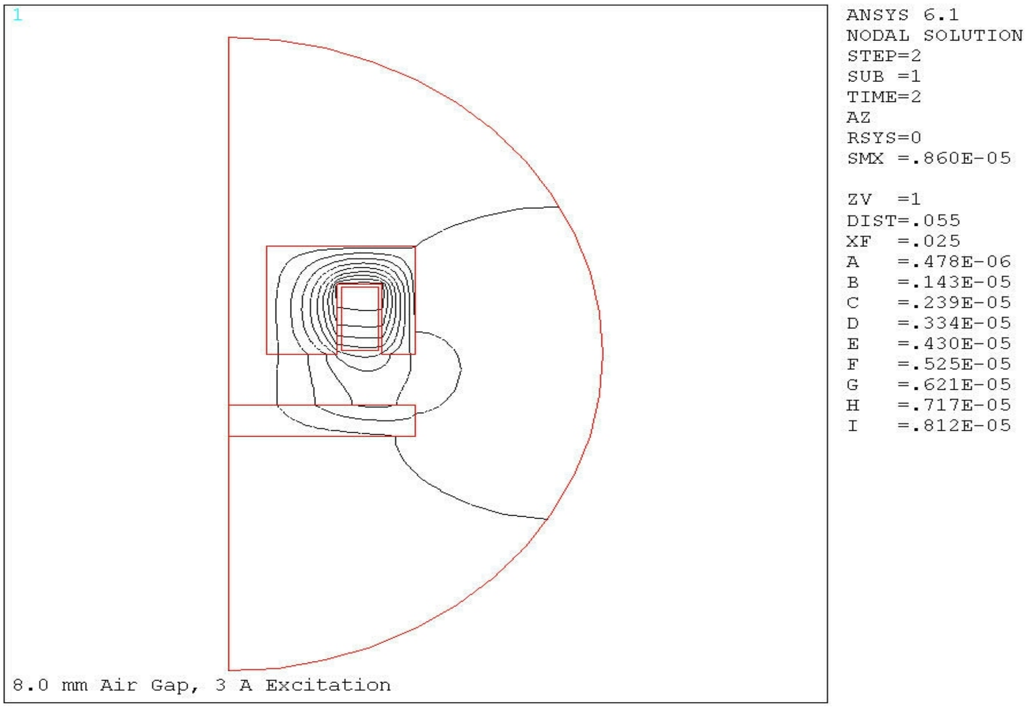

Figure 6.7: Flux Lines at 8.0mm Air Gap, 3A Excitation

6.2 Transient Current & Force Response

As a means of investigating the ability of predicting transient force response, several experiments were conducted where a predetermined time varying voltage was applied and the change in coil current and force was measured. Equivalent linear, ANSYS and lumped parameter models were used to simulate the current and force response from the same voltage input. The measured and simulated responses are contrasted in Figures 6.9 through 6.17 for 1.5ms 24V, 42V and 50V pulses at fixed air gaps of 0.5mm.

6.2.1 Voltage Input

Simulation voltage is input using points that approximate the measured voltage response in a piecewise linear fashion. ANSYS interpolates this function according to

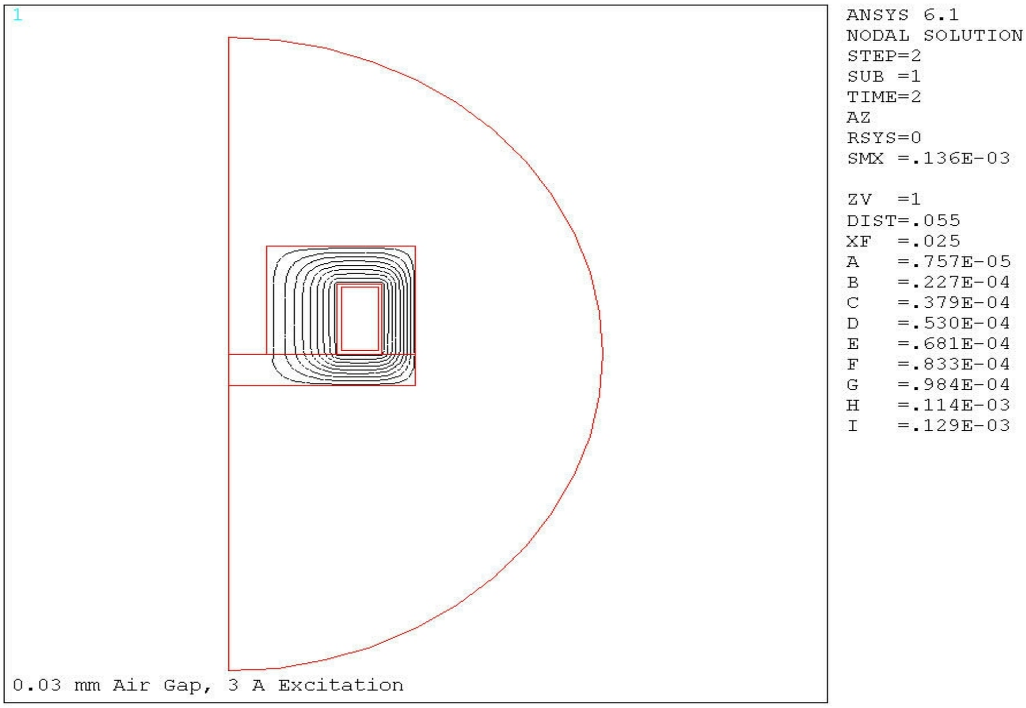

Figure 6.8: Flux Lines at 0.03mm Air Gap, 3A Excitation

the number of times steps specified for a particular load step. The measured and simulated voltage impulses for 24V, 42V and 50V cases are plotted in Figures 6.9, 6.12 and 6.15 respectively. The three voltage levels were used to investigate the affect of voltage pulse magnitude on current and force response. A pulse duration of 1.5ms was specified to achieve relatively high peak excitation levels without overloading the coil. The duration is also reasonable when considering a typical valve flight time of 3-4ms. In all three cases, the measured pulse was not found to exhibit the ideally square waveform. Rather, the voltage would start at a value typically two to three volts below the desired value and then drop until being switched off after 1.5ms. The drop in voltage is attributed to the finite power available from the Sorensen power supply. The supply is rated to 1kW continuous output and cannot deliver a steady state current in excess of 18A. The power supply limitation was exacerbated at higher

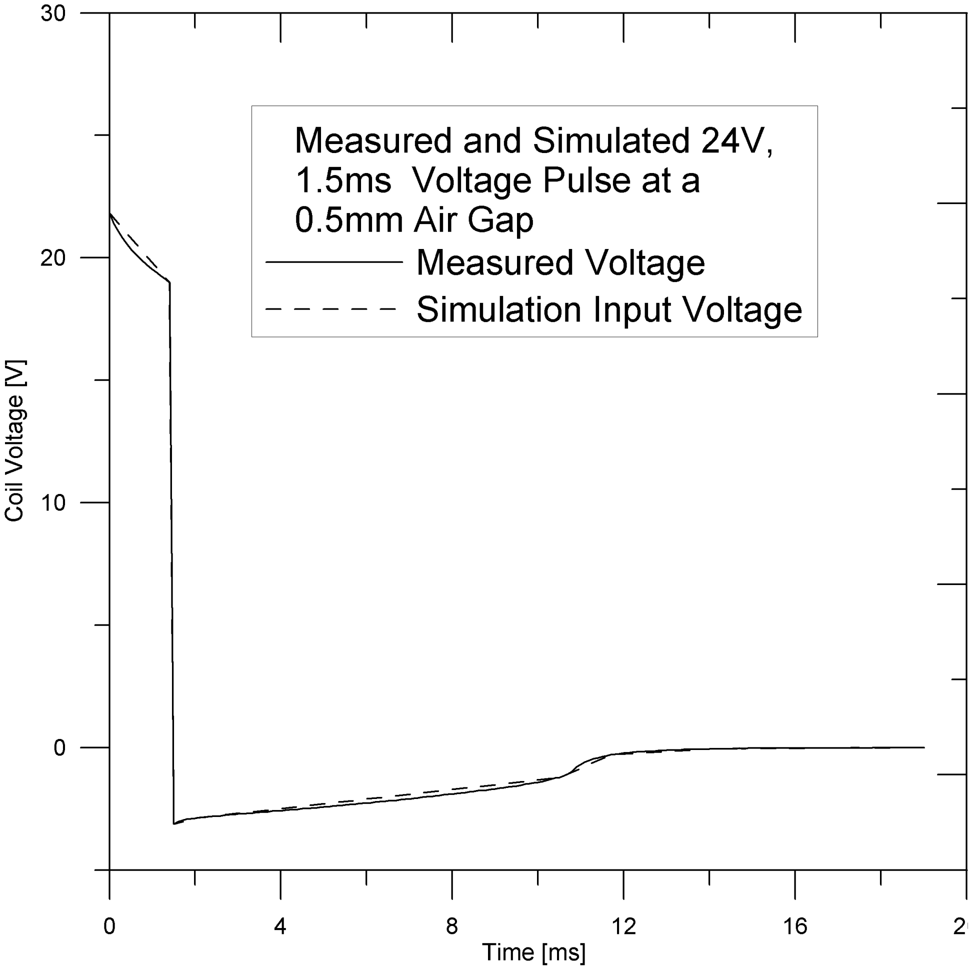

Figure 6.9: Measured and Input 1.5ms 24V Pulse

voltage levels, as the higher voltage allows for a faster current response and consequently, a higher and more rapid power demand. This is supported by observing that the change in voltage over the pulse duration for the 24V case was only 3V but over 6V for the 50V case. It was also observed that voltage can greatly influence current response time and a means of temporarily increasing voltage output may be of benefit in a real system. For the 0.5mm air gap case, the time required for armature force to reach 100N was 1.33ms, 0.65ms and 0.56ms for the respective 24V, 42V and 50V excitation cases. This suggests an inverse exponential relation between force rise time and voltage excitation (as predicted by linear theory as well).

In all cases, the measured initial voltage was approximately 2V less than the specified initial voltage. For example, despite the power supply being initialized to 24V, the initial measured coil voltage pulse was 22V. After consultation with the power electronics designer, it was concluded the initial drop is attributed to power electronic transistor and power line losses. After the 1.5ms pulse duration elapses, the supply is switched off and a negative voltage across the coil is observed. This may be explained by a back EMF being produced by the collapsing magnetic field. As Faraday's law states, a changing magnetic field will produce a current in a closed loop of coil. As the magnetic field dissipates, a counter current is generated in the coil and a measurable voltage of reversed polarity is produced until the stored energy is fully dissipated.

6.2.2 Current & Force Response

Current response for the three voltage cases are plotted in Figures 6.10, 6.13 and 6.16. The current and force results are presented for the 0.5mm position as it was observed from the static results that the gap is small enough to illustrate linear theory breakdown but large enough to be of interest when controlling landing speeds. Although results from positions other than 0.5mm were measured and simulated, they are not presented as they are of a similar nature and offer no further conclusions of the transient behavior or model performance.

The transient armature force is shown in Figures 6.11, 6.14 and 6.17. At air gaps greater than 2mm, a detailed force response was beyond the resolution of the load cell used. The impulse forces experienced at air gaps less than 0.2mm caused the armature to deflect and contact the back iron pole face. Besides the nonuniform air gap caused by armature deflection, pole face contact results in the armature force only being partially transmitted to the load cell, making any force measurements erroneous.

Current and force rise occur nearly simultaneously with only a 0.2ms difference in

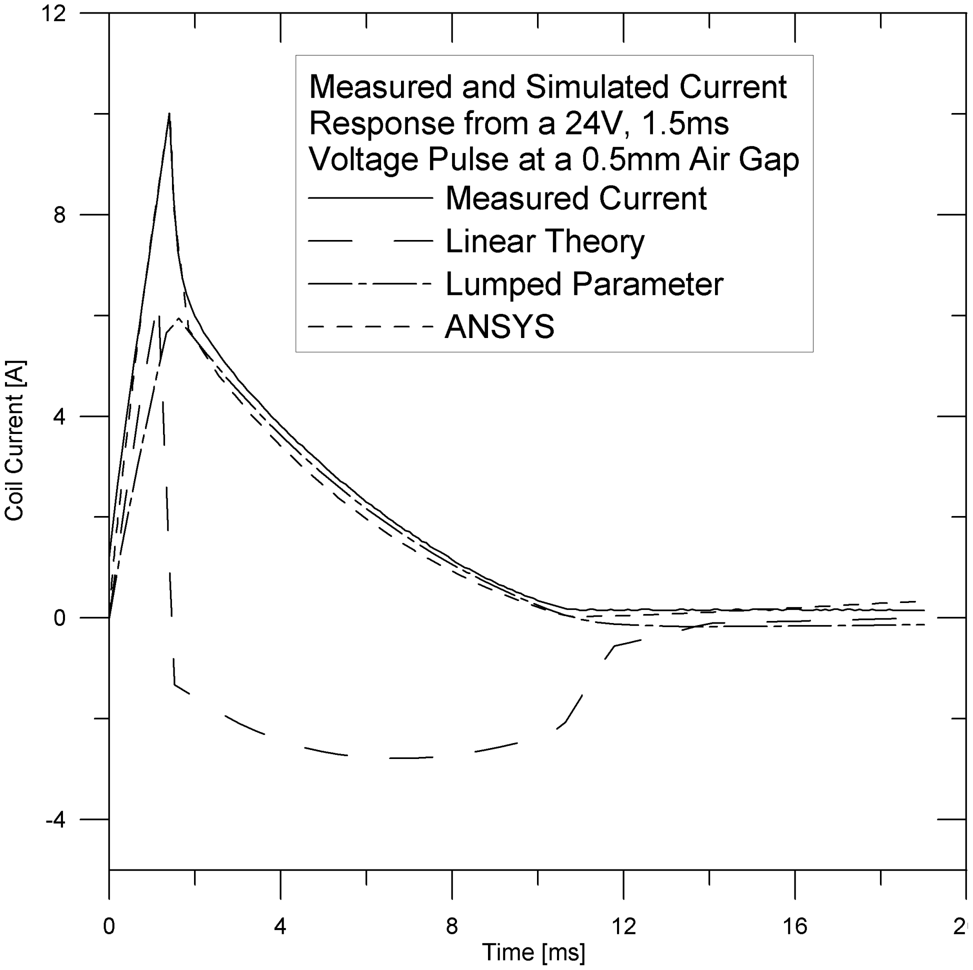

Figure 6.10: Coil Current Response to a 24V 1.5ms Voltage Pulse

peak value occurrence for all three excitation cases. This time difference may be attributed to the time required for current level to sufficiently change the armature flux and force. In the experimental case, some additional time may be required for the load pulse to propagate through the aluminum load rod and load cell. The jagged experimental force curve suggests a resonate response of the actuator or load cell structure due to the applied load pulse. The armature is also suspected of deflecting as the peak force loads are consistently above the peak ANSYS predictions (the only model that accounts for eddy currents).

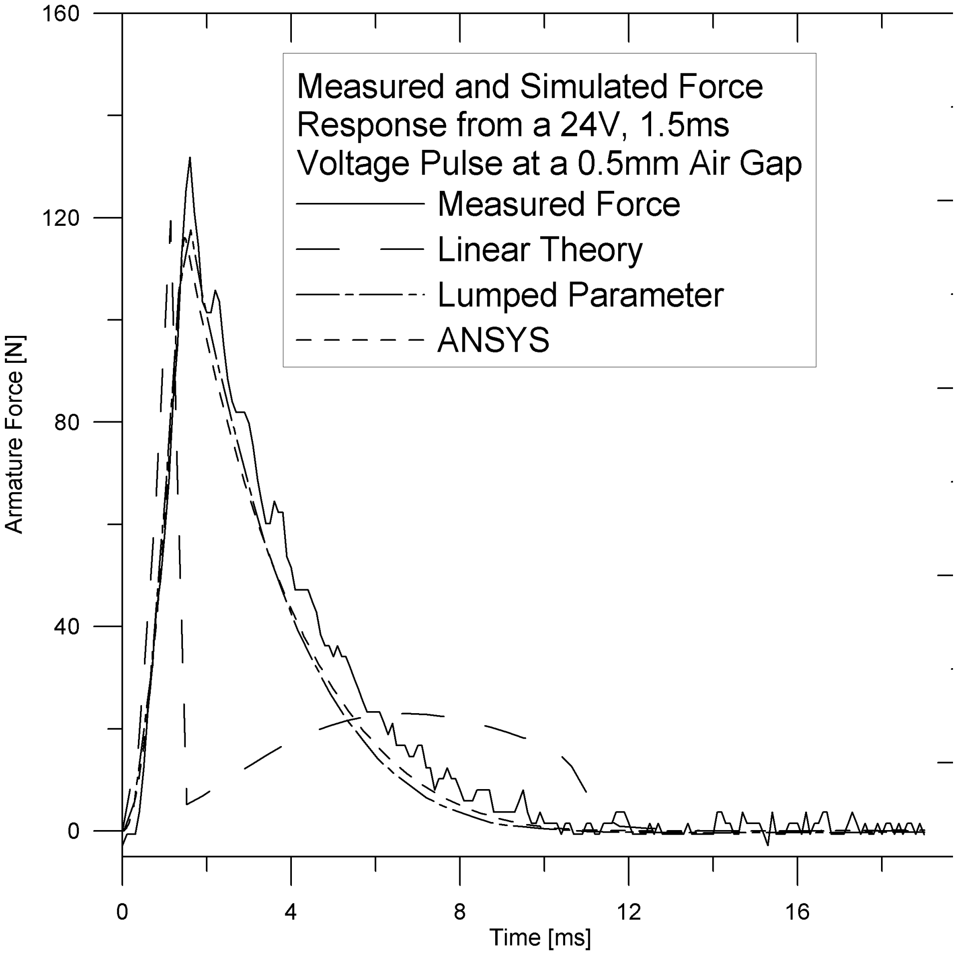

Figure 6.11: Armature Force Response to a 24V 1.5ms Voltage Pulse

6.2.2.1 Linear Model Transient Results

For the linear transient simulations, the derived equation for inductance and Equation 3.75 was used to predict current and force rise with respect to time. Inductance was calculated for an air gap of 0.5mm and Simulink was used to evaluate the resulting current and force response for the three time dependant input voltages. Recall that the linear magnetic expression for current rise neglects eddy current effects. Also note that at air gaps of less than 1mm, average inductance error increases in an inversely squared manner as a result of not accounting for material saturation and nonlinear field effects. Consequently, the poor experimental agreement observed for

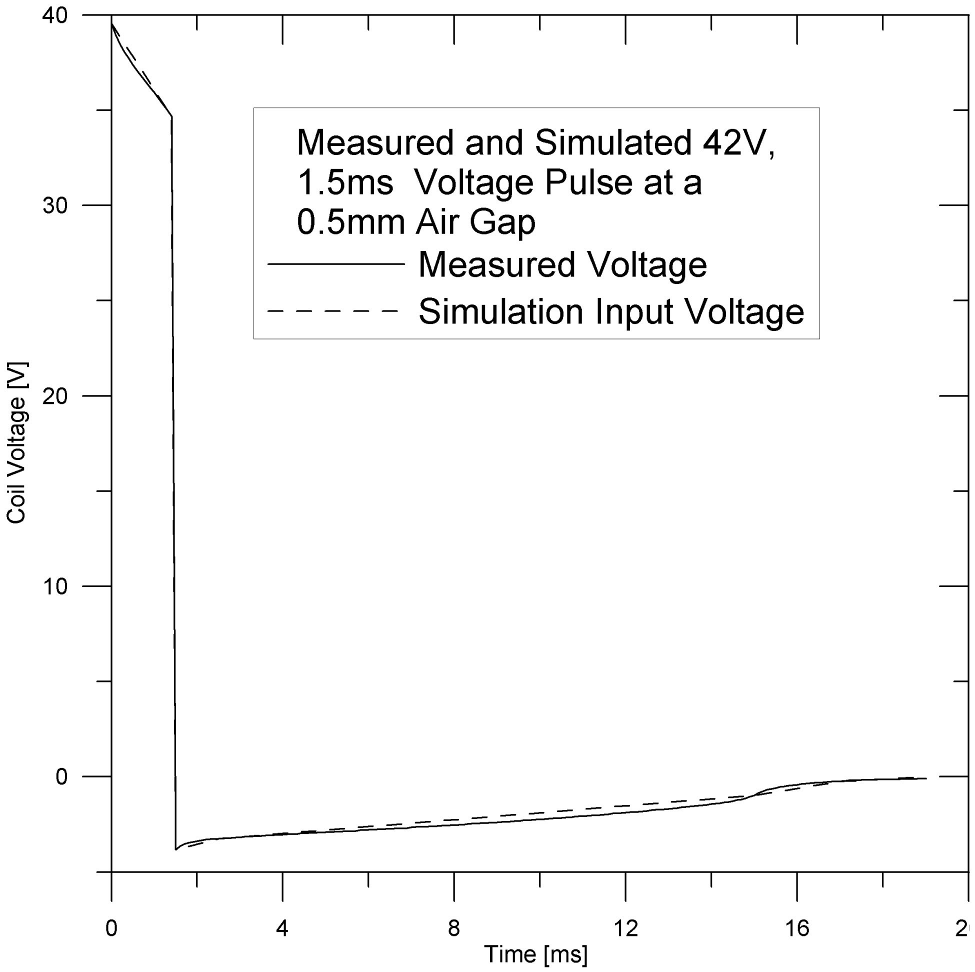

Figure 6.12: Measured and Input 1.5ms 42V Pulse

both current and force predictions generated by the linear model are not surprising. Thus, the results for the other excitation cases have been omitted.

6.2.2.2 Modified LPM Transient Results

The LPM used for simulating the electric, magnetic and mechanical actuator subsystems was modified so that the armature remained at a fixed position of 0.5mm. The three time dependant voltages are used to drive two subsequent lookup tables generated by the ANSYS static force and flux results. The model is thus capable of approximating material saturation and nonlinear field effects such as leakage and

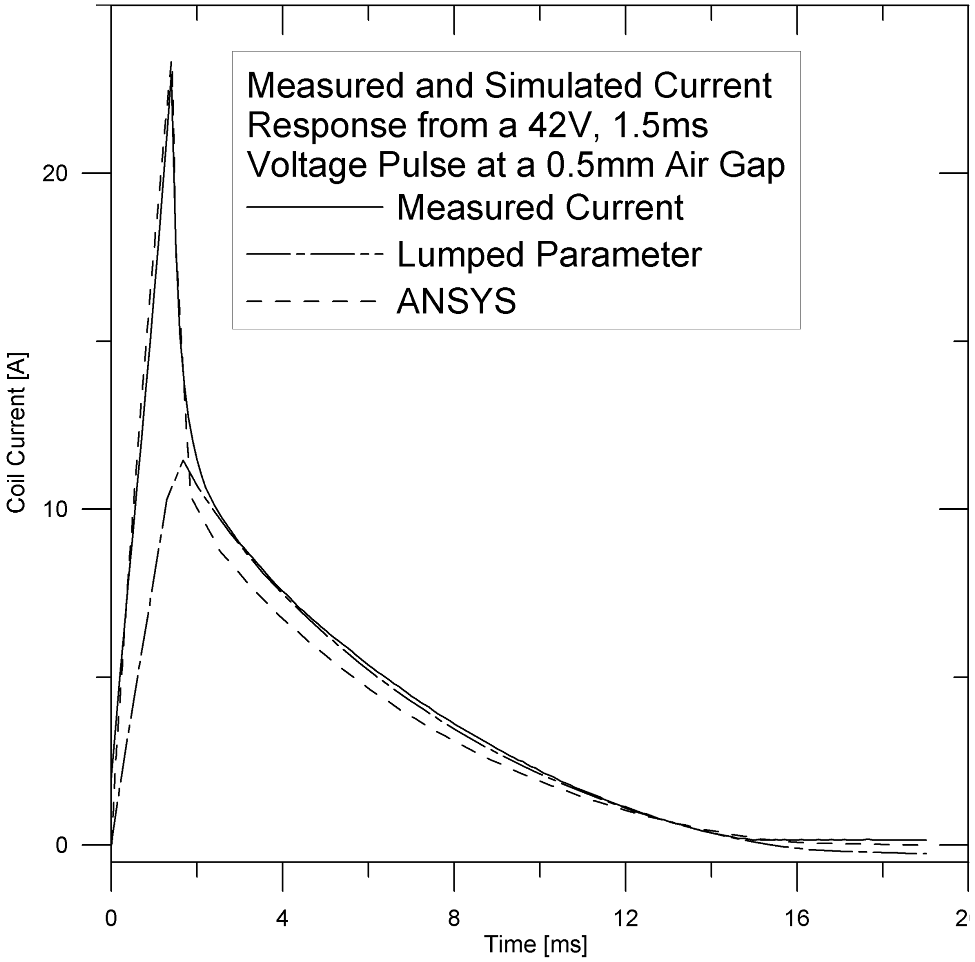

Figure 6.13: Coil Current Response to a 42V 1.5ms Voltage Pulse

fringing. However, the LPM neglects eddy currents. Despite these relatively large discrepancies, force prediction was within relatively good agreement with the measured results. Relative peak force errors are 10.8%, 4.8% and 0.5% for the 24V, 42V and 50V cases respectively. Current and force decay predictions were also quite close suggesting an accurate inductance or time constant estimate. Just as the rate of current and force rise is dependant on the system inductance, so to is the rate of decay. This effective time constant may be considered as the inductance divided by the coil resistance, $\tau = \frac{L}{R}$. Substituting the time constant into Equation 3.75, the linear theory expression for current response, results in $I = 0.63\frac{V}{R_{Coil}}$. This relation

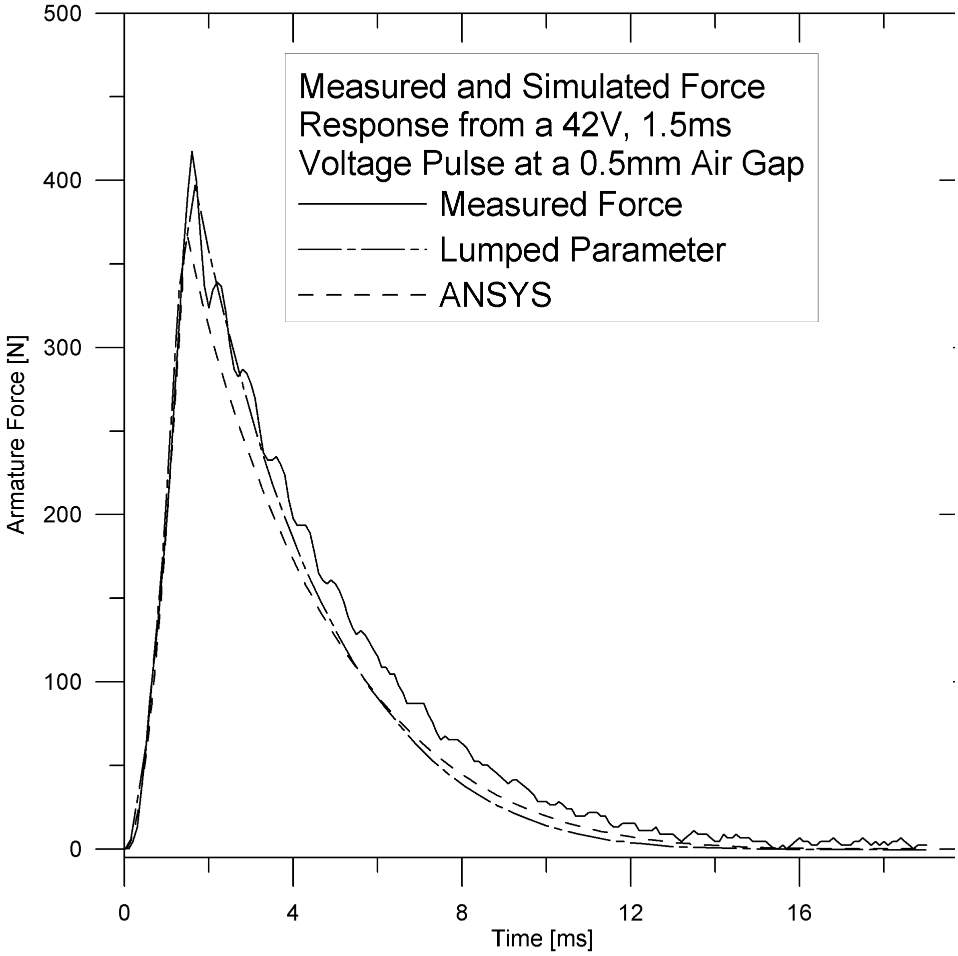

Figure 6.14: Armature Force Response to a 42V 1.5ms Voltage Pulse

also explicitly demonstrates the effect voltage excitation has on current response time. The close agreement between the experimentally measured and LPM predicted force suggests that the LPM is a valid model for transient force prediction.

6.2.2.3 ANSYS Transient Results

Generally, ANSYS predicted close agreement of force and current response with respect to the measured results and for the entire simulation duration. Maximum errors of 1.9% and 11.9% were observed for peak current and force errors respectively. The error may be largely due to armature deflection. The reduced air gap would account

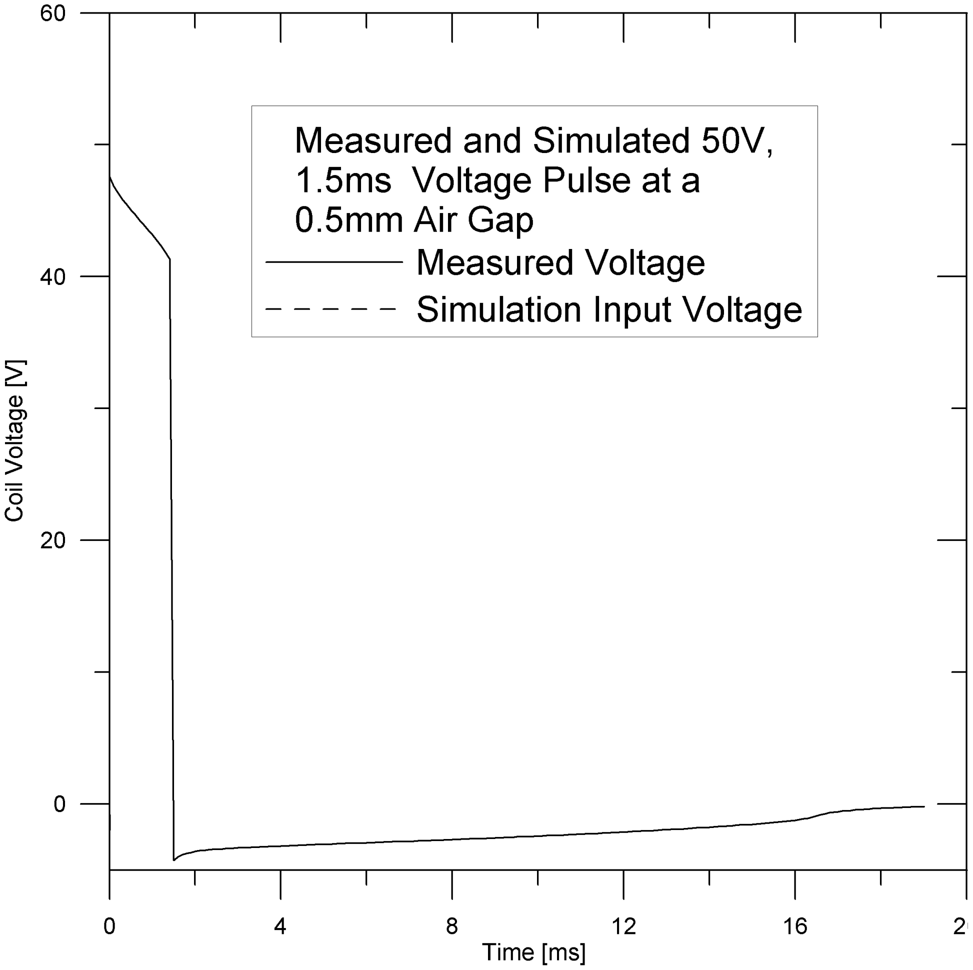

Figure 6.15: Measured and Input 1.5ms 50V Pulse

for the higher experimentally measured peak loads. This is supported by the increasing amount of error with increasing voltage. As a result, a higher impulse voltage results in a higher deflection causing a greater force discrepancy. Since the LPM does not account for eddy current generation, it would be expected that the model would over predict force estimates. The observation of the close agreement between the LPM and experimental transient force thus suggests that the experimental measurements are suspect to armature deflection. The 2D axisymmetric assumption may also contribute to the force error. In addition, the back iron and armature steel conductivities are approximate due to unavailable data. The transient models used a typical

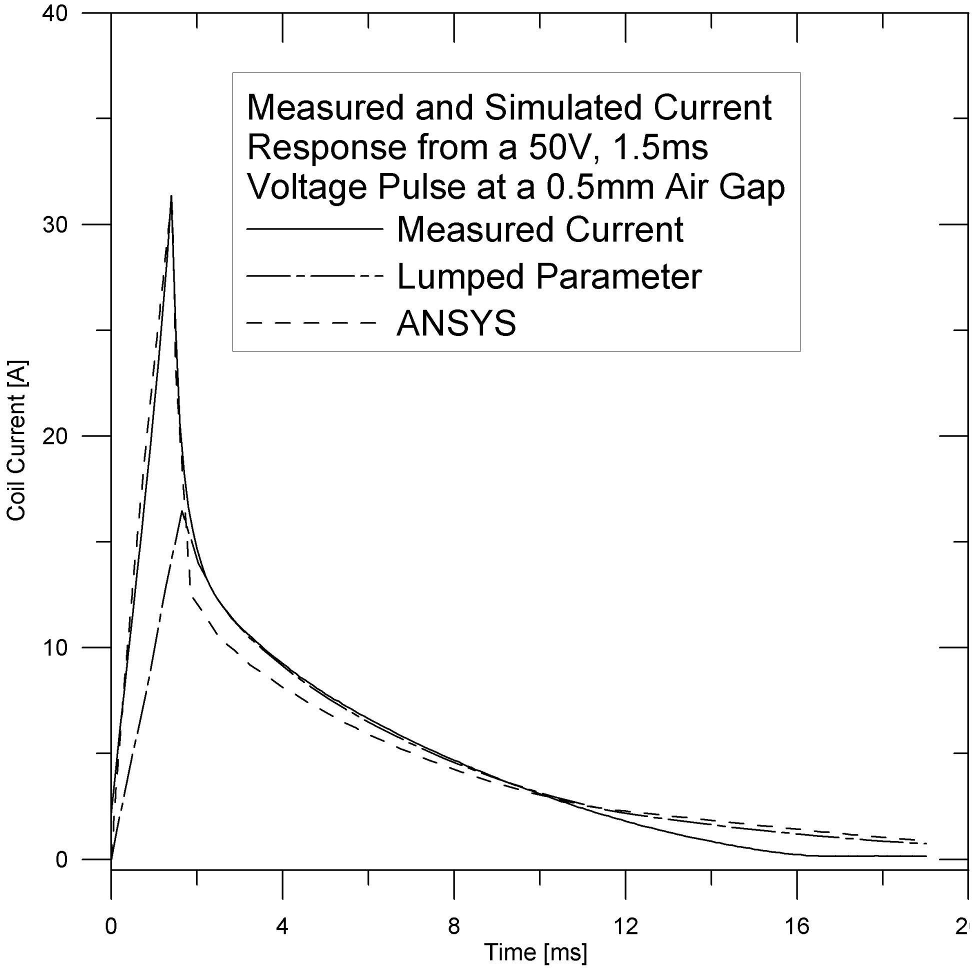

Figure 6.16: Coil Current Response to a 50V 1.5ms Voltage Pulse

conductivity value for silicon steel, hence eddy currents may not be accounted for as accurately as possible. However, due to the close current and force predictions, the transient model is not suspect at this time. Considering the assumptions and sources for measurement error, the model performed reasonably well. Although the model did not account for armature motion, one possible application may be armature release performance estimation. For example, a steady state holding current may be applied, after which the voltage may be switched to the -42V mode in order to rapidly reduce the magnetic flux and armature force. The timing of such events is critical to combustion engine performance. During such an operation, the armature may realistically

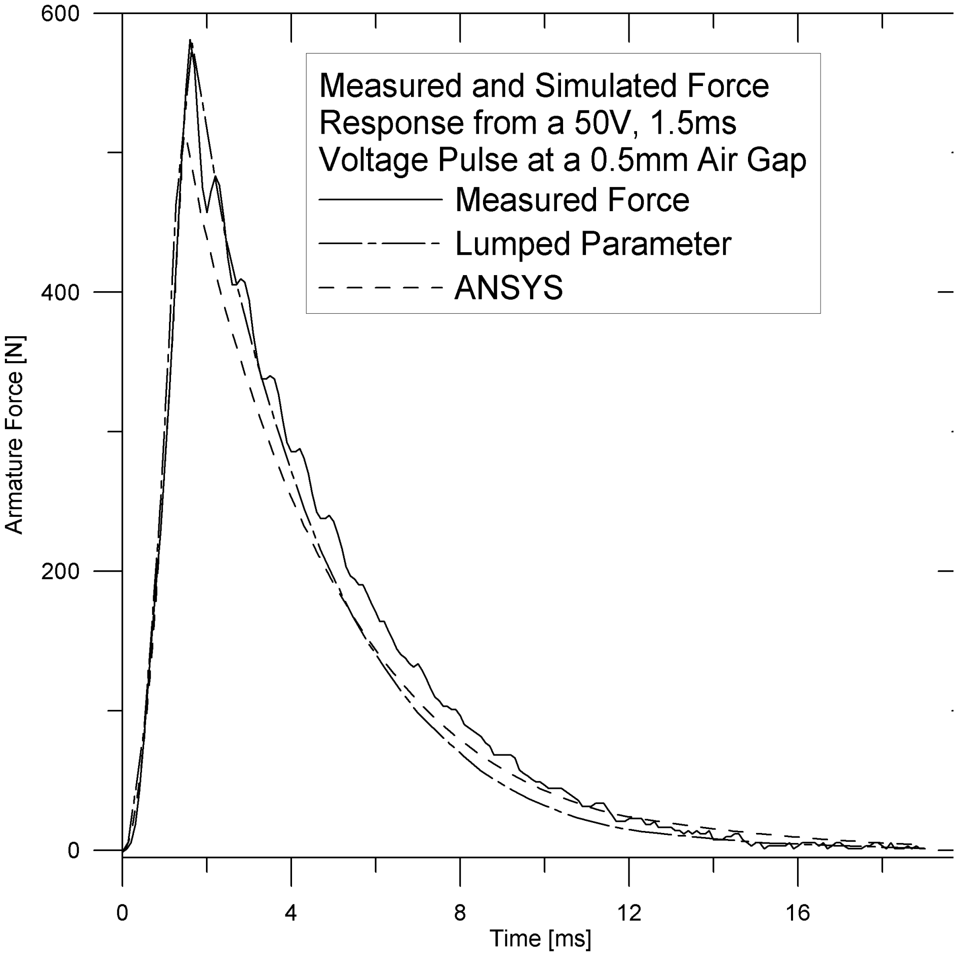

Figure 6.17: Armature Force Response to a 50V 1.5ms Voltage Pulse

be approximated as fixed until motion is incipient. It may also be possible to use this model to predict the eddy current losses. Any estimate predicting such losses may be incorporated in the LPM to enhance model accuracy. The transient FEA model could also be extended to three dimensions so that more accurate eddy current paths may be accounted for.

6.2.2.4 ANSYS Transient Flux Contour Plots

ANSYS was used to produce flux line contour plots at several instances in time to again assist in illustrating the effects of flux leakage and fringing as well as present

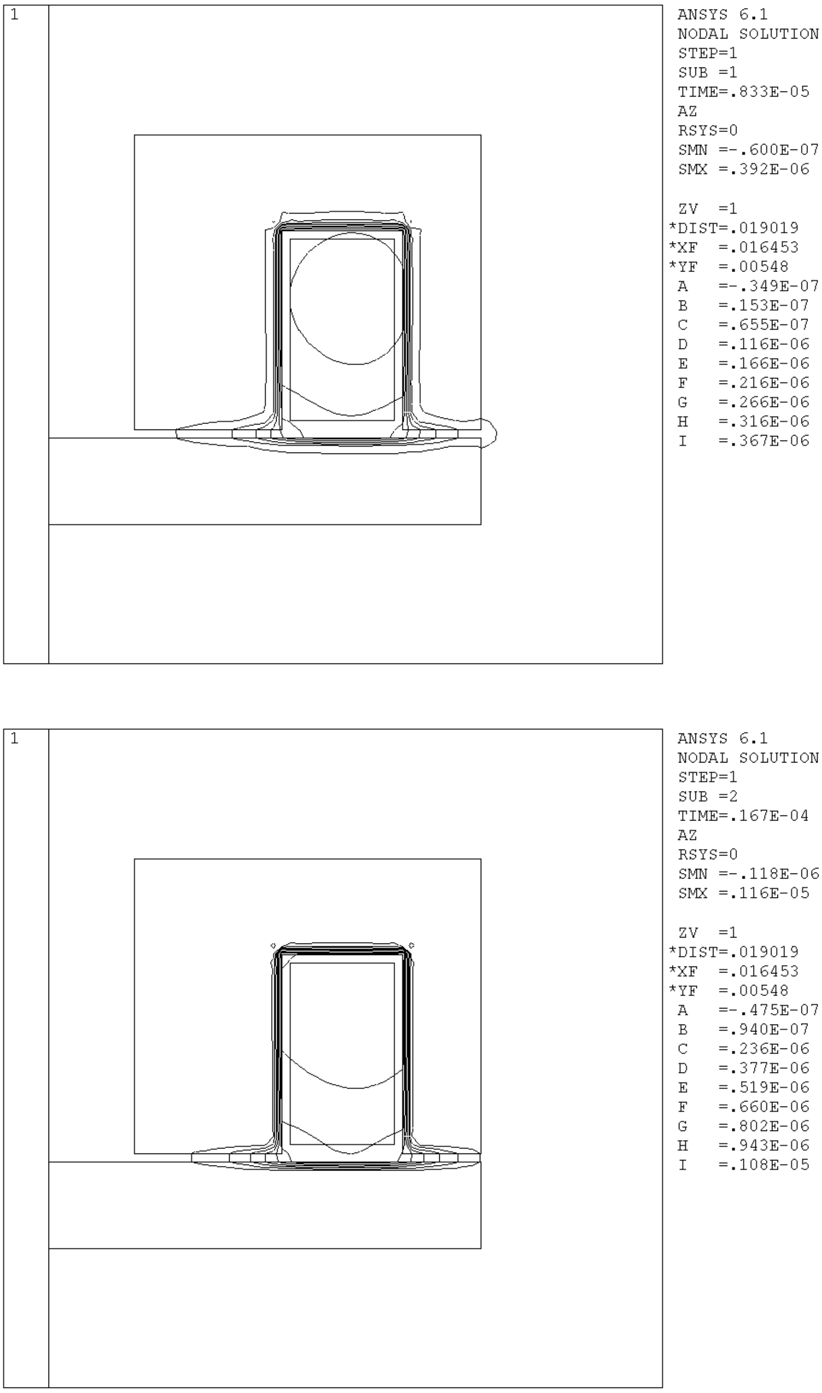

```
ANSYS 6.1
NODAL SOLUTION
STEP=1
SUB =1
TIME=.833E-05
AZ
RSYS=0
SMN =-.600E-07
SMX =.392E-06

 ZV  =1
*DIST=.019019
*XF  =.016453
*YF  =.00548
 A   =-.349E-07
 B   =.153E-07
 C   =.655E-07
 D   =.116E-06
 E   =.166E-06
 F   =.216E-06
 G   =.266E-06
 H   =.316E-06
 I   =.367E-06
```

```
ANSYS 6.1
NODAL SOLUTION
STEP=1
SUB =2
TIME=.167E-04
AZ
RSYS=0
SMN =-.118E-06
SMX =.116E-05

 ZV  =1
*DIST=.019019
*XF  =.016453
*YF  =.00548
 A   =-.475E-07
 B   =.940E-07
 C   =.236E-06
 D   =.377E-06
 E   =.519E-06
 F   =.660E-06
 G   =.802E-06
 H   =.943E-06
 I   =.108E-05
```

Figure 6.18: Flux time series plots at 0.008ms and 0.016ms

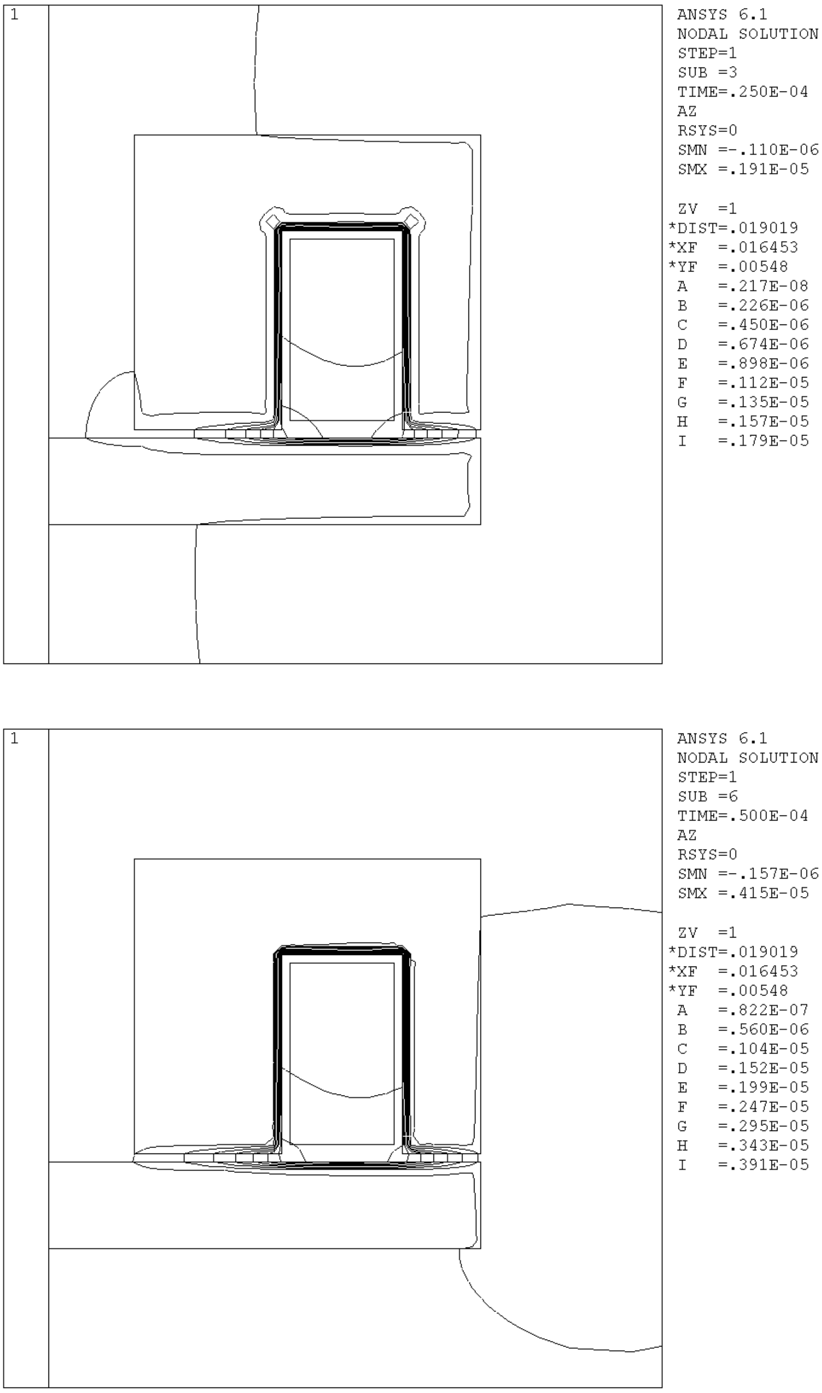

Figure 6.19: Flux time series plots at 0.025ms and 0.05ms

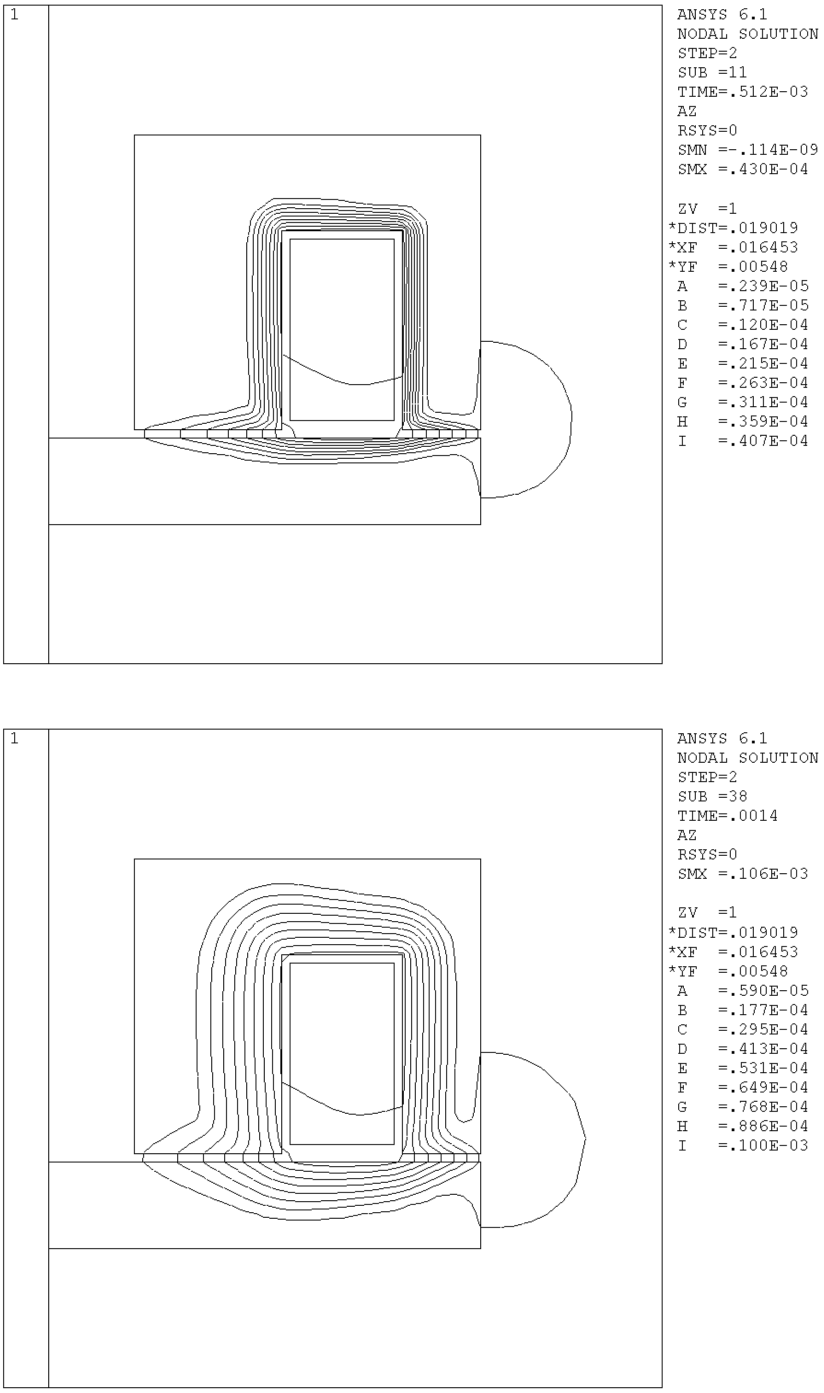

Figure 6.20: Flux time series plots at 0.51ms and 1.40ms

qualitative insights to flux behavior over time. Figures 6.18 through 6.20 illustrate six different instantaneous flux contour plots of the opener at a 0.5mm air gap using the same 42V 1.5ms pulse excitation illustrated in Figure 6.12. The plots correspond to respective times of 0.008ms, 0.016ms, 0.025ms, 0.05ms, 0.51ms and 1.40ms. The times were chosen to illustrate the most dramatic, yet typical flux contours during the course of excitation. Note the small closed contours at each corner of the back iron just above the coil region at 0.025ms in Figure 6.19. These small contours indicate the presence of eddy currents of sufficient magnitude to generate their own magnetic flux in an opposing direction, as indicated by their negative values. The presence of larger circulations have also been observed in the armature for different operating cases. Also noteworthy is the way in which flux is constrained to the inner back iron and armature surface for substantial time periods. This 'skin effect' is also likely the result of eddy currents inhibiting full field penetration by generating an opposing flux. Although the presence of eddy currents have a significant affect on flux path behavior, they will likely not have a significant effect on the overall force prediction as demonstrated with the modified lumped parameter model.

6.3 Lumped Parameter Model Results

The Simulink lumped parameter model is used to rapidly generate overall actuator performance results, as well as form the model from which control development may take place. Flux results for the static ANSYS simulations are inverted and used in a 2D lookup table which relates flux and position to a current excitation level. The current excitation level is passed to another ANSYS generated 2D lookup table which relates current excitation and position to the static force. This force is then used with other mechanical parameters such as spring and gas forces which consequently influence armature acceleration, velocity and position. Measured spring constants and valve and armature masses are used in the model to enhance accuracy. The most significant advantage to the LPM is the speed in which results may be achieved. When contrasted with the same ANSYS transient results which took in excess of thirty minutes to compute, the LPM results took less than a few seconds with comparable accuracy. Despite that much of the dynamic experimental equipment has been acquired and setup, no dynamic experiments have been performed which are capable of fully validating (or refuting) the LPM. This is due to the complexity of the required control system which is presently being developed. However, the magnetic and electric systems are likely to be more complicated than the mechanical portion of the model and little difficulty is expected to achieve accurate mechanical performance predictions.

6.4 Summary

Results contrasting static experimental, ANSYS and linear force as a function of air gap and excitation have been presented. It was observed that a 2D axis-symmetric ANSYS model was capable of accurately predicting static and transient magnetic actuator performance. As well, the static results can be confidently used in a LPM to predict transient force response from an arbitrary voltage input. It was shown that ANSYS is capable of accurately predicting transient responses, however, the fixed armature position and relatively large computational time required to perform such analyses make it somewhat prohibitive for practical use.

CHAPTER 7

CONCLUSIONS AND FURTHER RESEARCH

Due to the many constraints and requirements of electromagnetic gas exchange valve actuation, the design and implementation of the devices has proven to be exceptionally challenging. The multi-disciplinary nature of the problem has also hindered development as the design involves insights of electricity, magnetism, heat transfer, vibrations and control system theory. A development process that emphasizes the need for accurate simulation is presented as a means of reducing the dependency of design through iterative prototype construction and testing. Specifically, an axisymmetric 2D FEA model has been developed to demonstrate a feasible method of actuator simulation. The model has been contrasted with an equivalent experimental prototype to validate the use of FEA simulation techniques. Similarly, a model was developed using linear magnetic theory and contrasted with experimental results. Based on this work the following conclusions may be made:

1. The FEA model is sufficiently accurate with static force prediction errors not exceeding 10% over the full operating range.

2. For steady currents the linear theory model predicted a force / air gap relationship of $F = \frac{c_1}{(c_2+x_{gap})^2}$. Without fitting this relationship to existing data, the linear model demonstrated errors in excess of 200% at excitations beyond

1000MMF and air gaps of 0.5mm or less. Consequently, for this actuator configuration, it is not recommended to use a linear model at air gaps less than 1mm or excitation levels exceeding 1000MMF as landing speed control will likely occur at such operating points. An alternative is to calibrate the linear model to experimental results, however this requires the fabrication of a prototype.

3. It was observed however, that linear magnetic theory could be used at larger air gaps and lower excitation levels, primarily due to lack of material saturation.

4. As a means of simulating the dynamic response of the actuator system, the FEA results are incorporated in a LPM. The LPM provides a means of investigating the affects of external parameters on the overall actuator performance while avoiding the computational demands of a FEA. For example, the influence of time varying parameters such as gas forces, voltage waveforms and friction can be predicted in minutes rather than hours of computational time. Consequently, control system development can be expedited.

5. The LPM model was contrasted with the results from an experimental transient force and transient FEA model for the case of a fixed armature position and a voltage pulse. Peak transient force errors were observed to be 11% and 12% for the LPM and ANSYS transient models respectively with both models closely predicting the experimental transient response for the entire simulated time duration.

6. In contrast, the linear model transient force estimation was generally so poor that it is not appropriate to contrast the results with respective LPM and ANSYS simulations.

7.1 Further Research

In order to further the proposed design process described in Section 5.2 the following highlights possible areas of future work.

7.1.1 FEA ANALYSIS

1. During the transient experiments it was observed that the armature was subjected to sufficiently large magnetic forces to cause significant deflection, particularly at air gaps of 0.2mm or less. To account for this, it may be desired to use ANSYS to predict the transient armature deflection. PLANE13 elements posses both magnetic potential and deflection degrees of freedom. Thus, if they were meshed in the armature region it is possible to account for both the magnetic attractive force and the resulting deflection by first solving the magnetic system and transfer the resultant force loads to a structural analysis. The deflected geometry could then be used in the solution of the magnetic system. This process may continue until equilibrium is achieved (for a static analysis), or for each time step (in a transient analysis).

2. As a further extension, it may be of interest to conduct a full motion dynamic analysis capable of predicting the interaction of magnetic and spring forces as well as a changing air gap and velocity induced currents. Conducting such a simulation is a challenging task as the air gap elements must be capable of accommodating the armature motion. The model would also be much more computationally expensive than the current simulation. For example, in contrast to a LPM, a large amount of computation time would be required when investigating the affect of various time varying voltage inputs on landing speed.

3. The transient 2D model developed in this work could be extended to a 3D model

to investigate the axis-symmetric and 2D assumption. The 3D model would be able to produce an accurate field distribution and hence force prediction. In addition, contrasting the eddy currents of a full 3D geometry with a 2D model may also be of interest.

7.1.2 LPM Development

4. The LPM presented incorporates the nonlinear material saturation and field solution but could be further enhanced. The model could be extended to simulate time varying gas forces as well as the three available power electronic switching modes of +42V, 0V and −42V.

5. For a more realistic engine simulation, the model could also be extended to include a hydraulic lash adjuster with temperature dependant viscosity.

6. Upon sufficient model and control development, the LPM should be validated and contrasted with equivalent test bench experiments. The control need only be able to consistently latch and release the armature to validate the mechanical system response.

7.1.3 Control Development

7. Upon satisfactory LPM development and accuracy, a control system can be designed to mitigate armature landing velocities. During this process hardware requirements such as controller sampling rate, power supply limits and sensor resolution can be predicted. Trajectory planning and energy management can also be addressed. Different control designs can be contrasted and compared with experimental test bench results.

8. A feedforward system utilizing parameter estimation may be developed to predict system disturbances. If for example it is assumed that the spring constant and damping ratio are constant and known, by recursively observing the valve trajectory it may be possible to predict a system disturbance force such as an anomalous combustion variation. This would give the ability to adjust the electromagnetic force applied to the armature to compensate, thereby improving trajectory and ultimately impact velocities.

9. Experimental tests could be conducted with the test bench apparatus by varying the cavity air pressure to simulate gas disturbances or utilizing a cold room to alter valve actuator viscous damping.

10. The affect of mechanical stability on control performance can be studied.

11. The minimum hardware requirements for successful control can be contrasted with available on-board technologies. For example, closed loop motion control of each actuator may be prohibitively expensive for a commercially viable vehicle. In which case the fundamental actuator and control design may need to be re-evaluated or more sophisticated power electronics and energy conversion may need to be developed.

7.1.4 Alternate Actuators

12. It will be of benefit to consider the characteristics of a variety of electromagnet actuator configurations. For example, a hinged actuator configuration was demonstrated to illustrate a potential improvement to the traditional linear actuator. The hinged configuration was shown to have a flatter force-position relationship which will subsequently enhance mechanical stability. If prototypes of a different configuration can be acquired, equivalent ANSYS, LPM, and con-

trol simulations could be contrasted with experimental test bench experiments. The results could be contrasted with those obtained from the linear actuator studied in this work. In this way, the affect of actuator configuration on control system performance may be further quantified.

13. Comparisons of different actuator manufacturing cost, reliability and packaging could be performed.

7.1.5 Sensor Development

14. Alternate methods of measuring armature positions are being developed due the excessive costs associated with existing high speed and resolution sensor technologies. The ANSYS model and actuator prototype may be modified to include an inductive coil that is capable of measuring back iron flux.

15. By also measuring coil current, it may be possible to predict armature position as [Rossi and Alberto, 2001] suggests. A coil could be modeled in ANSYS to investigate the sensor performance.

16. Upon successful ANSYS simulation, hardware and signal processing could be developed to test an experimental sensor.

17. Methods of online calibration can also be explored, perhaps in conjunction with the system parameter estimation techniques.

BIBLIOGRAPHY

[ANS, 2002] (2002). *ANSYS Theory Reference.* ANSYS Inc. Release 6.1.

[Allen and Law, 2002] Allen, J. and Law, D. (2002). Production electro-hydraulic variable valve-train for a new generation of i.c. engines. *SAE Paper 2002-01-1109.*

[Atkins and Koch, 2003] Atkins, M. and Koch, C. (2003). A well-to-wheel comparison of several powertrain technologies. *SAE Paper 2003-01-0081.*

[Barros da Cunha et al., 2000] Barros da Cunha, S., Hedrick, J., and Pisano, A. (2000). Variable valve timing by means of a hydraulic actuation. *SAE Paper 2000-01-1220.*

[Butzmann et al., 2000] Butzmann, S., Melbert, J., and Koch, A. (2000). Sensorless control of electromagnetic actuators for variable valve train. *SAE Paper 2000-01-1225.*

[Chillet and Voyant, 2001] Chillet, C. and Voyant, J. (2001). Design-oriented analytical study of a linear electromagnetic acutator by means of a reluctance network. *IEEE Transactions on Magnetics*, 37:3004–3011.

[Flierl and Klüting, 2000] Flierl, R. and Klüting, M. (2000). The third generation of valvetrains - new fully variable valvetrains for throttle-free load control. *SAE Paper 2000-01-1227.*

[Gecim, 1993] Gecim, B. (1993). Analysis of a lost-motion-type hydraulic system for variable valve actuation. *SAE Paper 930822.*

[Giglio et al., 2002] Giglio, V., Iorio, B., Police, G., and di Gaeta, A. (2002). Analysis of advantages and of problems of electromechanical valve actuators. *SAE Paper 2002-01-1105.*

[Griffiths, 1999] Griffiths, D. (1999). *Introduction to Electrodynamics.* Prentice Hall.

[Hara et al., 2000] Hara, S., Hidaka, A., Tomisawa, N., Takemura, S., and Nohara, T. (2000). Application of a variable valve event and timing system to automotive engines. *SAE Paper 2000-01-1224.*

[Henry, 2001] Henry, R. (2001). Single-cylinder engine tests of a motor-driven variable-valve actuator. *SAE Paper 2001-01-0241.*

[Hoffmann and Stefanopoulou, 2001] Hoffmann, W. and Stefanopoulou, A. (2001). Valve position tracking for soft landing of electromechanical camless valvetrain. *International Federation of Automatic Control (IFAC), Advances in Automotive Control.*

[Kim et al., 1997] Kim, D., Anderson, M., Tsao, T., and Levin, M. (1997). Dynamic model of a springless electrohydraulic valvetrain. *SAE Paper 970248.*

[Koch et al., 2002] Koch, C., Lynch, A., and Chladny, R. (2002). Modeling and control of solenoid valves for internal combustion engines. *Published in the proceedings of the 2nd International Federation of Automatic Control (IFAC) Conference on Mechatronic Systems.*

[Lancefield et al., 1993] Lancefield, T., Gayler, R., and Chattopadhay, A. (1993). The practical application and effects of a variable event valve timing system. *SAE Paper 930825.*

[Lequesne, 1990] Lequesne, B. (1990). Fast acting, long-stroke solenoids with two springs. *IEEE Transactions on Industry Applications*, 26:848–856.

[Lequesne, 1996] Lequesne, B. (1996). Permanent magnet linear motors for short strokes. *IEEE Transactions on Industry Applications*, 32:161–168.

[Lequesne, 1999] Lequesne, B. (1999). Design and optimization of two-spring linear actuators. *European Transactions on Electrical Power*, 9:377–383.

[Longstaff and Holmes, 1975] Longstaff, K. and Holmes, S. (1975). Internal combustion engines. *U.S. Patent No. 3,882,833.*

[Lynch et al., 2003] Lynch, A., Koch, C., and Chladny, R. (2003). Nonlinear observer design for sensorless electromagnetic actuators. *To be published in the proceedings of the 3rd International Conference on Dynamics of Continuous, Discrete and Impulsive Systems, May 2003.*

[Melgoza and Rodger, 2002] Melgoza, E. and Rodger, D. (2002). Comparison of table models of electromagnetic actuators. *IEEE Transactions on Magnetics*, 38:953–956.

[Moro et al., 2001] Moro, D., Ponti, F., and Serra, G. (2001). Thermodynamic analysis of variable valve timing infuence [sic] on si engine efficiency. *SAE Paper 2001-01-0667.*

[Nakamura et al., 2001] Nakamura, M., Hara, S., Yamada, Y., Takeda, K., Okamoto, N., Hibi, T., Takemura, S., and Aoyama, S. (2001). A continuous variable valve event and lift control device (vel) for automotive engines. *SAE Paper 2001-01-0244.*

[Pierik and Burkhard, 2000] Pierik, R. and Burkhard, J. (2000). Design and development of a mechanical variable valve actuation system. *SAE Paper 2000-01-1221.*

[Piron et al., 1999] Piron, M., Sangha, P., G.Reid, Miller, T., Ionel, D., and Coles, J. (1999). Rapid computer-aided design method for fast-acting solenoid actuators. *IEEE Transactions on Industry Applications*, 35:991–999.

[Pischinger and Kreuter, 1984] Pischinger, F. and Kreuter, P. (1984). Electromagnetically operating actuator. *U.S. Patent No. 4,455,543.*

[Pischinger et al., 2000] Pischinger, M., Salber, W., van der Staay, F., Baumgarten, H., and Kemper, H. (2000). Benefits of the electromechanical valve train in vehicle operation. *SAE Paper 2000-01-1223.*

[Richeson and Erickson, 1989] Richeson, W. and Erickson, F. (1989). Pneumatic actuator with permanent magnet control valve latching. *U.S. Patent No. 4,852,528.*

[Roschke and Bielau, 1995] Roschke, T. and Bielau, M. (1995). Verfahren zur modellbasierten Messung und Regelung von Bewegungen an elektromagnetischen Aktoren. *Technische Universitaet Dresden German Patent Application DE 19544207 A1.*

[Rossi and Alberto, 2001] Rossi, C. and Alberto, T. (2001). Method and device for estimating the position of an actuator body in an electromagnetic actuator to control a valve of an engine. *Magneti Marelli European Patent Application EP 1152129 A1.*

[Rossi and Tonielli, 2001] Rossi, C. and Tonielli, A. (2001). Method and device for estimating the position of an actuator body in an electromagnetic actuator to control a valve of an engine. *European Patent Application EP 1152129 A1.*

[Roters, 1941] Roters, H. (1941). *Electromagnetic Devices.* John Wiley and Sons.

[Schechter and Levin, 1996] Schechter, M. and Levin, M. (1996). Camless engine. *SAE Paper 960581.*

[Schmitz and Novotny, 1965] Schmitz, N. and Novotny, D. (1965). *Introductory Electromechanics.* The Ronald Press Company.

[Tai and Tsao, 2001] Tai, C. and Tsao, T. (2001). Quite seating control design of an electromagnetic engine valve actuator. *Proceedings of 2001 ASME Ineternational Mechanical Engineering Congress and Exposition.*

[Takashi and Iwao, 1995] Takashi, D. and Iwao, M. (1995). Valve drive device for internal combustion engine and initial position setting method for valve element. *Japan Patent Application JP 0224624.*

[Theobald et al., 1994] Theobald, M., Lequesne, B., and Henry, R. (1994). Control of engine load via electromagnetic valve actuators. *SAE Paper 940816.*

[Wang et al., 2002] Wang, Y., Megil, T., Haghgooie, M., Peterson, K., and Stefanopoulou, A. (2002). Modeling and control of electromechanical valve actuator. *SAE Paper 2002-01-1106.*

[Wang et al., 2000] Wang, Y., Stefanopoulou, A., Haghgooie, M., Kolmanovsky, I., and Hammoud, M. (2000). Modeling of an electromechanical valve actuator for a camless engine. *Proceedings of AVEC 2000. 5th International Symposium on Advanced Vehicle Control.*

[Wilson et al., 1993] Wilson, N., Watkins, A., and Dopson, C. (1993). Asymmetric valve strategies and their effect on combustion. *SAE Paper 930821.*

[Woodson and Melcher, 1968] Woodson, H. and Melcher, J. (1968). *Electromechanical Dynamics Part I: Discrete Systems.* John Wiley and Sons.

APPENDIX A

SUPPLEMENTAL ELECTROMAGNETIC THEORY

A.1 Maxwell's Equations Derived

The following entails a brief overview of the empirical laws of electricity and magnetism in order to provide a very basic derivation of Maxwell's equations.

A.1.1 Coulomb's Law

Coulomb derived an inverse squared relation from measurements he made experimentally with an electrical torsion bar.

$$\mathbf{f} = \frac{qQ\mathbf{r}}{4\pi\epsilon_0|r|^3} \tag{A.1}$$

This expression describes the force, **f** [Newtons], experienced by a point charge, q [coulombs], when brought towards another point charge of like sign, Q. Where $\mathbf{r}$[m], is a position vector from one point charge to another, and ϵ_0 is the free space permittivity constant ($8.854\text{x}10^{-12}\frac{F}{m}$). Similarly, the electric field intensity, **E** [volts per meter], of charge Q may be expressed as:

$$\mathbf{E}(\mathbf{r}) = \frac{Q\mathbf{r}}{4\pi\epsilon_0|r|^3} \tag{A.2}$$

Since electric charge occurs in multiples of the elementary unit of charge, 1.60x10^{-19}C, charge density may be expressed as:

$$\rho_e(\mathbf{r}) = \lim_{\delta V \to 0} \frac{1}{\delta V} \sum_i q_i \tag{A.3}$$

which expresses a continuum model of a sum of charges at a point located by $\mathbf{r}$ enclosed by a small volume, δV. Where δV is considered infinitesimally small when compared to the considered system's dimensions yet large enough to contain a large number of charges, q_i.

In such instances, one may assume that all charges on such a volume will experience the same electric field. Thus, for the repulsion force of a body containing a number of charges one may average the force to derive an electric force density, $\mathbf{F}$. Where,

$$\mathbf{F} = \rho_e \mathbf{E} \tag{A.4}$$

A.1.2 Gauss's Law of Electricity

An often more convenient way to relate charge density and electric field intensity is through the integral form of Gauss's Law, which is implied by Coulombs law,

$$\oint_S \epsilon_0 \mathbf{E} \cdot \mathbf{n} da = \int_V \rho_e dV \tag{A.5}$$

where $\mathbf{n}$ is the unit vector normally directed from area S which encloses volume V. It can be seen that in the case of a point charge, Equation A.5 reverts to that of Coulombs law, Equation A.1 where the surface S may be taken as a sphere centered at the location of point charge Q. A differential form of Equation A.5 may be obtained by applying the divergence theorem,

$$\oint_S \mathbf{v} \cdot \mathbf{n} da = \int_V \nabla \cdot \mathbf{v} dV \tag{A.6}$$

to result in the following:

$$\int_V (\nabla \cdot \epsilon_0 \mathbf{E} - \rho_e) dV = 0 \tag{A.7}$$

Since the integrated volume is arbitrary, one may state:

$$\nabla \cdot \mathbf{E} = \frac{\rho_e}{\epsilon_0} \tag{A.8}$$

Which is in fact one of Maxwell's equations. Both Oersted and Gauss experimented with electromagnetism and its forces upon objects such as a compass needle.

A.1.3 Gauss's Law for Magnetism

Gauss's law for magnetism is a formalized means of stating the observation that unlike electricity, free magnetic poles do not exist (at least they have yet to be observed). This implies that the net magnetic flux passing through any closed surface, S, is always zero.

$$\Phi_B = \oint_S \mathbf{B} \cdot \mathbf{n} da = 0 \tag{A.9}$$

Or, again recognizing the surface is arbitrary and applying the divergence theorem, the relation may be expressed in differential format as,

$$\nabla \cdot \mathbf{B} = 0 \tag{A.10}$$

This relation represents another of Maxwell's equations.

A.1.4 Conservation of Charge

Observed experimental evidence has shown that electric charge is always conserved. For example, an equal and opposite charge is observed on a previously neutral atom when an electron is removed. When this concept is applied to an arbitrary volume, V, enclosed by a smooth surface, S, any flow rate of charge out of the surface must be balanced by the rate of which charge decreases in the volume. A continuum variable, current density, $\mathbf{J}$ $[\frac{C}{m^2 s}]$ is often used to express this charge flow rate. The sign indicates direction of flow of positive charge and its magnitude indicates the net rate of charge flow per unit area. Mathematically this observation may be expressed as:

$$\oint_S \mathbf{J} \cdot \mathbf{n} da = -\frac{d}{dt}\int_V \rho_e dV \tag{A.11}$$

or, in differential format (again utilizing the divergence theorem) as:

$$\nabla \cdot \mathbf{J} + \frac{\partial \rho_e}{\partial t} = 0 \tag{A.12}$$

A.1.5 Ampére's Law

As a means to relate the magnetic effect of time varying electric fields and currents. Maxwell extended the original expression by adding the far right hand side term, known as displacement current, to account for influence of time varying electric fields displacing electrons and thus generating current.

$$\nabla \times \mathbf{B} = \mu_0 \mathbf{J} + \mu_0 \frac{\partial \epsilon_0 \mathbf{E}}{\partial t} \tag{A.13}$$

The later format is another of Maxwell's equations.

A.1.6 Faraday's Law of Induction

Faraday discovered that time varying magnetic fields induce an emf. He infered from this that time varying magnetic fields must produce time varying electric fields. Experimentally this was performed by thrusting a permanent bar magnet through a loop of wire and observing the induced current. The emf was equal to the change of flux

$$\varepsilon = \oint \mathbf{E} \cdot d\mathbf{l} = -\frac{d\Phi}{dt} \tag{A.14}$$

And **E** is related to a change B by the equation

$$\oint_C \mathbf{E} \cdot d\mathbf{l} = -\frac{d}{dt} \int_S \mathbf{B} \cdot \mathbf{n} da \tag{A.15}$$

Or by applying Stoke's theorem, in differential form as:

$$\nabla \times \mathbf{E} = -\frac{\partial \mathbf{B}}{\partial t} \tag{A.16}$$

The latter format is known as Faraday's Law and completes the set of Maxwell's equations.

A.2 Other Relations of Interest

The following describes other relations which may be referred to through the course of this work.

A.2.1 Biot-Savart Law

The Biot-Savart Law is a means to assist in calculating the field produced by an arbitrary current density. As can be imagined, the solution to many of the aforementioned equations may be challenging even for relatively simple geometry. The Biot-Savart

Law discritizes a current density into elements which may be individually solved to calculate the field, $d\mathbf{B}$, due to each current element, $d\mathbf{l}$.

A.2.2 Lenz's Law

Lenz's Law is a means by which to predict the direction of induced currents by means of energy conservation. Although, the same results may be achieved by scrutinizing Faraday's law, Lenz's law is perhaps a more intuitive procedure for predicting currents in a closed loop produced by a changing magnetic field. Essentially it states that the induced current will appear in a direction that opposes the change that produced it.

A.2.3 Lorentz Force

The Lorentz force, f, is defined as the force imposed on a test charge, q, that is moving with velocity, v while moving through electric field, E and magnetic field, B. This relation is quantified by:

$$\mathbf{f} = q\mathbf{E} + q\mathbf{v} \times \mathbf{B} \tag{A.17}$$

A single moving charge, $q\mathbf{v}$ may be expressed as a current. Thus the first term is a force on a static charge and the second term is the force on a current. As mentioned earlier, we are generally not concerned with electrostatics. Further, when considering the average contribution the force may be expressed as current density and the magnetic field as shown:

$$\mathbf{F} = \mathbf{J_f} \times \mathbf{B} \tag{A.18}$$

A.3 Magnetic Materials

When considering the design of electromagnetic actuators, how a material behaves in the presence of a magnetic field is of great importance. The orbiting electrons of a particular atom within any material cause small but significant electric currents, which in turn cause small magnetic fields. The spin of the electron about its own axis also contributes to this current. The way in which the atom's magnetic fields interact with each other determines the overall magnetic behavior. For example, the fields produced by the electron spins of most materials are random and cancel out. Other materials may have regions which have aligned spins and thus an overall net field exists. The orientations are susceptible to external fields where the net magnetic field may be decreased, or enhanced depending on the new orientation. Generally, there are three major classifications of magnetic materials, diamagnetic, paramagnetic and ferromagnetic. Diamagnetic materials are characterized by resisting an applied external field. The effect is slight, but still measurable. For example, a typical relative permeability of a diamagnetic material may be 0.9. Paramagnetic materials align so that there is a slight but measurable increase in the applied field. A typical relative permeability may be on the order of 1.1. Ferromagnetic material possesses the ability to greatly enhance an external field, with relative permeabilities ranging from 100 to 1,000,000. As the regions of common orbital spin align, the external field is intensified, after which, the material is said to be saturated and then behaves as though no material were present, or takes on permeability of free space. This saturation limit is of great concern when controlling solenoid actuators as the armature material will most likely be saturated at low air gaps, where accurate control is most desired. The effect is also significant as the transition from high permeability to free space permeability is nonlinear, making accurate analytic performance estimates extremely challenging. It should also be noted that once magnetized, the aligned regions do not instantaneously return to their initially demagnetized state, nor does flux density follow the same magnetization path. This phenomena is known as magnetic hysteresis. Although this may complicate even a low frequency analysis, it is often of greater concern with the design of higher frequency devices such as transformers. Hysteresis is often negligible in systems with air gaps, especially at low flux densities, as the energy required to magnetize the gap is several orders greater than any losses incurred through magnetic domain realignment. The field strength required to return a material to a demagnetized space is referred to as coercive force. Ferromagnetic permeability is also sensitive to temperature, with a sharp drop at what is referred to as the Curie temperature. This temperature typically corresponds with a phase change (change in crystalline structure).

Despite the complex properties of ferromagnetic materials, their high permeability allows flux to be constrained to a predefined path just as one would use wires to connect an electrical circuit. In fact, in many circumstances magnetic systems may be analyzed as a circuit problem rather than a field problem as discussed in Section 3.5.

A.4 Eddy Currents

Eddy currents are characterized as local circulating currents which exist in the core material. These are physically existing currents produced within the material due to a time varying core flux. They may be thought of as a short circuit consisting of coil wrapped around the external core material path in that the change in flux induces a current which in turn generates its own magnetic flux in the opposite sense (obeying Lenz's law) and ultimately apposes the change or rise of flux of the overall circuit. Thus, the observed flux rise or magnetization curve will be lower than the that of the static case. The energy difference between the static and rapid field buildup is defined through resistive losses and hence heating. In summary, the two effects of eddy currents are: an internal mmf is generated which tends to counteract the applied mmf, an irreversible heating loss of energy with the i^2 losses in the core. Thus greater changes in flux tend to generate more losses. A widening of the hysteresis loop is an indication of the eddy current magnitudes. They may be minimized by using materials with low conductivity and by laminating the core structure (through thin sheets or sintered powder metallurgy techniques). The laminations succeed by increasing the circulating path length and by breaking the eddy current paths into many smaller loops with lower magnitude and subsequently reduce the counter flux generated. In the actuator studied, there are no laminations, however the core back iron appears to be made from a power metallurgy process. One improvement may be to laminate the armature without compromising the mechanical durability. This may prove to be somewhat challenging as the armature is often subjected to high impacts in the event of a control failure. Note that the individual laminations need to be electrically insulated between each other thus possibly adding to the overall volume of the actuator. Eddy currents are not to be confused with the continuum mechanics Amperian currents generated by electron spin which are used to explain material magnetism.

Appendix B

Experimental Equipment

B.1 Introduction

The following provides the system setup and electronic schematics for the equipment used during the course of the experiments.

B.2 System and Electronics Schematics

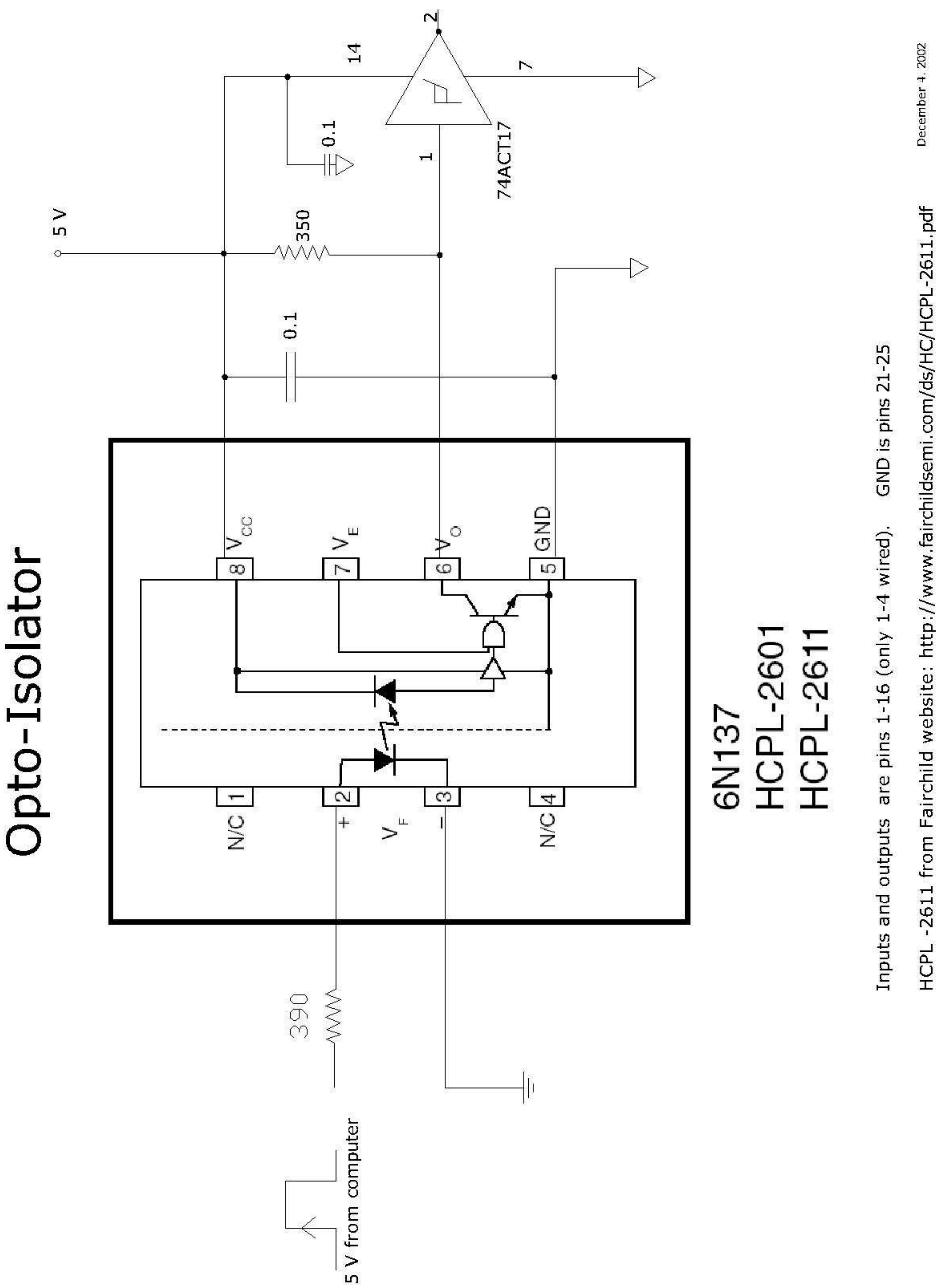

Figure B.1: Opto-Isolator Schematic (One Channel)

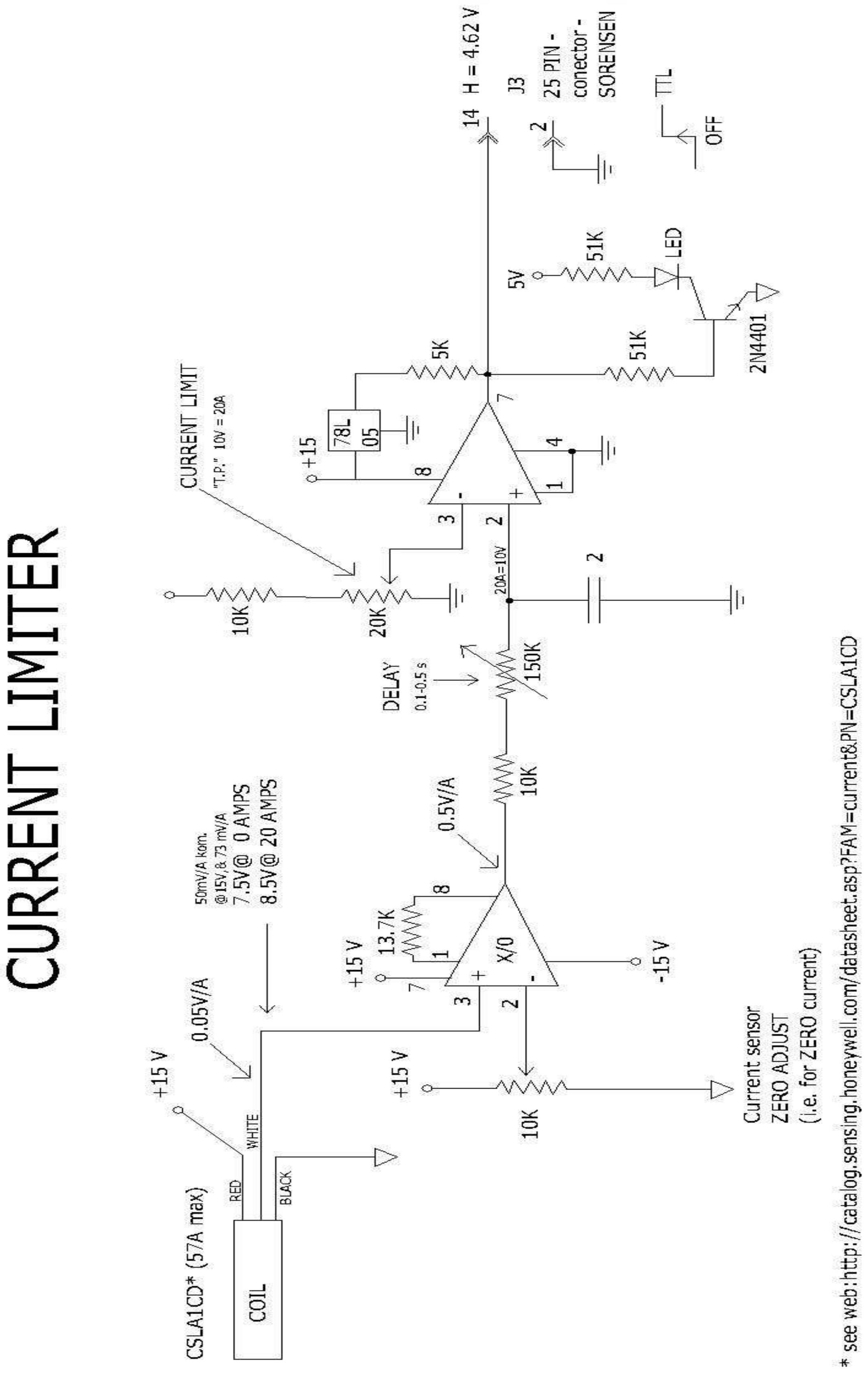

Figure B.2: Overload Protection Circuit Schematic

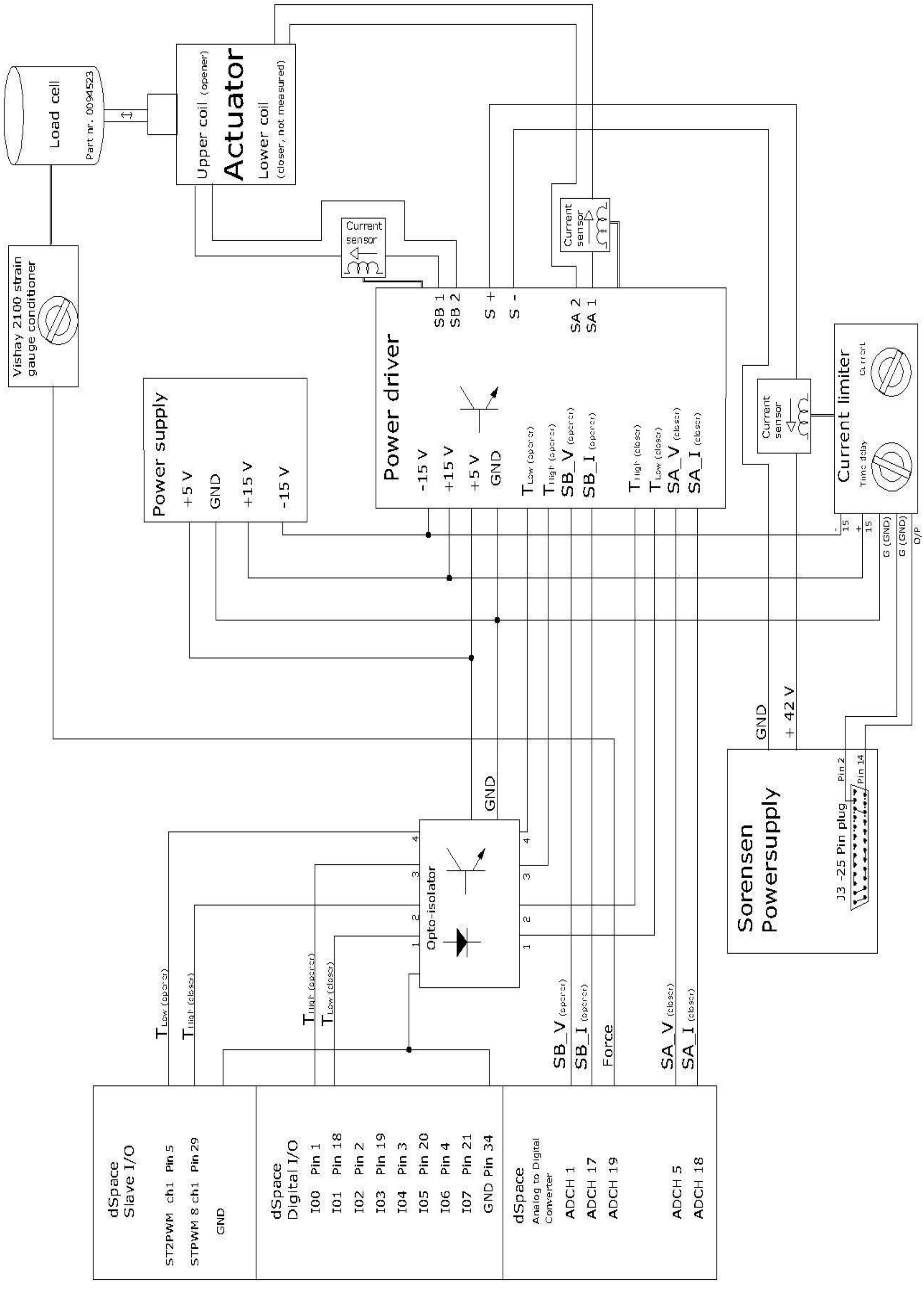

Figure B.3: MTS Detailed System Schematic

Appendix C

Actuator Properties and Specifications

C.1 Introduction

The following provides key actuator properties and data.

C.2 Actuator Specifications

Table C.1 lists the material properties for the prototype actuator donated by Daimler-Chrysler.

It is not presently known what grade of Vacflux the donated prototype consists of. Consequently these values should only be considered approximate. No material

Table C.1: Actuator Specifications

Parameter	Value
Effective Moving Mass	$155.8g$
Effective Spring Constant	$179\frac{kN}{m}$
Opener Coil Resistance (72 Turns)	0.37Ω
Closer Coil Resistance (79 Turns)	0.45Ω
Vacoflux50 Density	$8.12\frac{g}{cm^3}$
Vacoflux50 Resistivity	$0.43\frac{\Omega mm^2}{m}$
Vacoflux50 Thermal Conductivity	$30\frac{W}{Km}$
Vacoflux50 Curie Temp	950^oC
Vacoflux50 Elastic Modulus	$210\frac{kN}{mm^2}$

properties were able to be obtained for the QStE500 back iron material other than the DC induction curve shown in Figure C.1.

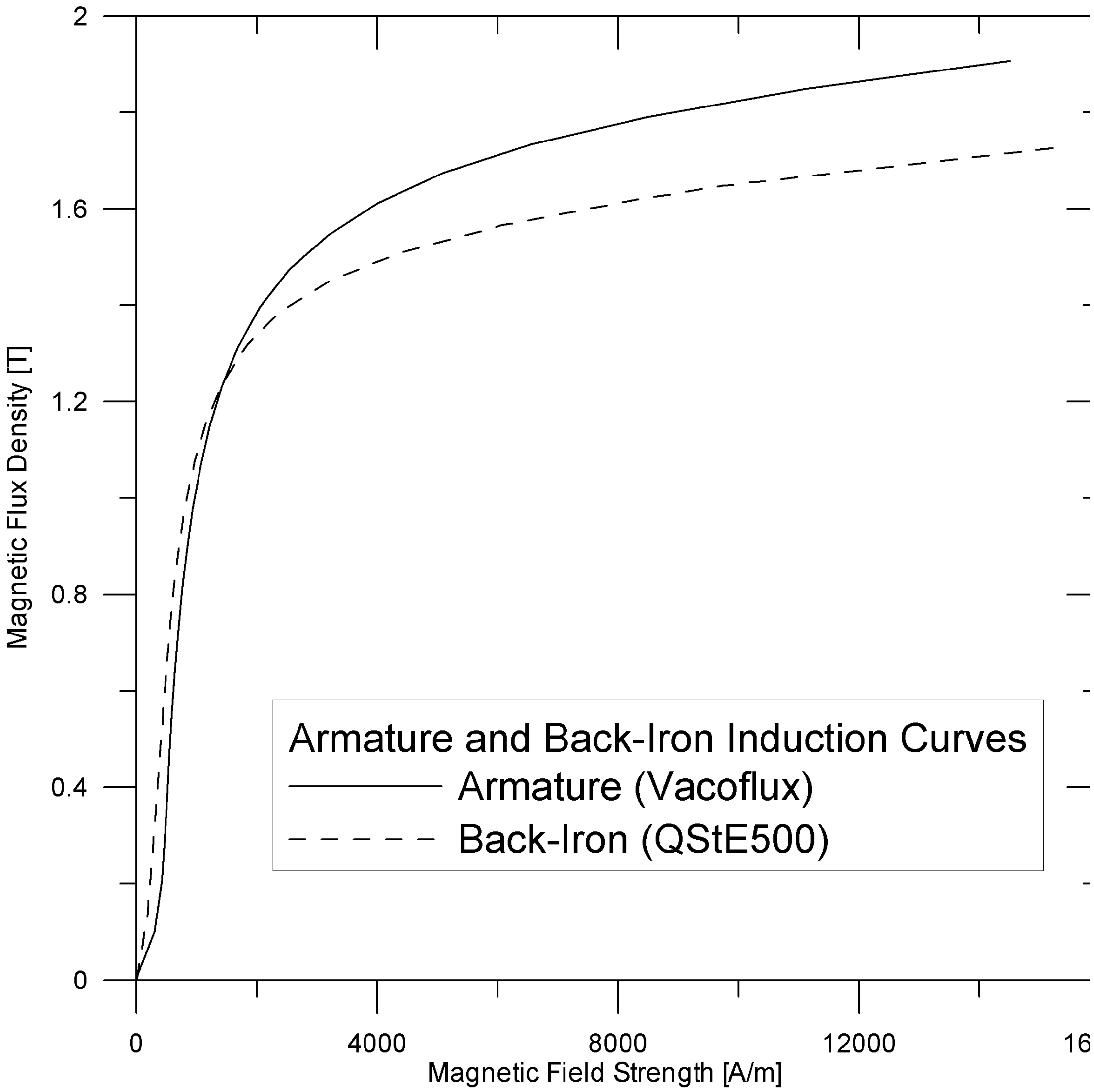

Figure C.1: Steady State Material Induction Curves

C.3 Spring Response

Actuator and valve return springs were measured over their entire operating stroke range as a means of enhancing LPM accuracy. The same MTS and load cell apparatus used in the static and transient experiments was used to measure the spring force response over a pre-specified 8mm displacement.

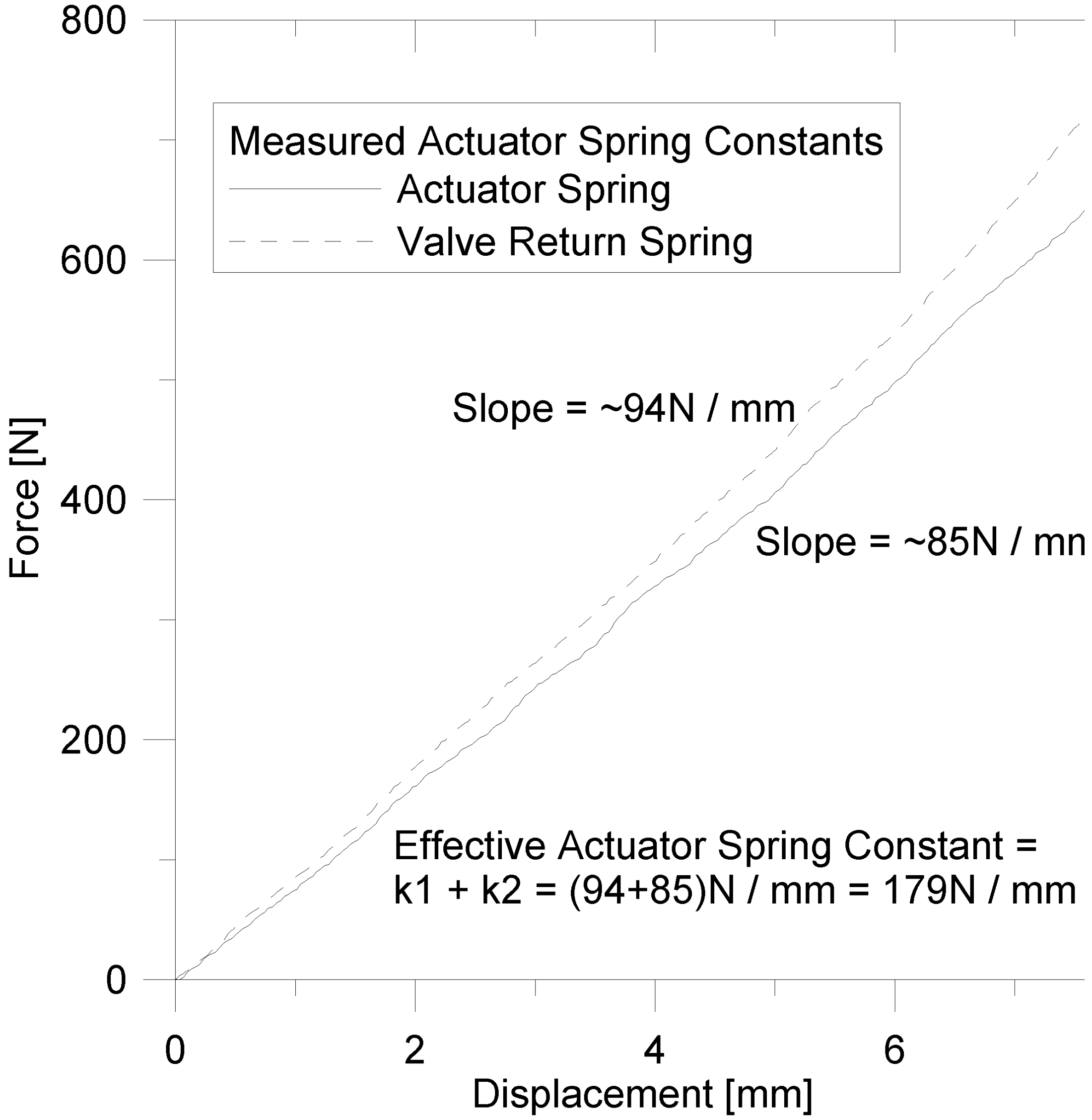

Figure C.2: Measured Spring Force Response

APPENDIX D

PROGRAM AND DATA FILE SUMMARY

D.1 Introduction

The following lists all command and data files that were used and generated over the course of this work.

D.2 ANSYS Static Command and Result Files

Table D.1: ANSYS Static Command and Result Files

File Description	File Name
ANSYS Master Command File (opener)	stopener.dat
ANSYS Master Command File (closer)	stcloser.dat
ANSYS Macro Command File (opener)	macopnr.lib
ANSYS Macro Command File (closer)	macclsr.lib
Output Force Result File (opener)	foropen.res
Output Flux Result File (opener)	flxopen.res
Output Force Result File (closer)	forclose.res
Output Flux Result File (closer)	flxclose.res
Matlab File Used to Process ANSYS Result Files	linpost.m
Matlab Output ANSYS Results File (opener)	opentab.m
Matlab Output ANSYS Results File (closer)	clostab.m

D.3 ANSYS Transient Command and Result Files

Table D.2: ANSYS Transient Command and Result Files

File Description	File Name
ANSYS Macro Command File (opener)	trnsopnr.lib
ANSYS Macro Command File (closer)	trnsclsr.lib
Output Transient Result File (opener)*	XXmmXXmsXXV_o.res
Output Transient Result File (closer)*	XXmmXXmsXXV_c.res

∗ - XXmmXXmsXXV represents the air gap in millimeters, pulse duration in milliseconds and pulse voltage level in volts.

D.4 Simulink Lumped Parameter Model and Result Files

Table D.3: Simulink Lumped Parameter Model and Result Files

File Description	File Name
Simulink Initialization File	LPMinitial.m
Simulink Model File	LPMactu.mdl
Modified Transient Model File (fixed position)	modtrans.mdl
Output Simulation Time File (fixed position)*	t_XXmmXXmsXXV.csv
Output Current File (fixed position)*	c_XXmmXXmsXXV.csv
Output Force File (fixed position)*	f_XXmmXXmsXXV.csv

∗ - XXmmXXmsXXV represents the air gap in millimeters, pulse duration in milliseconds and pulse voltage level in volts.

D.5 Linear Theory Model and Result Files

Table D.4: Linear Theory Model and Result Files

File Description	File Name
Static Force and Inductance Calculation	lnforind.m
Simulink Linear Model Initialization File	lninit.m
Simulink Model File	lnactu.mdl
Output Simulation Time File*	lint_XXmmXXmsXXV.csv
Output Current File*	linc_XXmmXXmsXXV.csv
Output Force File*	linf_XXmmXXmsXXV.csv

∗ - XXmmXXmsXXV represents the air gap in millimeters, pulse duration in milliseconds and pulse voltage level in volts.

D.6 Static Experimental Program and Data Files

Table D.5: Static Experimental Raw Data Files

File Description	File Name
Control Desk Interface File	fr_10.cdx
Control Desk Scope File	fr_10scope.lay
dSpace Make File (to be compiled)	fr.mk
Control Desk Setup Instructions (how to get PWM control working)	PWM_50_50.doc
Variable Files	fr.trc
Compiled dSpace Executable File	fr.ppc
Current Control Program Files	...\src\∗.c
Measured Experimental Time, Force and Current*	exp_XXmmXXA.csv

∗ - XXmmXXmsXXV represents the air gap in millimeters and excitation in amps.

D.7 Transient Experimental Program and Data Files

Table D.6: Transient Experimental Raw Data Files

File Description	File Name
Measured Experimental Time, Voltage, Current and Force*	exp_XXmmXXmsXXV.csv

* - XXmmXXmsXXV represents the air gap in millimeters, pulse duration in milliseconds and pulse voltage level in volts.

D.8 Miscellaneous Analysis and Data Files

Table D.7: Miscellaneous Analysis and Data Files

File Description	File Name
Average Normalized ANSYS and Linear Model Error	errcalc.m
Leverage Ratio Calculation	levratio.m
Measured Spring Force Data	sprngfor.xls
Back Iron and Armature B-H Curve Data	BHcurves.xls